Elucidating Igneous and Ore-Forming Processes with Iron Isotopes by using Experimental and Field-Based Methods

by

Laura Danielle Bilenker

A dissertation submitted in partial fulfillment
of the requirements for the degree of
Doctor of Philosophy
(Earth and Environmental Sciences)
in the University of Michigan
2015

Doctoral Committee:

Associate Professor Adam Charles Simon, Chair
Professor Joel D. Blum
Professor Rebecca Ann Lange
Associate Research Scientist Gordon Moore
Professor Sally Oey
Assistant Professor Jill A. VanTongeren, Rutgers University

DEDICATION

I dedicate this work to two great role models whose love for science and the outdoors inspired my own at an early age: my father, Jim, and my late Zayde. I owe each of them for my success in graduate school and research. In fact, Zayde's muffle furnace traveled from New Jersey to Michigan to contribute to Chapter II.

ACKNOWLEDGEMENTS

I would like to express my gratitude to my committee whose time and feedback were extremely valuable: Drs. Joel Blum, Becky Lange, Gordon Moore, Sally Oey, and Jill VanTongeren. Skype sessions and long emails with Jill preserved my sanity for that last chapter. Thank you for always being so positive and for making the Bushveld project possible. I would especially like to thank my advisor, Dr. Adam Simon, for the valuable advice, guidance, patience, time, and for bringing me to the University Michigan. I have learned a great deal from Adam about research, teaching, writing, and life that will certainly help me throughout my career.

Although he is not on my committee, Dr. Craig Lundstrom was a key player in this dissertation. He was instrumental in the project presented in Chapter II and has been a valuable collaborator for all of my Fe isotope work thus far. I have enjoyed working with him and always appreciate his insight. Without Norbert Gajos and Jim Palandri, much of the initial Fe and none of the O isotope data presented here would not have been possible. Likewise, Chapter III would not have been possible without Martin Reich and Fernando Barra at the University of Chile. Their guidance and connections in the field, generosity with supplemental samples, and co-authorship made Chapter III possible. Anne Hudon and Bill Wilcox were also lifesavers in other significant ways. Financially, the projects presented here were made possible by the Society of Economic Geologists Student Research Grant, the UM Dept. Earth & Environmental Sciences Turner Award, the National Science Foundation, and the UM Rackham Graduate School.

Transferring to Michigan was an unexpected, valuable opportunity and I am so fortunate to have ended up as part of an awesome lab *family*: thank you Tom (my academic twin), Jaayke (my temporary roomie, co-author, guaranteed ice cream buddy), Tristan (you've been more help than you know), and Brian (please do not blow up *all* of the Renés). The same goes for my academic older siblings and role models, despite frequently communicating overseas and across continents: Drs. Adrian Fiege, Harmony Colella, and Thomas Giachetti. I would also like to express my gratitude for the abundant support, entertainment, and love provided by the rest of my grad student family. I am eternally grateful for you all: Samantha, Trever, Joe, Pam, Anaïs (my technological savior!), Xiaofei, Kyle, Sarah, Man Sam, Ross, Kate, the rest of the 2012 cohort, and particularly Liz Tanis, who was first my lab mate and housemate in Vegas and became a best friend in Michigan.

I especially appreciate the long-distance support of my family and friends-like-family (Kristin, Jo, Alex, Catt, Jeff, Riggins, Jeri, Vicki, Susan, Grandma Ruth), for whom it's been worth many, many flights and long drives to participate in various life events. But lastly and above all, I owe so much to my parents and sister: Lanie, Jim, and Julie. I simply would not be where I am or who I am without their unconditional and constant love, support, generosity, and understanding. Thank you for every note, flower, gift basket, phone call, visit, brisket, and matzoh ball while I've lived no closer than 600 miles from home since college.

TABLE OF CONTENTS

LIST OF TABLES

CHAPTER II

CHAPTER III

APPENDIX

LIST OF FIGURES

CHAPTER II

CHAPTER III

CHAPTER IV

APPENDIX

ABSTRACT

Iron (Fe) is a vital resource and the fourth most common element in the Earth's crust, but variations in the Fe isotope composition of igneous rocks were only recently identified. This dissertation uses experimental and field-based methods to demonstrate the utility of Fe isotopes in tracking igneous and ore-forming processes. Chapter II presents the first experimental data that measure directly Fe isotope fractionation among phases in a fluid-bearing magmatic assemblage. The results, some of which contradict theoretical predictions, indicate that Fe isotopes fractionate during crystallization of magnetite from a melt and that Fe isotope fractionation between melt—fluid is influenced by the Cl content of the fluid. This is important considering the frequent extrapolation of data obtained from Fe-Cl complexes that are unrealistic for magmatic systems. Chapter III applies Fe isotopes to natural ore samples since Fe is globally mined from the rocks of iron oxide—apatite (IOA) deposits, which are a globally important source of Fe and other elements such as the rare earths but lack a genetic model. I focus on the world-class Los Colorados IOA, Chile as a case study and combine the Fe and O isotope composition of magnetite to investigate their formation. The data are consistent with a high-temperature (i.e., magmatic/magmatic-hydrothermal) origin for IOA deposits, and contributed to the development of a published novel IOA model. Iron is also abundant in layered mafic intrusions, and Chapter IV focuses on the uppermost portion of the world's largest exposed mafic magma chamber, the Bushveld Complex, South Africa. These Fe isotope data demonstrate that fractional crystallization is reflected in the Fe isotope signature of the uppermost Bushveld. Stratigraphically, over the top ~2.5 km of this 9 km-thick intrusion, there is little variation in

both whole rock and magnetite Fe isotope compositions, revealing that, despite theoretical predictions for the crystallization of magnetite to shift the isotopic composition of the whole rock, the presence of other Fe-bearing phases can buffer that effect. By incorporating published fractionation factors to model the measured data, this study provides the first benchmark for Fe isotope evolution during the crystallization of a large magma chamber.

CHAPTER I

INTRODUCTION

Iron (Fe) is ubiquitous in geological materials and is the fourth most common element in the Earth's crust. It is frequently present in igneous rocks as an oxide, (e.g., magnetite, Fe_3O_4; ilmenite, $FeTiO_3$; hematite, Fe_2O_3) and is abundant in ore deposits where elements have been concentrated by geological processes to economically extractable levels. Iron is one of the most abundant redox-sensitive elements in such systems, and is a useful tracer of geochemical processes because it can exist as Fe^{2+} (ferrous) or Fe^{3+} (ferric). Further, Fe has four stable isotopes: masses 54, 56, 57, and 58. Mass 56 is the most abundant (91.76%), followed by 54 (5.84%), 57 (2.12%), and 58 (0.28%) (Beard and Johnson, 2004). Geological processes influence the behavior of each mass differently, producing mass-dependent fractionation of the isotopes between phases within a given system (e.g., minerals, fluids, melts within a magmatic system).

Within a societal context, Fe is an indispensible resource as it is the main constituent in steel, which is used in construction materials, vehicles, magnets, and many other industrial applications. Iron ore deposits are usually mined for their Fe oxides (e.g., magnetite, hematite) and many are formed by igneous processes. For example, iron oxide—apatite (IOA) and iron oxide—copper—gold (IOCG) deposits can individually contain millions to billions of tons of Fe with whole rock compositions of up to >90 modal% Fe oxide. They are also often mined for economic grades of copper, gold, rare earth elements, titanium, phosphorous, and occasionally uranium (c.f. Barton, 2014). These other metals are vital to society as well, making IOA and

IOCG deposits extremely valuable. However, despite their worldwide importance, there is much debate surrounding a genetic model for IOA and IOCGs, akin to the disagreement regarding the formation of many other igneous ore deposits (e.g., Bushveld Igneous Complex, South Africa). This dissertation demonstrates our ability to use Fe isotopes to disentangle some of the igneous processes important in producing ore deposits.

The Fe Isotope Composition of Igneous Rocks

When Poitrasson and Freydier (2005) published the Fe isotope values of 11 granites ranging in SiO_2 from 64.9 to 77.7 wt.% and MgO from 0.06 to 1.84 wt.%, they were the first to draw attention to a positive correlation between increasing Fe stable isotope ratios ($\delta^{5\#}Fe = {}^{5\#}Fe/{}^{54}Fe$ of the sample relative to standard IRMM-14) and SiO_2 content of igneous rocks. They suggested that the most likely explanation for the trend was the exsolution of an aqueous fluid enriched in Fe^{2+} (and therefore ^{54}Fe), driving the rock to a heavier isotopic composition. Heimann et al. (2008) invoked the same model based on data from dozens more plutonic and volcanic rocks that displayed the same trend of increasing $\delta^{56}Fe$ vs. SiO_2 trend. Heimann et al. (2008) also measured the $\delta^{56}Fe$ composition of mineral separates from a global variety of igneous rocks from around the globe and found that some minerals (e.g., magnetite) preferentially incorporate heavy Fe isotopes over light Fe isotopes. This is expected, since Fe isotope systematics are probably controlled in part by changes in Fe valence state. Ferric Fe is a smaller ion, and therefore forms stronger bonds than the larger ion, ferrous Fe. Additionally, theory, supported by spectroscopy, predicts that phases containing more Fe^{3+} will preferentially incorporate heavy Fe isotopes relative to Fe^{2+}-bearing phases (Polykov and Mineev 2000; Polykov et al. 2007). For example, magnetite, which contains a molar ratio of 2 Fe^{3+} to 1 Fe^{2+},

preferentially incorporates isotopically heavy Fe into its structure. Conversely, fayalite, which contains only ferrous Fe, is relatively isotopically light.

Experimental studies conducted at high temperatures corroborate the fractionation trends measured in natural samples. Schuessler et al. (2007) and Shahar et al. (2008) quantified experimentally Fe isotope fractionation between pyrrhotite and peralkaline rhyolite, and magnetite and fayalite, respectively. They are the only experimental studies published to date conducted at conditions relevant to igneous systems, and they were the first experimental studies to demonstrate that Fe isotopes fractionate in igneous systems due to crystallization of individual mineral phases as well as magmatic redox processes.

Due to the paucity of experimental data on Fe isotope fractionation at magmatic-hydrothermal conditions, many hypotheses (e.g., fluid exsolution) are based solely on theoretical calculations (e.g. Polyakov and Mineev, 2000; Schauble et al., 2001; Polyakov et al., 2007), utilizing data that are unrealistic for magmatic-hydrothermal systems. This is problematic because, as experimental data for stable Fe isotope fractionation at magmatic conditions are produced and more natural samples analyzed, results are inconsistent with these predictions (e.g., Shahar et al., 2008; Heimann et al., 2008). To track magmatic processes within a volcanic system and to further contribute to the growing database of Fe isotope values of igneous rocks, Schuessler et al. (2009) analyzed Icelandic samples, primarily from eruptions of Hekla volcano. Like Heimann et al. (2008) and Poitrasson and Freydier (2005), Schuessler et al. (2009) also reported higher $\delta^{56}Fe$ values in more evolved samples ($\delta^{56}Fe_{dacite} = 0.051 \pm 0.021‰$ to $\delta^{56}Fe_{rhyolite} = 0.168 \pm 0.021‰$). Evaluation of Li concentrations and measured $\delta^{7}Li$ values demonstrated minimal, if any, fluid exsolution, so Schuessler et al. (2009) concluded that the Fe

isotope fractionation observed at Hekla was caused by crystal fractionation as the magma evolved from dacite to rhyolite.

These data are consistent with those of Sossi et al. (2012), which support a hypothesis that couples redox processes and fractional crystallization as the mechanisms by which Fe isotopes fractionate in closed igneous systems. They sampled stratigraphically through the 420 m thick Red Hill sill in Tasmania, which is thought to have formed by a single intrusive event. The system was closed to O_2 and experienced fractional crystallization, the record of which is observed *in situ*. The whole rock data for this locality are different from the $\delta^{56}Fe$ vs. SiO_2 pattern identified by earlier studies in that $\delta^{56}Fe$ at first increases during the crystallization of pyroxene, peaking at magnetite saturation, and then decreases during magnetite crystallization. Sossi et al. (2012) reported an equilibrium fractionation factor (Δ) between magnetite and melt of $\Delta^{57}Fe_{magnetite\text{-}melt} = 0.20‰ \times 10^6/T^2$, where Δ is calculated as difference in δ value between two phases for any isotope ratio:

$$\Delta^{\#\#}Fe_{A\text{-}B}\ (‰) = \delta^{\#\#}Fe_A - \delta^{\#\#}Fe_B \qquad (1.2)$$

Fractionation of Fe between magnetite and pyroxene in the Red Hill sill is approximately 0.30‰ at 900-1000°C. They note that pyroxene, which contains Fe^{2+}, is relatively depleted in heavy Fe isotopes, and suggest that fractionation of pyroxene would result in an increase in oxygen fugacity (fO_2) and, in conjunction, the $Fe^{3+}/\Sigma Fe$ and $\delta^{57}Fe$ of an unbuffered melt to increase. This would occur until magnetite saturation when the crystallization of magnetite would result in a decrease in the $\delta^{57}Fe$ of the melt, as is observed.

It is also possible that fractionation of stable Fe isotopes is driven by a sustained thermal gradient. Huang et al. (2010) demonstrated experimentally that Fe isotopes can fractionate this way, with isotopically heavier Fe compositions measured in more differentiated (i.e., colder)

samples. Zambardi et al. (2014) invoked this mechanism to explain stratigraphic variations in the Fe isotope composition of samples from the Finland granophyre of the Duluth Complex (Montana, USA). They paired stable Fe isotope values with Si isotope values to reveal that neither fluid exsolution nor crystal fractionation could explain the observed data for both isotopic systems, but could be explained by the hypothesis that the isotopes fractionated in response to a thermal gradient.

In summary, within a magma or magmatic-hydrothermal system, it has been hypothesized that Fe isotopes fractionate due to: 1) exsolution and loss of an aqueous fluid (Poitrasson and Freydier, 2005; Heimann et al., 2008; Telus et al., 2012); 2) fractional crystallization, which may also involve redox processes since higher valence state and heavier isotopic ratios are often correlated (Schuessler et al., 2007; Teng et al., 2008; Schuessler et al., 2009; Sossi et al., 2012; Dauphas et al., 2014; Foden et al., 2015); and 3) thermal diffusion effects reflecting differentiation within a temperature gradient (Lundstrom, 2009; Huang et al., 2010; Zambardi et al., 2014).

Chapter II of this dissertation reports the first experimental study to measure directly the role of a fluid phase in controlling Fe isotope fractionation at magmatic conditions. This is particularly important due to the frequent invocation of fluid exsolution to cause the observed pattern of increasing Fe isotope ratios with increasing SiO_2 content. I performed two- (mineral-fluid) and three- (mineral-fluid-melt) phase high-temperature experiments in order to test the hypothesis that the $\delta^{56}Fe$ trend of igneous rocks was caused by fluid exsolution. The results are inconsistent with theoretical predictions, suggesting that Fe isotope fractionation between fluid and melt is more complicated than was considered previously. This chapter is under review at *Geochimica et Cosmochimica Acta.*

Using Fe Isotopes to Study Natural Ore Deposits

Chapter III explores the utility of stable Fe isotopes when paired with the well-developed and understood stable isotope system of oxygen (O) by measuring Fe—O stable isotope pairs in magnetite from known igneous sources as well as IOA and IOCG deposits. The actively mined Los Colorados IOA deposit in Northern Chile serves as the case study. This kind of isotopic approach was attempted only once before on IOA samples, in the thesis of Weis (2013). Chilean IOA and IOCG samples were collected from drill cores and the mine pit at Los Colorados and well as an inactive mine sites at Mariela. We also analyzed drill core from El Laco (Chile) as well as Kiruna (Sweden) and Mineville (USA). By pairing Fe isotope data with O isotope values for magnetite, we are developing a new technique with which we can decipher whether Fe oxide was formed under high- or low-temperature conditions (i.e., magmatic/magmatic-hydrothermal vs. meteoric).

The detailed isotopic study, to be submitted to *Geochimica et Cosmochimica Acta*, revealed a high-temperature environment for the formation of Los Colorados and other Chilean Fe oxide deposits, as well as the Swedish IOA type locale, Kiruna. The isotopic data agree with minimum formation temperatures calculated by measuring the O isotope and Fe/Mg compositions of co-existing actinolite (610-820°C). The data demonstrate that magmatic magnetite has Fe—O isotopic compositions within the previously established range of $\delta^{56}Fe$ = 0.06-0.49‰ (Heimann et al., 2008; Weis, 2013) and $\delta^{18}O$ = 1.0-4.4‰ (Taylor 1967; 1968). Additionally, magnetite that formed by lower temperature processes such as the remobilization or replacement of Fe (e.g., the Mineville deposit) has an isotopically lighter Fe and O signature. So far, this technique cannot decipher between different high-temperature processes, but further calibration of the method will make Fe—O isotope pairing a useful geochemical tool to

fingerprint the source of Fe oxide in rocks including ore deposits. These natural isotopic data were also used in conjunction with geochemical analyses of magnetite to propose a novel formation model for IOAs, published in *Geology* in 2015 (Knipping et al., 2015).

Chapter IV also examines the Fe isotope systematics of a natural system, focusing on the uppermost ~2.5 km of the Bushveld Igneous Complex, South Africa. The Bushveld is the world's largest exposed mafic magma chamber and the uppermost portion is thought to have formed from a single injection of magma that evolved under relatively closed conditions. In this chapter, submitted to *Geology*, we report the first stable Fe isotope data measured throughout the stratigraphy of the Upper and Upper Main Zones (UUMZ), using samples previously characterized by VanTongeren et al. (2010) and VanTongeren and Mathez (2012). By incorporating published mineral-melt fractionation factors to model the measured Fe isotope data obtained from whole rock samples and magnetite separates, this study provides the first benchmark for Fe isotope evolution during the crystallization of a large magma chamber.

Our current state of knowledge regarding Fe isotope fractionation at magmatic and magmatic-hydrothermal conditions is assessed in ***Chapter V*** by highlighting the contributions of this dissertation to the recently-developed field of high-temperature Fe isotope geochemistry, as well as the application of these new geochemical tools to deposits of economic importance. Since igneous Fe isotope studies were made possible recently by the improved precision of the multi-collector inductively coupled plasma mass spectrometer, this field is only about one decade old. Thus, the experimental and natural studies completed in this dissertation can help to advance igneous Fe isotope geochemistry as it grows.

References

Barton M.D. (2014) Iron Oxide(-Cu-Au-REE-P-Ag-U-Co) Systems. In: *Treatise on Geochemistry*, 2nd edition, vol. 11, p. 515-541.

Beard B.L. and Johnson C.M. (2004) Fe isotope variations in the modern and ancient earth and other planetary bodies. *RiMG* **55**, 319-357.

Dauphas N., Roskosz M., Alp E.E., Neuville D.R., Hu M.Y, Sio C.K., Tissot F.L.H, Zhao J., Tissandier L., Médard and Cordier C. (2014) Magma redox and structural controls on iron isotope variations in Earth's mantle and crust. *Earth Planet. Sc. Lett.* **308**, 127-140.

Foden J., Sossi P.A. and Wawryk C.M. (2015) Fe isotopes and the contrasting petrogenesis of A-, I- and S-type granite. *Lithos,* doi:10.1016/j.lithos.2014.10.015.

Heimann A., Beard, B.L. and Johnson C.M. (2008) The role of volatile exsolution and sub-solidus fluid/rock interactions in producing high $^{56}Fe/^{54}Fe$ ratios in siliceous igneous rocks. *Geochim. Cosmochim. Acta* **72**, 4379-4396.

Huang F., Chakraborty P., Lundstrom C.C., Holmden C., Glessner J.J.G., Kieffer S.W. and Lesher C.E. (2010) Isotope fractionation in silicate melts by thermal diffusion. *Nature* **464**, 396-400.

Knipping J.L., Bilenker L.D., Simon A.C., Reich M., Barra F., Deditius A.P., Lundstrom C., Bindeman I. and Munizaga R. (2015) Giant Kiruna-type deposits form by efficient floation of magmatic magnetite suspensions. *Geology*, published online 19 May 2014, doi:10.1130/G36650.1.

Lundstrom C.C. (2009) Hypothesis for the origin of convergent margin granitoids and Earth's continental crust by thermal migration zone refining. *Geochim. Cosmochim. Acta* **73**, 5709-5729.

Poitrasson F. and Freydier R. (2005) Heavy iron isotope composition of granites determined by high resolution MC-ICP-MS. *Chem. Geol.* **222**, 132-147.

Polyakov V.B. and Mineev S.D. (2000) The use of Mössbauer spectroscopy in stable isotope geochemistry. *Geochim. Cosmochim. Acta* **64**, 849-865.

Polyakov V.B., Clayton R.N., Horita J. and Mineev S.D. (2007) Equilibrium iron isotope fractionation factors of minerals: Reevaluation from the data of nuclear inelastic resonant X-ray scattering and Mössbauer spectroscopy. *Geochim. Cosmochim. Acta* **71**, 3833-3846.

Schuessler J.A., Schoenberg R., Behrens H. and von Blanckenburg F. (2007) The experimental calibration of the iron isotope fractionation factor between pyrrhotite and peralkaline rhyoltic melt. *Geochim. Cosmochim. Acta* **71**, 417-433.

Schuessler J.A., Schoenberg R. and Sigmarsson O. (2009) Iron and lithium isotope systematics of the Hekla volcano, Iceland—Evidence for Fe isotope fractionation during magma differentiation. *Chem. Geol.* **258**, 78-91.

Shahar A., Young E.D. and Manning C.E. (2008) Equilibrium high-temperature Fe isotope fractionation between fayalite and magnetite: An experimental calibration. *Earth Planet. Sc. Lett.* **268**, 330-338.

Schauble E.A., Rossman G.R. and Taylor Jr. H.P. (2001) Theoretical estimates of equilibrium Fe-isotope fractionations from vibrational spectroscopy. *Geochim. Cosmochim. Acta* **65**, 2487-2497.

Sossi P.A., Foden J.D. and Halverson G.P. (2012) Redox-controlled iron isotope fractionation during magmatic differentiation: an example from the Red Hill intrusion, S. Tasmania. *Contrib. Mineral. Petrol.* **164**, 757-779.

Telus M., Dauphas N., Moynier F., Tissot F. L.H., Teng F-Z., Nabelek P.I., Craddock P.R. and Groat L.A. (2012) Iron, zinc, magnesium and uranium isotopic fractionation during continental crust differentiation: The tale from migmatites, granitoids, and pegmatites. *Geochim. Cosmochim. Acta* **97**, 247-265.

Teng F., Dauphas N. and Helz R.T. (2008) Iron isotope fractionation during magmatic differentiation in Kilauea Iki Lava Lake. *Science* **320**, 1620-1622.

VanTongeren J.A., Mathez E.A. and Kelemen P.B. (2010) A Felsic End to Bushveld Differentiation. *J. Petrol.* **51**, 1891-1942.

VanTongeren J.A. and Mathez E.A. (2012) Large-scale liquid immiscibility at the top of the Bushveld Complex. *Geology* **40**, 491-494.

Zambardi T., Lundstrom C.C., Li X. and McCurry M. (2014) Fe and Si isotope variations at Cedar Butte volcano; insight into magmatic differentiation. *Earth Planet. Sc. Lett.* **405**, 169-179.

CHAPTER II

EXPERIMENTAL DETERMINATION OF IRON ISOTOPE FRACTIONATION AMONG MAGNETITE, FLUID, AND SILICATE MELT

ABSTRACT

Several hypotheses have been invoked to explain the observation that $^{56}Fe/^{54}Fe$ and $^{57}Fe/^{54}Fe$ ratios generally increase with increasing SiO_2 contents of igneous rocks: 1) exsolution and loss of an aqueous fluid; 2) fractional crystallization, including associated changes in oxygen fugacity (fO_2); and 3) thermal diffusion during magmatic differentiation. We experimentally quantified equilibrium Fe isotope fractionation among silicate melt, aqueous Cl-bearing fluid, and magnetite to test the first two hypotheses. Experiments were performed in Au capsules at 800°C and fO_2 buffered at nickel-nickel oxide (NNO) for two assemblages: magnetite-aqueous fluid (150 MPa, 10 wt.% NaCl eq.) and magnetite-aqueous fluid-rhyolite melt (100 MPa, 1.8 wt.% NaCl eq.). In all experiments, the aqueous fluid existed above the critical point as a single phase, where Fe is present only as the neutral ferrous complex $FeCl_2$. We assessed the loss of Fe to the capsule by mass balancing Fe isotopes in the magnetite-fluid-melt-capsule assemblage, which indicates that Fe loss is minimal and does not affect the reported fractionation factors. The experimentally determined fractionation factors ($\Delta_{a\text{-}b}$) (± 2σ) at 800°C, 100 MPa, ~NNO are: $\Delta^{56}Fe_{magnetite\text{-}fluid} = 0.75 \pm 0.08‰$; $\Delta^{56}Fe_{magnetite\text{-}melt} = 0.95 \pm 0.05‰$; and $\Delta^{56}Fe_{melt\text{-}fluid} = -0.20 \pm 0.07‰$. The values determined for $\Delta^{56}Fe_{magnetite\text{-}fluid}$ and $\Delta^{56}Fe_{magnetite\text{-}melt}$ are consistent with theoretical predictions and existing experimental data that indicate that the higher $Fe^{3+}/\sum Fe$ ratio

of magnetite leads to its preferentially incorporating isotopically heavier Fe relative to coexisting silicate melt and fluid.

Using the melt-magnetite fractionation factor, modeled fractional crystallization involving removal of magnetite will lead to lighter Fe isotopic ratios with increasing SiO_2, opposite to the observed trends in igneous differentiation suites. The value for $\Delta^{56}Fe_{melt\text{-}fluid}$ indicates that rhyolitic melt is isotopically lighter than co-existing Cl-bearing aqueous fluid, despite $Fe^{3+}/\sum Fe_{melt} > Fe^{3+}/\sum Fe_{fluid}$. This may reflect the effects of fluid composition on Fe coordination in the fluid, which is consistent with results recently reported for force constants measured for a range of silicate melt compositions, and with published B isotope fractionation data from a melt-fluid assemblage. Thus, exsolution of a Cl-bearing aqueous fluid will make the silicate melt phase isotopically lighter and cannot be solely responsible for the observed changes in $^{56}Fe/^{54}Fe$ with differentiation. However, rhyolitic magma (melt + coexisting magnetite) will become increasingly isotopically heavy during progressive fluid loss providing a possible explanation for isotope signatures observed in natural samples.

2.1. INTRODUCTION

Historically, it has been assumed that igneous rocks were isotopically homogeneous with respect to Fe and other stable metal isotopes, since the magnitude of equilibrium isotopic fractionations are predicted to scale as $1/T^2$ (Urey, 1947; Schauble, 2004). However, several recent studies of igneous rocks, across a wide range of compositions from basalt to rhyolite, report that the whole rock Fe isotope ratios become heavier with increasing SiO_2 content (e.g., Poitrasson and Freydier, 2005; Heimann et al., 2008) (Figure 2.1). The data plotted in Figure 2.1 include whole rock samples from a wide range of igneous environments, including plutonic and volcanic, open and closed systems, and diverse alteration histories. Plausible hypotheses invoked

to explain this excursion include: 1) exsolution and loss of an aqueous fluid that preferentially scavenges isotopically light Fe from the magma (Poitrasson and Freydier, 2005; Heimann et al., 2008; Telus et al., 2012); 2) fractional crystallization, which may also involve redox processes since higher valence state and heavier isotopic ratios are often correlated (Schuessler et al., 2007; Teng et al., 2008; Schuessler et al., 2009; Sossi et al., 2012; Dauphas et al., 2014; Foden et al., 2015); and 3) thermal diffusion effects reflecting differentiation within a temperature gradient (Lundstrom, 2009; Huang et al., 2010; Zambardi et al., 2014). Variations in magma source controls such as mantle isotopic composition have been used to explain mantle peridotite variations (e.g., Williams et al., 2005; Weyer, 2008) but are generally not considered responsible for the trend in $\delta^{56}Fe$ with SiO_2.

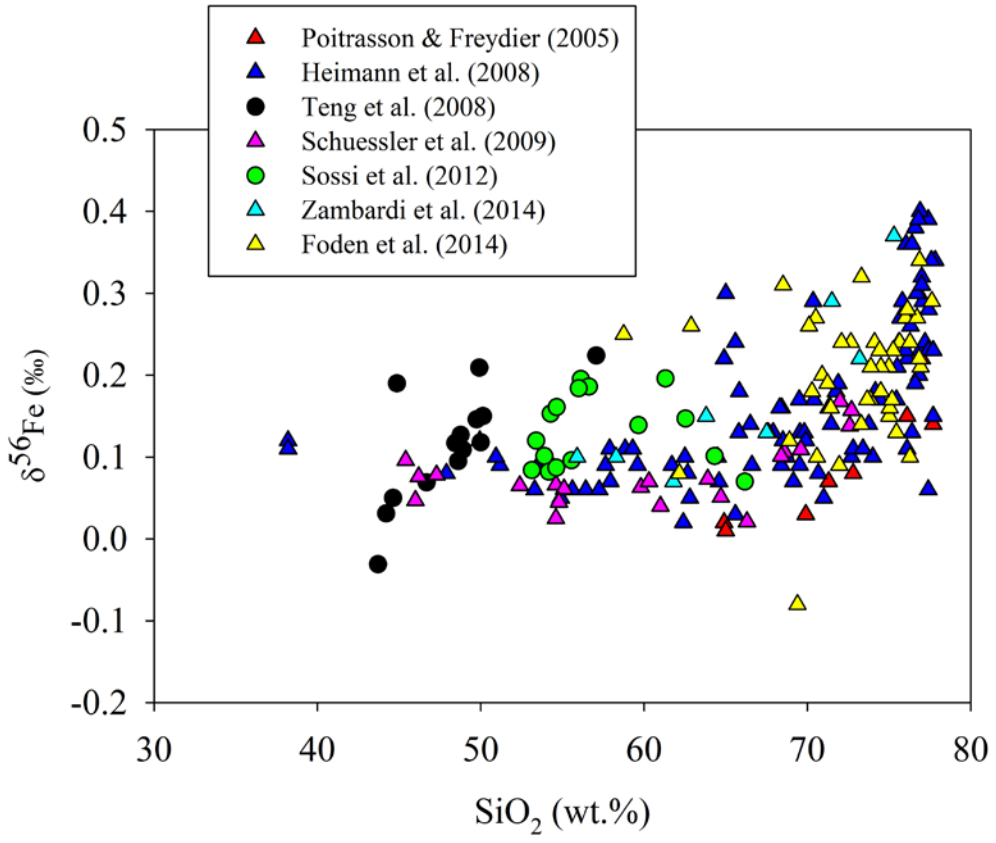

Figure 2.1: Whole rock $\delta^{56}Fe$ values versus SiO_2 content for igneous rocks from seven published studies. Circles in green and black represent magma closed to O_2. All triangles represent the whole rocks of systems open to O_2.

Fundamentally, isotopic fractionation of redox sensitive metals such as Fe is thought to be controlled by changes in the valence state of the element, reflecting changes in bond strength (e.g., Urey, 1947; Schauble et al., 2001; Schauble, 2004). However, observed isotopic variations in univalent elements such as Si or Mg in igneous rocks indicate that redox activity is not required (e.g., Teng et al., 2007; Zambardi et al., 2014). Theoretical predictions and spectroscopic measurements indicate that Fe^{3+}, which has a smaller ionic radius than Fe^{2+}, forms stronger bonds (Polyakov and Mineev, 2000; Schauble et al., 2001; Polyakov et al., 2007). Hence, Fe^{3+}-rich phases should preferentially incorporate heavy Fe isotopes relative to Fe^{2+}-rich phases. Recent high-temperature experimental studies of Fe isotope fractionation at magmatic conditions between mineral phases (e.g., fayalite-magnetite; Shahar et al., 2008) and mineral-melt (e.g., pyrrhotite-rhyolite; Schuessler et al., 2007) support this prediction. These experimental data have significantly advanced our understanding of Fe isotope fractionation during magmatic differentiation; however, to our knowledge, there are no experiments investigating the role of volatile phases in fractionating Fe isotopes in magmatic systems (Young et al., 2015). There are also presently no direct measurements of the magnetite-melt fractionation factor. Considering the seemingly ubiquitous presence of volatile phases and magnetite in magmatic systems and the demonstrated ability of magmatic-hydrothermal fluids to mobilize Fe (Simon et al., 2004), the absence of these data significantly limits our ability to use Fe isotope compositions of igneous rocks to decipher magmatic processes. It has been demonstrated experimentally that magmatic-hydrothermal fluids transport Fe as neutral $FeCl_2^0$ (Chou and Eugster, 1977; Boctor et al., 1980; Simon et al., 2004; Bell et al., 2011), and Heimann et al. (2008) hypothesized that $FeCl_2^0$ should be enriched in ^{54}Fe so that a Fe^{2+}-enriched aqueous fluid would preferentially scavenge lighter Fe isotopes from silicate melt. This could result in the

heavy Fe isotope ratios measured in high-silica igneous rocks that preserve evidence for the loss of a magmatic-hydrothermal fluid (Heimann et al., 2008). If fluid loss is a Rayleigh-like process, then removing an isotopically light fluid should yield a silicate melt that has a progressively heavier Fe isotope ratio that is proportional to the amount of fluid loss.

In this contribution, we report experimental data that quantify the equilibrium Fe isotopic fractionation between phases in a magnetite-aqueous fluid assemblage and a magnetite-aqueous fluid-rhyolite melt assemblage. Our data allow quantitative assessment of the role of volatile loss and fractional crystallization of magnetite in moderating Fe isotope fractionation in magmatic and magmatic-hydrothermal systems.

2.2. EXPERIMENTAL PROCEDURE

Starting Materials

Natural magnetite from Mineville, New York, was used in all experiments, which are summarized in Table 2.1. The chemical composition of the magnetite was characterized by using Electron Probe Microanalysis (EPMA) to perform a wavelength dispersive spectroscopy (WDS) scan of multiple grains. The magnetite is end-member Fe_3O_4. Grains were visually inspected by using a microscope at ~40x magnification, then crushed and sieved to a size range of 20 to 32 μm. This size range was selected based upon published data for Fe self-diffusion in magnetite, which is the rate-limiting step for equilibration in our experiments (Dieckmann and Schmalzried, 1977; length scale of diffusive equilibration is discussed in section 2.2.3). Synthetic haplogranite glass (Table 2.2) was used as the starting glass in magnetite-fluid-melt experiments. A 10 wt.% NaCl equivalent solution (molar KCl:NaCl:HCl = 1:1:1) was used in magnetite-fluid runs and a 1.8 wt.% NaCl equivalent solution was used in magnetite-fluid-melt runs (Table 2.1). These fluid compositions are representative of fluids exsolved from silicate melts in natural magmatic

systems (cf. Audétat and Simon, 2013; Bodnar et al., 2014) and exist as a single phase rather than brine plus vapor at the experimental conditions of this study (Bodnar et al., 1985; Chou et al., 1992; Bodnar et al., 2014; Steel-MacInnis et al., 2015). For magnetite-fluid experiments, we also used the three-isotope method to assess equilibrium, as discussed in detail in section 3.3.

Experimental Methods

Capsule Material

One challenge in running experiments with Fe-bearing assemblages is that Fe can be lost to the metal capsule. Gold capsules absorb less Fe than other metals and metal alloys, but Ratajeski and Sisson (1999) demonstrated that there is measurable Fe loss to Au capsules when conducting experiments at magmatic temperatures. We used EPMA-WDS to quantify the concentration of Fe in post-run Au capsules and unused Au tubing. The 1-sigma limit of detection for these analyses was calculated as ~97 ppm based on counting statistics, and no measurable Fe peak was detected in any of the samples. If we assume that the Au capsule contained this upper limit of 97 ppm Fe, and each capsule contains ~1g of Au, then a maximum of 2.5% of the total Fe contained in the magnetite-fluid and magnetite-fluid-melt assemblages may be lost to the capsule over the course of each run. This assumes that the entire Au capsule diffusively equilibrated with Fe, which is also an upper limit and ignores any possible diffusion profile for Fe in the Au capsule. Although one could in principle measure the isotopic composition of the Au capsule, this task is quite difficult given the separation steps typically employed for Fe isotope analyses and is beyond the scope of this work. Rather, to assess the possible effect of Fe loss to the Au capsule on the reported isotope fractionation factors, we performed a mass balance calculation for Fe isotope abundances in each phase assemblage. The mass balance results, reported in section 4.3, indicate that the starting and final phase assemblage

have statistically the same δ^{56}Fe value. This demonstrates that the loss of Fe to the Au capsule does not affect the calculated Fe isotope fractionation factors reported here.

Capsule configurations and experimental equipment

Two experimental designs were employed. The first included two phases: magnetite and fluid. Approximately 5 mg of magnetite and exactly 100 μL of ^{54}Fe-spiked, 10 wt.% NaCl eq. aqueous fluid were added to each capsule. Charges were welded inside triple-crimped gold capsules (5 mm OD, 0.2 mm wall thickness), weighed prior to experimentation, and then loaded into René-41 cold seal pressure vessels and held at 800°C and 150 MPa for the run durations specified in Table 2.1.

A double-capsule configuration was used to assess Fe isotope fractionation in a magnetite-fluid-melt assemblage at 800°C and 100 MPa. This double-capsule method physically, but not chemically, isolated the melt from the magnetite and allowed us to recover the run product melt as a single cylinder of glass (Figure 2.2). Inside a capsule of the same dimensions as the two-phase runs, a smaller (1.6 mm OD, 0.127 mm wall thickness, ~10 mm length) Au capsule was bottom welded and ~25 mg of the powdered starting glass was tamped down inside this capsule. The powdered glass was tamped in order to minimize porosity and air bubbles that might form as the glass melted. This capsule was crimped at the top but not welded, allowing chemical transport by the fluid phase through this one crimped end. Magnetite and 1.8 wt.% NaCl eq. aqueous fluid were added to the outer capsule before it was triple-crimped and welded shut on both ends. At run conditions, the vapor occupied all open space inside the charge, including the open top of the inner capsule. At the end of the run, the silicate melt quenched to a glass and the aqueous fluid and magnetite crystals remained separate within the outer capsule.

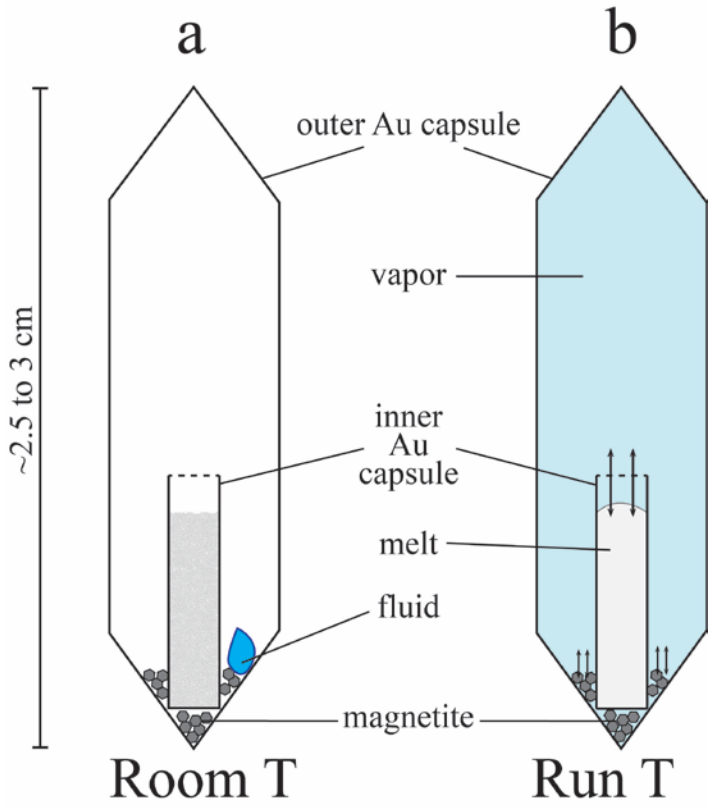

Figure 2.2: Capsule configuration for three-phase runs. This schematic diagram depicts at approximate scale the double-capsule method at room (A) and run temperature (B). The dashed line of the top of the inner capsule denotes a crimped, not welded, closure. Arrows in B represent iron transport between mineral and fluid as well as melt and fluid. The melt column is in contact with the walls of the inner capsule at run conditions, and the aqueous fluid occupies the entire available volume of the inner and outer capsule that is not occupied by magnetite and melt.

Omega type-K Chromel-Alumel thermocouples were used to measure temperature. Pressure was measured daily by using a pressure gauge that was calibrated against a factory-calibrated Heise gauge. The René-41 vessels were pressurized with water, which reacted with the inner walls of the nickel alloy vessel to buffer fO_2 at ~NNO. We note that the fO_2 of the vessels used in this study has been measured by using the technique of Chou (1978), and sensor capsules filled with Ni and NiO have been used to verify that the fO_2 is equivalent to NNO. The inner wall of the pressure vessel is mechanically abraded after each run to ensure that no coating builds up on the vessel wall, which would change the fO_2 of the run. The temperature difference along the ~2.5 cm long capsule was a maximum of 5-7°C. This gradient, as well as thermal convection,

was minimized by inclining the experimental furnaces to about +7° from the horizontal lab bench (cf. Charles and Vidale, 1982).

All experiments were quenched by removing the vessel from the furnace and blowing compressed air across its surface until it reached ~200°C, at which time it was immersed in a room-temperature water bath. The melt was cooled through the glass transition temperature in approximately 30 seconds, and previous studies have demonstrated that this quench time is sufficient to preserve the chemical integrity of phases at run conditions (Frank et al., 2002; Simon et al., 2004). Capsules were removed from the pressure vessel, weighed, and inspected optically for mechanical failure. All capsules maintained a constant mass before and after the run (±0.3 mg or less), which is consistent with the absence of mechanical failure. Capsules were punctured with a razor blade and opened by using non-magnetic tweezers. Aqueous fluid was drawn from the capsule using a syringe. The recovered fluid was examined by using a binocular microscope, and any stray magnetite grains observed were removed by using a magnet. In runs performed by using the double capsule configuration, the inner capsule was pried open with tweezers and cut with a razor to remove the glass cylinder (i.e., quenched melt), which was inspected under the microscope. Optical examination of the glass cylinder from each run indicated that the melts were crystal-free, and chemical analyses (described in section 3.1) of the glass cylinders indicate that the melt equilibrated chemically with the aqueous fluid and magnetite.

Run durations based on Fe self-diffusion data

For all experiments, we performed time series runs to assess the approach to steady-state conditions. Run durations were established by using data for the self-diffusion of Fe in magnetite, which was assumed to be the rate-limiting step for equilibrium in our experimental

assemblages owing to the faster diffusivities of Fe in silicate liquid and aqueous fluid (Dieckmann and Schmalzried, 1977; Van Orman and Crispin, 2010). Magnetite grains that measure 20 to 32 μm in diameter were calculated to reach equilibrium with respect to Fe isotopes in ~33 days at 800°C, 100 MPa, and fO_2 ~NNO. Electron probe microanalyses (EPMA) along the entire length of glass (melt) cylinders (see section 4.1) recovered from three-phase experiments indicate that they were compositionally homogeneous with respect to all elements (Table 2.2), including Fe and Cl that were initially contained only in the magnetite and fluid, respectively (Table 2.3). Behrens et al. (2012) reported experimental data for self- and chemical-diffusion of Fe in hydrous rhyolitic melts that demonstrate that self-diffusion is 0.16 log units faster than chemical diffusion. Thus, the attainment of bulk chemical equilibrium and homogeneous Fe distribution of the rhyolitic melt is interpreted to indicate that the melt reached steady-state conditions with respect to Fe isotope abundances.

2.3. ANALYTICAL METHODS

Glass Analyses

The bulk composition of run product rhyolitic glasses in the magnetite-fluid-melt experiments was quantified using EPMA-WDS to perform line traverses along the length of the recovered glass cylinder (Tables 2.2, 2.3). We used an accelerating voltage of 20 keV, a 5 nA Faraday cage current, and a de-focused beam diameter of 15 μm. We followed the protocol outlined in Morgan and London (1996) and Acosta-Vigil et al. (2003) to minimize, if not altogether eliminate, Na migration and concomitant Si and Al burn-in that may effect the analysis of hydrous aluminosilicate glasses. The EPMA wt.% oxide totals indicate that the melt contains about 6-7 wt.% H_2O, which is consistent with data reported for this melt composition at these P-T conditions (Bell et al., 2009).

MC-ICP-MS Analyses

Sample preparation

All run products and starting materials were digested in Optima Grade acid (glasses in $HF+HNO_3$; fluids and magnetite in aqua regia) and processed via column chromatography following the procedure of Huang et al. (2011), by using AG1-X8 ion exchange resin and HCl media. The glass and fluid recovered from each experiment were each analyzed (separately) as a single sample owing to the low total quantity of Fe in these phases; i.e., it was not possible to obtain more than 2 or 3 measurements from run products of individual experiments. United States Geological Survey rock powder standard BCR-2 was processed identically for quality assurance.

Double spike method

All Fe isotope analyses were performed by using a Nu Plasma HR MC-ICPMS at the University of Illinois, Urbana-Champaign. Mass resolution was >6000 and samples were run in dry plasma mode using a DSN-100. A double spike solution of ^{57}Fe-^{58}Fe was added to the samples (run products from three-isotope experiments were treated differently, see next section) prior to analysis to correct for instrumental mass bias and increase precision, following Millet et al. (2012). Results and analytical error are reported in Tables 2.4, 2.5, and 2.6 as $\delta^{56}Fe$ (and for three-isotope experiments, also $\delta^{57}Fe$) defined as:

$$\delta^{\#\#}Fe\ (‰) = \frac{(^{\#\#}Fe/^{54}Fe)_{sample} - (^{\#\#}Fe/^{54}Fe)_{IRMM\text{-}14}}{(^{\#\#}Fe/^{54}Fe)_{IRMM\text{-}14}} * 1000 \qquad (2.1)$$

where ## is 56 or 57, depending on the measured mass. Each $\delta^{56}Fe$ and $\delta^{57}Fe$ value is the average of 2 or 3 measurements. IRMM-14 was run between every sample analysis to further correct mass bias drifts within the run session (Millet et al., 2012). Corrections for isobaric

interferences from Ni and Cr were negligible, but measured in their own analytical routine and applied to all double spike data, including those from three-isotope experiments. The average value of BCR-2 during 4 independent sessions over the course of 2.5 months was 0.07 ±0.02‰ (1SE, n=14). Based on reproducibility on processed rock standards (including BCR-2, reported here) and the average standard deviation obtained from our 2 to 3 analyses per sample, estimated 2σ precision is 0.04‰.

Standard-sample bracketing for three-isotope method run products

Chemical processing for three-isotope method run products was identical to that used for other samples. However, the MC-ICP-MS analyses were performed using the standard-sample bracketing technique since non-mass dependent $\delta^{57}Fe$ changes cannot be accounted for using a double spike. To do this, each sample was analyzed at least 2 times between measurements of the IRMM-14 standard and the $\delta^{56}Fe_{sample}$ and $\delta^{57}Fe_{sample}$ values were calculated relative to the $^{56}Fe/^{54}Fe$ and $^{57}Fe/^{54}Fe$ of the IRMM-14 measured immediately before and after. Chromium was measured to correct for ^{54}Cr, although all corrections were negligible. Precision on standard-sample bracketing analyses is 0.05‰.

The Three-Isotope Method

The three-isotope method was used to directly determine the equilibrium isotopic fractionation factors of the magnetite-fluid experiments and to assess whether the $\delta^{56}Fe$ values calculated from measured Fe isotope ratios in phases from non-three-isotope experiments reflect equilibrium values. The three-isotope method works on the principle that by spiking one phase of a two-phase experiment (e.g., spiking the fluid in a magnetite-fluid run) with one of the isotopes of Fe (e.g., ^{54}Fe), the measured change in $\delta^{56}Fe$ vs. $\delta^{57}Fe$ of the run products can be used to calculate an equilibrium isotope fractionation factor even in the case where kinetics prevented

the attainment of equilibrium (cf. Matsuhisa et al., 1978; Shahar et al., 2008). In our study, the starting aqueous fluid was enriched in ^{54}Fe such that δ^{56}Fe and δ^{57}Fe were -15.36 ±0.17‰ and -16.62 ±0.29‰, respectively. The three-isotope experiments were quenched after varying lengths of time (Table 2.6), producing time series data that reflect changes in the Fe isotope ratios of each phase as the system approached equilibrium. The isotopic compositions of all run products were plotted as δ^{56}Fe vs. δ^{57}Fe. The convergence of these values through graphic projection to a Secondary Fractionation Line (SFL) yields the predicted equilibrium isotope ratios (i.e., δ^{56}Fe and δ^{57}Fe) for these two phases at run conditions and thus the equilibrium fractionation factor. The SFL has the same slope ($\gamma = 0.67795$, equation 2.3) as the mass dependent Terrestrial Fractionation Line (TFL) but with an offset in intercept based on the amount of ^{54}Fe spike added to the system.

$$\gamma = \frac{(1/m_{56}) - (1/m_{54})}{(1/m_{57}) - (1/m_{54})} = 0.67795 \qquad (2.3)$$

2.4. RESULTS

Fractionation factors for all experiments were calculated according to equation 2.4:

$$\Delta^{\#\#}Fe_{A\text{-}B}\ (‰) = \delta^{\#\#}Fe_A - \delta^{\#\#}Fe_B \qquad (2.4)$$

where ## refers to ^{57}Fe or ^{56}Fe. These data are reported in Table 2.5 and 2.6. Errors for three-isotope and three-phase experiment $\Delta^{\#\#}Fe_{A\text{-}B}$ values were calculated by using equation 2.5:

$$\sigma = (\sigma_A^{\,2} + \sigma_B^{\,2})^{1/2} \qquad (2.5).$$

Magnetite-Fluid-Melt Experiments

We report results for magnetite-fluid-melt experiments (800°C, 100 MPa, fO_2 ~ NNO) with durations of 6, 20, and 26 days (Table 2.4). The starting δ^{56}Fe value of the magnetite was -0.92 ±0.02‰. The starting isotopic composition of the fluid and melt were not measured due to negligible amount of Fe in these starting materials (i.e., the starting fluid contained no Fe while

the starting glass contributed only ~0.06 mg of Fe to the capsule compared to ~3.6 mg contributed by magnetite). Based on reported data for the Fe concentration of a magnetite-saturated aqueous fluid in a magnetite-fluid-rhyolitic melt assemblage at identical run conditions (Simon et al., 2004), the Cl-bearing fluid in runs at 100 MPa and 800°C contained ~1,900 ppm Fe. As mentioned above, measured chemical homogeneity along the length of the glass run products is assumed to indicate the attainment of steady-state conditions with respect to Fe isotope abundances in the rhyolitic melt. Therefore, the measured fractionation factors in the longest duration (26 days) experiments are: $\Delta^{56}Fe_{magnetite\text{-}fluid}$ = 0.75‰ ±0.08, $\Delta^{56}Fe_{magnetite\text{-}melt}$ = 0.95‰ ±0.05, and $\Delta^{56}Fe_{melt\text{-}fluid}$ = -0.20‰ ±0.07. These data indicate that magnetite preferentially incorporates heavier Fe isotopes relative to both the aqueous fluid and rhyolitic melt, and that aqueous fluid preferentially incorporates heavier Fe isotopes relative to co-existing rhyolitic melt.

It is important to note that the fluid composition was different for the two types of experiments (magnetite-fluid vs. magnetite-fluid-melt) with aqueous fluids containing 2 wt.% Fe and 1,900 ppm Fe, respectively. Thus, the differences in the fractionation factors themselves between types of experiments may be an effect of solution composition and the presence of the rhyolitic melt in those experiments.

Magnetite-Fluid Three-Isotope Experiments

The $\delta^{56}Fe$ and $\delta^{57}Fe$ values of the fluid and magnetite as a function of run duration are reported in Table 2.6 and plotted in Figure 2.3. The 10 wt.% NaCl eq. aqueous fluid in these two-phase experiments at 150 MPa and 800°C contained ~2 wt.% Fe, based on magnetite solubility data reported for a nearly identical phase assemblage (Simon et al., 2004). Importantly, Simon et al. (2004) demonstrated that the Fe content of a quenched Fe-bearing aqueous fluid

represents the Fe content of the fluid at run conditions. Taking into account the relative contributions of Fe from each run product phase (~20% and ~80% from the fluid and magnetite, respectively), the y-intercept of the SFL for these experiments was shifted by $\delta^{56}Fe$ = -0.19‰ relative to the TFL.

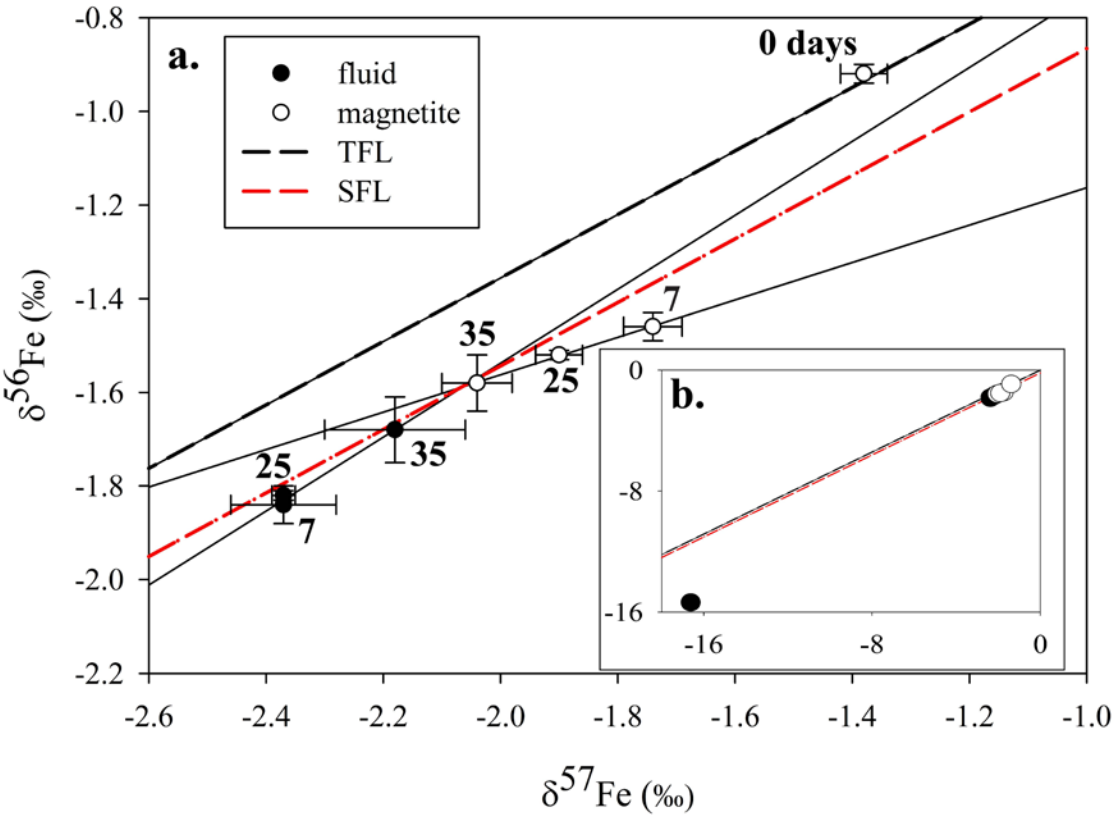

Figure 2.3: Results of time-series experiments displayed in $\delta^{56}Fe$ v. $\delta^{57}Fe$ space, following the three-isotope method of Matsuhisa et al. (1978). The black dashed line denotes the terrestrial fractionation line (TFL), and the red dashed line is the secondary fractionation line (SFL). Panel A shows the experimental run product data, associated 2σ error bars, and solid black lines that indicate projection through the data to the SFL. Panel B (inset), has significantly expanded ordinate and abscissa to show values of $\delta^{56}Fe$ v. $\delta^{57}Fe$ for the starting fluid (black dot at (-16.62‰, -15.36‰) and magnetite at (-1.38‰, -0.92‰)). In panel B, error bars are smaller than the size of the data points.

Regressing the data for different time experiments, the calculated equilibrium isotopic composition of each phase at 800°C is: $\delta^{56}Fe_{fluid}$ = -1.67‰ and $\delta^{57}Fe_{fluid}$ = -2.20‰; $\delta^{56}Fe_{magnetite}$ = -1.57‰ and $\delta^{57}Fe_{magnetite}$ = -2.05‰. These values are within error of those for the longest-duration (35 days) three-isotope experiment: $\delta^{56}Fe_{fluid}$ = -1.68 ±0.07‰, $\delta^{57}Fe_{fluid}$ = -2.18

±0.12‰; $\delta^{56}Fe_{magnetite}$ = -1.58 ±0.06‰, $\delta^{57}Fe_{magnetite}$ = -2.04 ±0.06‰. Therefore, the calculated fractionation factors for the magnetite-fluid assemblage at 150 MPa and 800°C are $\Delta^{56}Fe_{magnetite\text{-}fluid}$ = 0.10 ±0.09‰, and $\Delta^{57}Fe_{magnetite\text{-}fluid}$ = 0.14 ±0.13‰. The agreement between regression based equilibrium isotope ratios and those calculated from the longest duration magnetite-fluid-melt experiments (described in section 4.1) indicates that run durations were sufficient to attain equilibrium.

Assessing Fe Loss to the Au Capsule

We calculated the mass balance of Fe isotopes in the magnetite-fluid-melt assemblage and found that the $\delta^{56}Fe$ of the experimental system displays no statistically significant change from its starting composition after 26 days. All of the Fe in the system was initially contained in the starting magnetite, which has a $\delta^{56}Fe$ value of -0.92 ±0.02‰. There is no Fe detectable by MC-ICP-MS in the starting aqueous fluid (0 wt.% Fe) or the starting silicate glass (~0.06 mg Fe_{total}). The run products of the longest experiments yield $\delta^{56}Fe_{magnetite}$ = -0.89 ±0.01‰, $\delta^{56}Fe_{melt}$ = -1.84 ±0.05‰, $\delta^{56}Fe_{fluid}$ = -1.64 ±0.07‰. Taking into account the mass proportion of each phase (i.e., the melt contributes ~2% of the Fe_{total}, magnetite contributes ~93%, and fluid contributes ~5%) within the experimental system, and their measured $\delta^{56}Fe$ compositions, the $\delta^{56}Fe$ of the run product experimental system is -0.94‰, within error of the starting value. This mass balance exercise follows equation 2.6:

$$\delta^{56}Fe_{system} = X_{melt} * \delta^{56}Fe_{melt} + X_{mgt} * \delta^{56}Fe_{mgt} + X_{fluid} * \delta^{56}Fe_{fluid} \qquad (2.6)$$

where X is the proportion of total Fe mass in the experimental system contributed by the phase noted in subscript. This calculation demonstrates that the $\delta^{56}Fe$ of the initial phase assemblage is statistically the same as the $\delta^{56}Fe$ of the final phase assemblage. We interpret these mass balance results to indicate that Fe loss to the capsule did not affect the reported isotopic fractionation

factors. However, if the difference of -0.02‰ between the initial and final isotopic composition of the system actually reflects loss of Fe to the capsule walls, we can assume that lighter isotopes are lost to the Au capsule as they should diffuse through Au faster than heavier isotopes. In this case, preferential loss of lighter isotopes to the Au capsule would make the δ^{56}Fe values of all phases isotopically heavier. Iron diffuses the slowest through magnetite and therefore magnetite loses Fe more slowly to the capsule than the fluid and melt, which would likely bias the melt and fluid to relatively lighter isotope ratios than the magnetite. Since we measured the melt and fluid phases to be isotopically lighter, not heavier, than co-existing magnetite, the true magnetite-melt and magnetite-fluid fractionation factors would actually be larger than our measured values if our data reflect effects of the presence of the Au capsule. Thus, the result that magnetite is heavy relative to fluid and melt is robust.

2.5. DISCUSSION OF EXPERIMENTAL RESULTS

The new data reported here demonstrate that magnetite preferentially incorporates isotopically heavy Fe isotopes relative to co-existing rhyolitic melt and aqueous fluid, such that $\delta^{56}Fe_{magnetite} > \delta^{56}Fe_{fluid} > \delta^{56}Fe_{melt}$ (Tables 2.4, 2.5, 2.6). In Figure 2.4, our data are compared to the isotope fractionation factors for magnetite-fluid, magnetite-melt, and melt-fluid assemblages calculated from theory-based models, which relied on low-temperature experimental measurements and *ab initio* calculations to predict the magnitude of stable Fe isotope fractionation at high-temperature (e.g., Polyakov & Mineev, 2000; Schauble et al., 2001; Polyakov et al., 2007). We highlight that the published model results for Fe isotope fractionation at magmatic conditions had to assume that Fe is present in high-temperature magmatic-hydrothermal aqueous fluid as $FeCl_4^{2-}$, because no high temperature spectroscopic data exist at present; hence, these models used data for $FeCl_4^{2}$ from low-temperature, sub-critical conditions

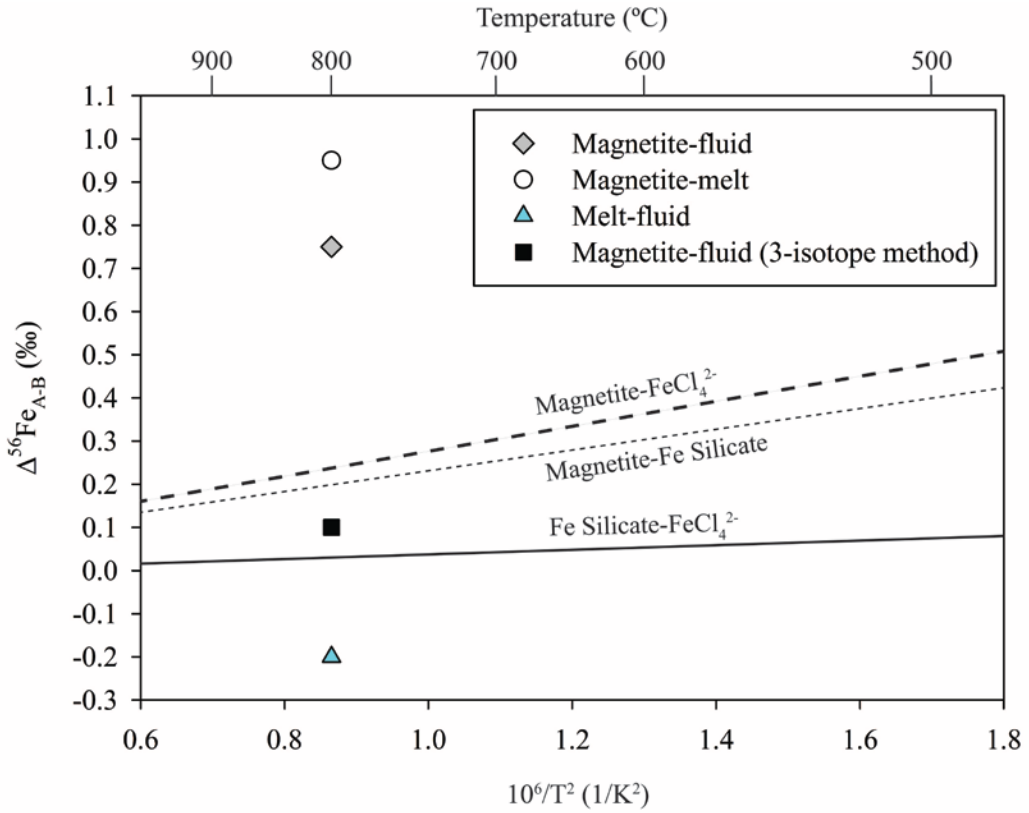

Figure 2.4: Experimentally-determined fractionation (Δ) factors derived from the three-phase and three-isotope experiments of the current study are plotted relative to theoretical predictions calculated and compiled by Heimann et al. (2008). The solid line is a proxy for melt-fluid fractionation factors, considering Fe isotope fractionation between Fe silicate and aqueous fluid containing $FeCl_4^{2-}$. The dotted line denotes Fe isotope fractionation between magnetite and Fe silicate, again a proxy for melt. The dashed line plots theoretical fractionation factors between magnetite and fluid containing $FeCl_4^{2-}$. The magnetite-fluid-melt experiments (magnetite-fluid: gray diamond; magnetite-melt: open circle; melt-fluid: blue triangle) were run at 800°C, 100 MPa, ~NNO, and contained a 1.8 wt.% equivalent NaCl aqueous fluid (NaCl:KCl:HCl = 1), which itself contained ~1,900 ppm Fe. The magnetite-fluid (black square) three-isotope experiments were run at 800°C, 150 MPa, ~NNO, and contained a 10 wt.% equivalent NaCl aqueous fluid, which itself contained 20,000 ppm Fe. The significant decrease in the value of $\Delta^{56}Fe_{magnetite\text{-}fluid}$ reflects the concentration and coordination of $FeCl_2$ in the fluid, as discussed in the text.

(Polyakov and Mineev, 2000; Schauble et al., 2001). Notably, experimental data indicate that from 400 to 800ºC, Fe is present as the neutral $FeCl_2^0$ complex in Cl-bearing aqueous fluid (Chou and Eugster, 1977; Simon et al., 2004). This is consistent with data for other dissolved aqueous metal-halide species that indicate that low-charge and fully associated neutral species are more abundant with increasing temperature, owing to the decrease of electrostatic shielding as the dielectric field decreases significantly (Eugster, 1986). Thus, we suggest that the

discrepancy between the predicted value of $\Delta^{56}Fe$ and the values determined experimentally in our study likely reflects differences in the Fe-speciation used for *ab initio* models (i.e., $FeCl_4^{2-}$) and those that actually exist in high-temperature Cl-bearing aqueous fluid (i.e., $FeCl_2^0$).

We also observe differences in Fe isotope fractionation between experiments containing only magnetite and a 10 wt.% NaCl eq. fluid, and experiments that contained magnetite, melt, and a 1.8 wt.% NaCl eq. fluid. The Fe content of these fluids differs by an order of magnitude, increasing from ~0.19 wt.% Fe in a 1.8 wt.% NaCl eq. fluid to ~2 wt.% Fe in a 10 wt.% NaCl eq. fluid (Simon et al., 2004). We suggest that the measured difference in $\Delta^{56}Fe_{melt\text{-}fluid}$ (Table 2.5) for fluids of different salinities is controlled by the total Fe content of the fluids, which in turn is controlled by the abundance of Cl in the aqueous fluid as increasing chlorinity allows the fluid to scavenge more Fe from magnetite and silicate melt (Simon et al., 2004; Zajacz et al., 2012). This experimental observation demonstrates the importance of fluid composition (e.g., $FeCl_2^0$ content) on the evolution of the stable Fe isotope composition of a magmatic system, a finding that is consistent with the fluid exsolution model prediction of Heimann et al. (2008).

Similarly from a redox perspective, our melt-fluid data, which were equilibrated at fO_2 of ~NNO, are unexpected because 22% of the Fe in the rhyolitic melt is calculated to be Fe^{3+}, whereas all of the Fe in the fluid is Fe^{2+}, as discussed above. The $Fe^{3+}/\Sigma Fe$ ratio of the experimental rhyolitic melt was calculated by using the method of Kress and Carmichael (1991). If oxidation state is the fundamental control on Fe isotope fractionation, the rhyolitic melt should be isotopically heavier than the coexisting fluid (Schauble, 2001). That we measure the opposite is proposed to result from the importance of coordination and bonding preferences of Fe in each phase, which may overcome redox controls of Fe isotope fractionation between silicate melt and co-existing Cl-bearing aqueous fluid. Published Mössbauer spectroscopic data for Fe-bearing

silicate glasses indicate that ferric Fe can be tetrahedrally or octahedrally coordinated in a silicate melt that has a $Fe^{3+}/\Sigma Fe$ ratio of 0.3-0.5, whereas ferrous Fe is probably octahedrally coordinated (Mysen et al., 1985). If $FeCl_2^0$ is the only Fe-chloride species present in the aqueous phase, then the Fe in the fluid is tetrahedrally coordinated (Eugster, 1986). Heavy isotopes tend to become concentrated in phases where the isotopes can have a lower coordination number (e.g., Bigeleisen and Mayer, 1947; Schauble, 2004). This behavior has been demonstrated experimentally for B isotope fractionation between silicate melt and aqueous fluid (Hervig et al., 2002), in which case the melt is isotopically lighter than the fluid due to the preference of ^{11}B for trigonal coordination in the fluid, and ^{10}B for tetragonal coordination in silicate melt. Thus, the empirical finding in the present study that heavy Fe isotopes prefer Cl-bearing aqueous fluid relative to coexisting rhyolitic melt, which has a $Fe^{3+}/\Sigma Fe$ ratio of ~0.22, is consistent with our knowledge of melt and fluid structures, as well as observations of B isotope partitioning.

2.6. IRON ISOTOPE FRACTIONATION IN NATURAL SYSTEMS

The fractionation factors determined in this study indicate that both magnetite crystallization and exsolution of a Cl-bearing aqueous fluid decrease the $\delta^{56}Fe$ and $\delta^{57}Fe$ of coexisting rhyolitic melt. The mechanical separation of phases having different isotope ratios leads to a Rayleigh distillation process following equation 2.7:

$$R = R_0 + 1000 * (\alpha - 1) * \ln (F) \qquad (2.7)$$

where R is the calculated $^{56}Fe/^{54}Fe$ ratio, R_0 is the initial $^{56}Fe/^{54}Fe$ ratio, α is the fractionation factor, and F is the fraction of Fe remaining in the melt.

In a volatile-saturated magnetite-free magma, volatile exsolution should drive the composition of rhyolitic melt to progressively lighter $\delta^{56}Fe$ values as the aqueous fluid scavenges and removes heavier isotopes from the melt. This is illustrated in Figure 2.5, where a Rayleigh

model of either magnetite fractionation or exsolution and loss of a 1.8 wt.% NaCl eq. aqueous fluid containing ~0.2 wt.% Fe shift the residual Fe isotope composition of the rhyolitic melt to more negative values. These results graphically illustrate that magnetite fractionation has a much greater effect on decreasing δ^{56}Fe of the melt relative to volatile exsolution.

However, in natural systems, rhyolitic melts are almost ubiquitously saturated in magnetite. Hence, we also model the effects of volatile exsolution on the Fe isotope composition of a magnetite + rhyolitic melt magma. Two melt compositions were used: one with 1.5 wt.% FeO and a second with 5 wt.% FeO, while the modal abundance of magnetite varied from 0.06 to 0.1. The model results shown in Figure 2.5 indicate that progressive loss of a 1.8 wt.% NaCl eq. aqueous fluid, which contains ~0.2 wt.% Fe, increases the δ^{56}Fe of the magma (magnetite + rhyolitic melt). The results also indicate that δ^{56}Fe of the magma increases with increasing modal abundance of magnetite, despite the fact that the aqueous fluid is isotopically heavier than the rhyolitic melt. While this model does suggest consistency with observations, there are other factors to consider. For instance, if the Fe content of the fluid in equilibrium with the melt is just ≤0.2 wt.% Fe, considering the range of magmatic water contents from <0.5 wt.% to ~8 wt.% H_2O (Wallace, 2005), it would be difficult to remove enough Fe via fluid exsolution from the melt to significantly change the δ^{56}Fe.

Application of these model results to observational data (Figure 2.1) suggests that the increase of δ^{56}Fe with increasing silica content is consistent, at least in part, with fluid loss, provided that the magma was magnetite saturated (e.g., Poitrasson and Freydier, 2005; Heimann et al., 2008). However, other studies indicate that processes such as changes in oxidation state during crystallization may also affect δ^{56}Fe (e.g., Sossi et al., 2012). Additionally, Dauphas et al. (2014) measured the force constants of Fe bonds in silicate glasses and suggested that the change

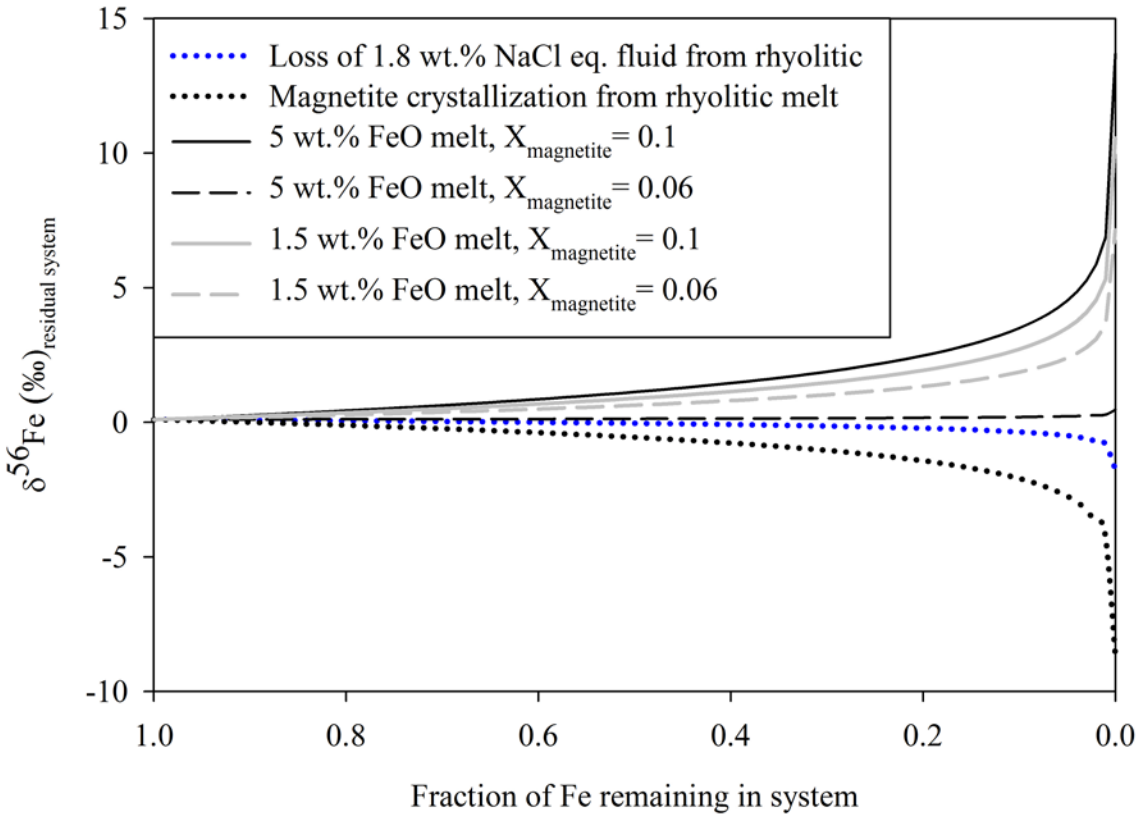

Figure 2.5: The results of Rayleigh fractionation models show the evolution of δ^{56}Fe of a residual rhyolitic melt and magnetite-rhyolitic melt magma during progressive fractionation of magnetite and loss of a $FeCl_2$–bearing aqueous fluid. Models incorporated fractionation factors calculated from the three-phase experimental data reported here. A remaining fraction of Fe indicates that no magnetite has been crystallized nor fluid exsolved from the melt, while a fraction of 0.0 represents the theoretical, yet unrealistic, situation in which all magnetite or fluid have been extracted. Model results indicate that at 800°C, 100 MPa, fO_2 ~NNO, the δ^{56}Fe value of a rhyolitic melt becomes progressively more negative (i.e., decreases in value) during magnetite fractionation (black dotted line) and the exsolution and loss of a 1.8 wt.% NaCl eq. aqueous fluid (blue dotted line). When considering a magnetite-rhyolitic melt magma, the model results indicate that the value of δ^{56}Fe increases with continued fluid loss, and notably that δ^{56}Fe increases more for high modal abundances of magnetite ($X_{magnetite}$ = 0.1 versus 0.06). See the text for details.

in $\delta^{56}Fe$ with silica is related to bonding structure of Fe in the melt and its effect on mineral-melt isotopic partitioning in high SiO_2 melts. Although Dauphas et al. (2014) used glasses as proxies for melts, they reported that the measured bonding characteristics (i.e., force constants) of Fe^{3+} and Fe^{2+} show a dramatic change in force constants for high silica melts (75% SiO_2) relative to lower silica melts, which indicates the potential importance of discrepancies in Fe coordination number in different phases, consistent with our inferred controls on melt-fluid fractionation factors. Cleary, more work is required to fully constrain the causes of Fe isotope fractionation during the evolution of magmatic systems, at magmatic-hydrothermal conditions. However, the experimental results reported here, with the implications of force constant data collected by Dauphas et al. (2014), are consistent with Fe bonding environment being an important control on Fe isotope fractionation (Urey, 1947; Schauble et al., 2004).

7. CONCLUSIONS

We report experimental data that quantify stable Fe isotope fractionation among silicate melt, magnetite, and Cl-bearing aqueous fluid of variable salinity and Fe content at 800°C, 100-150 MPa, and fO_2 ~NNO. The data are used to assess directly the effects of fluid exsolution and magnetite fractionation on the evolution of the stable Fe isotope composition of felsic magma. Major findings include:

1. Magnetite preferentially incorporates heavy Fe isotopes relative to both fluid and melt.
2. Rhyolitic melt is isotopically light relative to co-existing $FeCl_2$-bearing aqueous fluid.
3. The value of $\Delta^{56}Fe_{magnetite\text{-}fluid}$ decreases as the $FeCl_2$ content of the aqueous fluid increases.
4. The new experimentally determined $\Delta^{56}Fe$ values reported here are significantly higher than theoretically predicted $\Delta^{56}Fe$ values for high P-T conditions, which likely reflects the importance of the neutral $FeCl_2$ complex in magmatic-hydrothermal aqueous fluids.

5. Rayleigh fractionation of a $FeCl_2$-bearing aqueous fluid decreases the $\delta^{56}Fe$ of felsic silicate melt (considering melt as a distinct phase and not as synonymous with magma).
6. However, Rayleigh fractionation of a $FeCl_2$-bearing aqueous fluid from a magma that contains rhyolitic melt and magnetite increases the $\delta^{56}Fe$ of the magma, consistent with the excursion of $\delta^{56}Fe$ measured in high-silica, low-FeO, magnetite-saturated igneous rocks. The magnitude of change of $\delta^{56}Fe$ depends on the total Fe content of the melt and the modal abundance of magnetite. This finding is consistent with the conclusions of Poitrasson and Freydier (2005) and Heimann et al. (2008) both of whom interpreted data from natural magmatic systems to indicate that magnetite imposes a significant control on the evolution of $\delta^{56}Fe$ in felsic magmas.

Additional experimental data are needed to complement field and theoretical work to explore the effects of Cl-complexation and polymerization of Fe in the fluid, as well as the roles of crystal fractionation and oxygen fugacity on the evolution of the Fe isotope composition of silicate magmas.

ACKNOWLEDGEMENTS

This work was supported partially by National Science Foundation grant EAR-1264537. LB thanks the Society of Economic Geologists, the University of Michigan Rackham Graduate School, and the Earth & Environmental Sciences Turner Endowment for financial support. All authors thank Charles Lesher for a very helpful pre-submission review.

2.8. REFERENCES

Acosta-Vigil A., London D., Morgan G. B. and Dewers T. A. VI (2003) Solubility of excess alumina in hydrous granitic melts in equilibrium with peraluminous minerals at 700–800°C and 200 MPa and applications of the aluminum saturation index. *Contrib. Mineral. Petrol.* 146, 100–119.

Audétat, A. and Simon, A. (2013) Magmatic controls on porphyry Cu genesis. In: Economic Geology Monograph in honor of Richard Sillitoe. (Eds. J.W. Hedenquist, M. Harris, F.

Camus). *Society of Econ. Geol. Special Publication* **16**, 553-572.

Bell A. S., Simon A. C. and Guillong M. (2009) Experimental constraints on Pt, Pd and Au partitioning and fractionation in silicate melt-sulfide-oxide-aqueous fluid systems at 800°C, 150 MPa and variable sulfur fugacity. *Geochim. Cosmochim. Acta* **73**, 5778-5792.

Bell A.S., Simon A. and Guillong M. (2011) Gold solubility in oxidized and reduced, water-saturated mafic melt. *Geochim. Cosmochim. Acta* **75**, 1718-1732.

Bell A.S. and Simon A. (2011) Experimental evidence for the alteration of the $Fe^{3+}/\Sigma Fe$ of silicate melt caused by the degassing of chlorine-bearing aqueous volatiles. *Geology* **39**, 499-502.

Behrens, H., Kaltenbach, A., Horn, I. and Schüssler, J. (2012) Diffusion of iron in rhyolitic melts, 14th International Conference Experimental Mineralogy Petrology Geochemistry - EMPG (Kiel, Germany 2012).

Boctor, N.Z., Popp, R.K. and Frantz J.D. (1980) Mineral-solution equilibria—IV. Solubilities and the thermodynamic properties of Fe_2O_3 in the system Fe_2O_3-H_2–H_2O-HCl. *Geochim. Cosmochim. Acta* **44**, 1509–1518.

Bodnar R. J., Burnham C. W and Sterner S. M. (1985) Synthetic fluid inclusions in natural quartz. III. Determination of phase equilibrium properties in the system H_2O–NaCl to 1000 °C and 1500 bars. *Geochim. Cosmochim. Acta* **49**, 1861–1873.

Bodnar R.J., Lecumberri-Sanchez P., Moncada D. and Steele-MacInnis M. (2014) Fluid Inclusions in Hydrothermal Ore Deposits. *Treatise on Geochem. (2nd Ed.)* **11**, 119-142.

Charles R. W. and Vidale R. (1982) Temperature calibration of a new rapid quench vessel. *Am. Mineral.* **67**, 175-179.

Chou I. and Eugster H.P. (1977) Solubility of magnetite in supercritical chloride solutions, *Am. J. Sci.* **277**, 1296-1314.

Chou, I-M. (1978) Calibration of oxygen buffers at elevated P and T using the hydrogen fugacity sensor. *Am. Mineral.* **63**, 690-703.

Chou I.-M., Sterner S. M. and Pitzer K. S. (1992) Phase relations in the system NaCl KCl–H_2O: IV. Differential thermal analysis of the sylvite liquidus in the KCl–H_2O binary, the liquidus in the NaCl–KCl–H_2O ternary, and the solidus in the NaCl–KCl binary to 2 kb pressure, and a summary of experimental data for thermodynamic-PTX analysis of solid–liquid equilibria at elevated P–T conditions. *Geochim. Cosmochim. Acta* **56**, 2281– 2293.

Dauphas N., Roskosz M., Alp E.E., Neuville D.R., Hu M.Y, Sio C.K., Tissot F.L.H, Zhao J., Tissandier L., Médard and Cordier C. (2014) Magma redox and structural controls on iron isotope variations in Earth's mantle and crust. *Earth Planet. Sc. Lett.* **308**, 127-140.

Dieckmann R. and Schmalzried H. (1977) Defects and Cation Diffusion in Magnetite (I). *Berichte der Bunsengesellschaft für physikalische Chemie* **81**, 344-347.

Foden J., Sossi P.A. and Wawryk C.M. (2015) Fe isotopes and the contrasting petrogenesis of A-, I- and S-type granite. *Lithos*, doi:10.1016/j.lithos.2014.10.015.

Hill P.S., Schauble E.A. and Young E.D. (2010) Effects of changing gsolution chemistry on Fe^{3+}/Fe^{2+} isotope fractionation in aqueous Fe-Cl solutions. *Geochim. Cosmochim. Acta* **74**, 6669-6689.

Heimann A., Beard, B.L. and Johnson C.M. (2008) The role of volatile exsolution and sub-solidus fluid/rock interactions in producing high $^{56}Fe/^{54}Fe$ ratios in siliceous igneous rocks. *Geochim. Cosmochim. Acta* **72**, 4379-4396.

Hervig R.L., Moore G.M., Williams L.B., Peacock S.M., Holloway J.R. and Roggensack K. (2002) Isotopic and elemental partitioning of boron between hydrous fluid and silicate melt, *Am. Mineral.* **87**, 769-774.

Huang F., Chakraborty P., Lundstrom C.C., Holmden C., Glessner J.J.G., Kieffer S.W. and Lesher C.E. (2010) Isotope fractionation in silicate melts by thermal diffusion. *Nature* **464**, 396-400.

Huang F., Zhang Z., Lundstrom C.C. and Zhi X. (2011) Iron and magnesium isotopic compositions of peridotite xenoliths from Eastern China. *Geochim. Cosmochim. Acta* **75**, 3318-3334.

Kress V.C. and Carmichael I.S.E. (1991) The compressibility of silicate liquids containing Fe_2O_3 and the effect of composition, temperature, oxygen fugacity and pressure on their redox states. *Contrib. Mineral. Petrol.* **108**, 82-92.

Lundstrom C.C. (2009) Hypothesis for the origin of convergent margin granitoids and Earth's continental crust by thermal migration zone refining. *Geochim. Cosmochim. Acta* **73**, 5709-5729.

Matsuhisa Y., Goldsmith J.R. and Clayton R.N. (1978) Mechanisms of hydrothermal crystallization of quartz at 250°C and 15 kbar. *Geochim. Cosmochim. Acta* **42**, 173-182.

Millet M., Baker J. and Payne C. (2012) Ultra-precise stable Fe isotope measurements by high resolution multi-collector inductively coupled plasma mass spectrometry with a ^{57}Fe-^{58}Fe double spike. *Chem. Geol.* **304-305**, 18-25.

Morgan G. B.VI and London D. (1996) Optimizing the electron microprobe analysis of hydrous alkali aluminosilicate glasses. *Am. Mineral.* **81,** 1176-1185.

Poitrasson F. and Freydier R. (2005) Heavy iron isotope composition of granites determined by high resolution MC-ICP-MS. *Chem. Geol.* **222**, 132-147.

Polyakov V.B. and Mineev S.D. (2000) The use of Mössbauer spectroscopy in stable isotope geochemistry. *Geochim. Cosmochim. Acta* **64**, 849-865.

Polyakov V.B., Clayton R.N., Horita J. and Mineev S.D. (2007) Equilibrium iron isotope fractionation factors of minerals: Reevaluation from the data of nuclear inelastic resonant X-ray scattering and Mössbauer spectroscopy. *Geochim. Cosmochim. Acta* **71**, 3833-3846.

Ratajeski K. and Sisson T. (1999) Loss of iron to gold capsules in rock-melting experiments. *Am. Mineral.* **84**, 1521-1527.

Schauble E.A., Rossman G.R. and Taylor Jr. H.P. (2001) Theoretical estimates of equilibrium Fe-isotope fractionations from vibrational spectroscopy. *Geochim. Cosmochim. Acta* **65**, 2487-2497.

Schauble E.A. (2004) Applying stable isotope fractionation theory to new systems. *Rev. Mineral. Geochem.* **55**, 65-111.

Schuessler J.A., Schoenberg R., Behrens H. and von Blanckenburg F. (2007) The experimental calibration of the iron isotope fractionation factor between pyrrhotite and peralkaline rhyoltic melt. *Geochim. Cosmochim. Acta* **71**, 417-433.

Schuessler J.A., Schoenberg R. and Sigmarsson O. (2009) Iron and lithium isotope systematics of the Hekla volcano, Iceland—Evidence for Fe isotope fractionation during magma differentiation. *Chem. Geol.* **258**, 78-91.

Shahar A., Young E.D. and Manning C.E. (2008) Equilibrium high-temperature Fe isotope fractionation between fayalite and magnetite: An experimental calibration. *Earth Planet. Sc. Lett.* **268**, 330-338.

Simon A.C., Pettke T., Candela P.A., Piccoli P.M. and Heinrich, C.A. (2004) Magnetite solubility and iron transport in magmatic-hydrothermal environments. *Geochim. Cosmochim. Acta* **68**, 4905-4914.

Sossi P.A., Foden J.D. and Halverson G.P. (2012) Redox-controlled iron isotope fractionation during magmatic differentiation: an example from the Red Hill intrusion, S. Tasmania. *Contrib. Mineral. Petrol.* **164**, 757-779.

Steel-MacInnis M., Lecumberri-Sanchez P. and Bodnar R.J. (2015) Synthetic fluid inclusions XX. Critical PTx properties for H_2O-$FeCl_2$ fluids. *Geochim. Cosmochim. Acta* **148**, 50-61.

Telus M., Dauphas N., Moynier F., Tissot F. L.H., Teng F-Z., Nabelek P.I., Craddock P.R. and Groat L.A. (2012) Iron, zinc, magnesium and uranium isotopic fractionation during continental crust differentiation: The tale from migmatites, granitoids, and pegmatites. *Geochim. Cosmochim. Acta* **97**, 247-265.

Teng F., Wadhwa M. and Helz R.T. (2007) Investigation of magnesium isotope fractionation during basalt differentiation: Implications for a chondritic composition of the terrestrial mantle. *Earth Planet. Sc. Lett.* **261**, 84-92.

Teng F., Dauphas N. and Helz R.T. (2008) Iron isotope fractionation during magmatic differentiation in Kilauea Iki Lava Lake. *Science* **320**, 1620-1622.

Urey H.C. (1947) The Thermodynamic Properties of Isotopic Substances. *J. Chem. Soc. (London)* 562-581.

Van Orman J.A. and Crispin K.L. (2010) Diffusion in oxides. *Rev. Mineral. Geoch.* **72**, 757-825.

Wallace P. (2005) Volatiles in subduction zone magmas: concentrations and fluxes based on melt inclusion and volcanic gas data. *J. Volcanol. Geoth. Res.* **140**, 217-240.

Weyer S. (2008) What Drives Iron Isotope Fractionation in Magma? *Science Perspectives* **320**, 1600-1601.

Williams H.M., Peslier A.H., McCammon C., Halliday A.N., Levasseur S., Teutsch N. and Burg J.-P. (2005) Systematic iron isotope variations in mantle rocks and minerals: The effects of partial melting and oxygen fugacity. *Earth Planet. Sc. Lett.* **235**, 435-452.

Young E.D., Manning C.E., Schauble E.A., Shahar A., Macris C.A., Lazar C. and Jordan M. (2015) High-temperature equilibrium isotope fractionation of non-traditional stable isotopes: Experiments, theory, and applications. *Chem. Geol.* **395**, 176-195.

Zambardi T., Lundstrom C.C., Li X. and McCurry M. (2014) Fe and Si isotope variations at Cedar Butte volcano; insight into magmatic differentiation. *Earth Planet. Sc. Lett.* **405**, 169-179.

TABLES

Table 2.1. Summary of run conditions and description of phases for all experiments.

Run	Conditions		Fluid Composition			Phases	Duration (days)
	Temperature (°C)	Pressure (MPa)	wt.% NaCl equivalent	^{54}Fe added	Fe content of product fluid*		
LB-12	800	100	1.8	no	1,900 ppm	Mgt + Fl + Melt	6
LB-10	800	100	1.8	no	1,900 ppm	Mgt + Fl + Melt	20
LB-9	800	100	1.8	no	1,900 ppm	Mgt + Fl + Melt	26
LB-53	800	150	10	yes	20,000 ppm	Mgt + Fl	7
LB-56	800	150	10	yes	20,000 ppm	Mgt + Fl	25
LB-52	800	150	10	yes	20,000 ppm	Mgt + Fl	35

*The Fe content of the run product fluids was calculated by using magnetite solubility data from Simon et al. (2004).

Table 2.2. The compositions of starting synthetic haplogranite (HG) glass and the product glass from runs LB-10 and LB-12 (20 and 6 days, respectively, at 800°C, 100 MPa, ~NNO).

Oxide constituent	HG (wt.%)[a]	LB-10 (wt.%)[a,b]	LB-12 (wt.%)[a,b]
SiO_2	77.68	71.52	72.36
TiO_2	0.01	0.01	0.01
Al_2O_3	12.70	11.88	11.85
FeO	NA*	0.17	0.23
Fe_2O_3	0.28	NA	NA
MnO	NP**	0.01	0.01
MgO	NP	0.01	0.02
CaO	NP	0.05	0.06
Na_2O	4.49	3.26	3.45
K_2O	4.50	5.22	5.22
P_2O_5	NA	0.02	0.01
Cr_2O_3	NA	0.01	0.01
Total	99.66	92.34	93.39

[a]Concentrations for all glasses are the average for a minimum of 16 EPMA spot analyses. The concentration of Fe in all product glasses is reported as FeO.
[b]LB run product glasses were also analyzed for F and Cl (Table 2.3)
*NA = not analyzed
**NP = not present

Table 2.3. The concentrations of Cl and Fe in experimental run product glasses LB-10 and LB-12.

Spot*	Cl (wt.%)	Fe (wt.%)	Spot	Cl (wt.%)	Fe (wt.%)
LB10-1	0.16	0.22	**LB12-1**	0.28	0.40
LB10-2	0.18	0.24	**LB12-2**	0.17	0.22
LB10-3	0.11	0.16	**LB12-3**	0.15	0.15
LB10-4	0.13	0.12	**LB12-4**	0.12	0.15
LB10-5	0.12	0.20	**LB12-5**	0.14	0.19
LB10-6	0.14	0.22	**LB12-6**	0.17	0.29
LB10-7	0.15	0.17	**LB12-7**	0.11	0.23
LB10-8	0.13	0.14	**LB12-8**	0.13	0.27
LB10-9	0.14	0.14	**LB12-9**	0.13	0.31
LB10-10	0.14	0.13	**LB12-10**	0.16	0.38
LB10-11	0.15	0.13	**LB12-11**	0.17	0.40
LB10-12	0.12	0.14	**LB12-12**	0.15	0.37
LB10-13	0.16	0.13	**LB12top-1**	0.16	0.34
LB10-14	0.17	0.15	**LB12top-2**	0.13	0.09
LB10-15	0.15	0.19	**LB12top-3**	0.10	0.05
LB10-16	0.17	0.19	**LB12top-4**	0.15	0.07
			LB12top-5	0.13	0.10
			LB12top-6	0.15	0.13
LB-10 average	0.14	0.17	**LB-12 average**	0.15	0.23
1σ	0.02	0.04	**1σ**	0.04	0.12

*Individual points were chosen between the top and bottom of the cylinder to avoid poorly polished or vesicular areas.

Table 2.4. Data for magnetite-fluid-melt experiments at 800°C and 100 MPa, where the fluid contained ~1,900 ppm Fe.

Run	Duration (days)	$\delta^{56}Fe_{magnetite}$ (‰)	2σ*	$\delta^{56}Fe_{fluid}$ (‰)	2σ	$\delta^{56}Fe_{melt}$ (‰)	2σ
LB-12	6	-1.08	0.03	-1.20	0.06	-1.61	0.03
LB-10	20	-0.98	0.03	-1.67	0.16	-1.69	0.07
LB-9	26	-0.89	0.05	-1.64	0.07	-1.84	0.03

*2σ values are based on 2 or 3 measurements

1

Table 2.5. Data for magnetite-fluid-melt experiments at 800°C and 100 MPa, where the fluid contained ~1,900 ppm Fe.

Run	Duration (days)	$\Delta^{56}Fe_{magnetite\text{-}fluid}$ (‰)[a]	2σ*	$\Delta^{56}Fe_{magnetite\text{-}melt}$ (‰)	2σ	$\Delta^{56}Fe_{melt\text{-}fluid}$ (‰)	2σ
LB-12	6	0.12	0.06	0.53	0.04	-0.41	0.06
LB-10	20	0.69	0.16	0.71	0.07	-0.02	0.17
LB-9	26	0.75	0.09	0.95	0.05	-0.20	0.07

[a]Fractionation factors (Δ) were calculated by using the $\delta^{56}Fe$ values reported in Table 2.4.

*2σ uncertainties were calculated by using equation 2.5 in the text.

Table 2.6. Isotope fractionation data for the three-isotope magnetite-fluid time-series runs performed at 800°C and 150 MPa, where the fluid contained ~2 wt.% Fe.

Run	Duration (days)	$\delta^{57}Fe_{magnetite}$ (‰)	2σ	$\delta^{57}Fe_{fluid}$ (‰)	2σ	$\delta^{56}Fe_{magmetite}$ (‰)	2σ	$\delta^{56}Fe_{fluid}$ (‰)	2σ	$\Delta^{56}Fe_{magnetite\text{-}fluid}$ (‰)[a]	2σ
Start	0	-1.38*	0.03	-16.62	0.29	-0.92	0.02	-15.36	0.17		
LB-53	7	-1.74	0.05	-2.37	0.09	-1.46	0.03	-1.84	0.04	0.38	0.05
LB-56	25	-1.90	0.04	-2.37	0.02	-1.52	0.03	-1.82	0.03	0.30	0.04
LB-52	35	-2.04	0.06	-2.18	0.12	-1.58	0.06	-1.68	0.07	0.10	0.09

* The starting $\delta^{57}Fe_{magnetite}$ value was calculated from the measured $\delta^{56}Fe_{magnetite}$ value by assuming mass dependent fractionation since this analysis was performed with the double spike technique, which introduced a spike of ^{57}Fe-^{58}Fe into the sample.

[a]Fractionation factors (Δ) were calculated by using the $\delta^{56}Fe$ values reported here and the respective 2σ uncertainties were calculated by using equation 2.5 in the text.

CHAPTER III

Fe-O STABLE ISOTOPE PAIRS ELUCIDATE A HIGH-TEMPERATURE ORIGIN OF CHILEAN IRON OXIDE—APATITE DEPOSITS

ABSTRACT

Iron oxide–apatite (IOA) ore deposits occur globally and can host millions to billions of tons of Fe in addition to economic reserves of other metals such as rare earth elements, which are critical for the expected growth of technology and renewable energy resources. In this study, we pair the stable Fe and O isotope compositions of magnetite samples from several IOA deposits to constrain the source reservoir of these elements in IOAs. Since magnetite constitutes up to 90 modal% of many IOAs, identifying the source of Fe and O within the magnetite may elucidate high-temperature and/or lower-temperature processes responsible for their formation. We focus on the world-class Los Colorados IOA in the Chilean iron belt (CIB), and present data for magnetite from other Fe oxide deposits in the CIB (El Laco, Mariela). We also report Fe and O isotopic values for other IOA deposits, including Mineville, New York (USA) and the type locale, Kiruna (Sweden). The ranges of Fe isotopic composition (δ^{56}Fe, ^{56}Fe/^{54}Fe relative to IRMM-14) of magnetite from the Chilean deposits are: Los Colorados, δ^{56}Fe ($\pm$ 2σ) = 0.08 ± 0.03‰ to 0.24 ± 0.08‰; El Laco, δ^{56}Fe = 0.20 ± 0.03‰ to 0.53 ± 0.03‰; Mariela, δ^{56}Fe = 0.13 ± 0.03‰. The O isotopic composition (δ^{18}O, ^{18}O/^{16}O relative to VSMOW) of the same Chilean magnetite samples are: Los Colorados, δ^{18}O ($\pm$ 2σ) = 1.92 ± 0.08‰ to 3.17 ± 0.03‰; El Laco, δ^{18}O = 4.00 ± 0.10‰ to 4.34 ± 0.10‰; Mariela, δ^{18}O = (1.48 ± 0.04‰). The δ^{18}O and δ^{56}Fe values for Kiruna magnetite yield an average of 1.76 ± 0.25‰ and 0.16 ± 0.07‰, respectively.

The Fe and O isotope data from the Chilean IOAs fit unequivocally within the range of magnetite formed by high-temperature magmatic or magmatic-hydrothermal processes (i.e., δ^{56}Fe 0.06 to 0.49‰ and δ^{18}O = 1.0 to 4.5‰), consistent with a high-temperature origin for Chilean IOA deposits. Additionally, minimum formation temperatures calculated by using the measured δ^{18}O values of Los Colorados magnetite and actinolite separates (630°C) as well as Fe numbers of actinolite grains (610-820°C) are consistent with this interpretation. We also present Fe isotope data from magmatic magnetite of the Bushveld Complex, South Africa, where δ^{56}Fe ranges from 0.28 ± 0.04‰ to 0.86 ± 0.07‰. Based on these data and comparison to published Fe and O stable isotope values of igneous magnetite, we propose extending the magmatic/high-temperature δ^{56}Fe range to 0.86‰. Considering that the Chilean IOAs and Kiruna deposit are representative of IOA deposits worldwide, the Fe and O stable isotope data indicate that IOAs are formed by high-temperature (magmatic) processes.

3.1. INTRODUCTION

The 600 km-long Chilean iron belt (CIB) in Northern Chile (25-31°S) hosts numerous Mesozoic Fe-rich ore deposits, many of which are characterized as iron oxide–apatite (IOA) or iron oxide–copper–gold (IOCG) deposits (e.g., Nyström and Henriquez, 1994; Oyarzún et al., 2003; Groves et al., 2010). The origin and classification of these types of deposits is widely debated, and working hypotheses include: 1) meteoric fluids (e.g., basinal brines) and hydrothermal replacement (e.g., Barton and Johnson, 1996; Sillitoe and Burrows, 2002); 2) magmatic-hydrothermal fluids (e.g., Pollard, 2006; Richards and Mumin, 2013; Knipping et al., 2015); and 3) immiscible Fe-rich and Si-rich melts (Nyström and Henriquez, 1994; Naslund et al., 2002). A genetic connection between IOA and IOCG deposits has been proposed, wherein IOA deposits may represent the basal portion of IOCG systems (Sillitoe, 2003). Iron oxide–

apatite and IOCG deposits occur globally and individually host millions to billions of tons of their namesake metals and in some deposits economic reserves of uranium, rare earth elements (REEs), phosphorous, cobalt, silver, and/or titanium (Hitzman, 1992; Sillitoe, 2003; Groves et al., 2010; Richards and Mumin, 2013; Barton, 2014). Therefore, elucidating the source(s) of metals and the process(es) by which the deposits form is important for improving exploration strategies.

In this contribution, we pair non-traditional stable isotope data ($^{56}Fe/^{54}Fe$) with isotopic values from a stable isotope system ($^{18}O/^{16}O$) that has been well calibrated for deciphering the source of oxygen in rocks and minerals (Taylor, 1967; Hedenquist and Lowenstern, 1994; Bindeman, 2008) to fingerprint the source of Fe and O in magnetite in the world-class Los Colorados IOA deposit in Northern Chile. Los Colorados is one of the largest IOA deposits in the CIB and is representative of the nearly 50 IOAs in the region as well as those that exist globally. We also report Fe and O isotope ratio data for magnetite from several other deposits in the CIB, as well as the namesake Kiruna IOA deposit in Sweden. Magnetite can comprise >90 modal % of these deposits, and the Fe and O isotopic compositions of magnetite have been shown to be more resistant to secondary alteration than O and H isotopes in other mineral phases (Weis, 2013). Further, we use O isotope values of actinolite-magnetite pairs from unaltered Los Colorados samples to calculate minimum formation temperatures (cf. Bindeman, 2008), and use the Fe/Mg ratio of the actinolite grains to provide further constraints on the origin of actinolite.

3.2. GEOLOGICAL SETTING

The Cretaceous Los Colorados deposit has been characterized as an IOA or Kiruna-type ("magnetite-apatite") or simply "iron" deposit (e.g., Mathur et al., 2002; Oyarzún et al., 2003; Chen et al. 2013). It is the site of an active Fe mine ~35 km north of Vallenar, Chile within the

Atacama Fault System (AFS) (Figure 3.1) and contains ~350 Mt of Fe in two sub-parallel, sub-vertical magnetite-rich (up to >90 modal%) bodies that are hosted in the igneous rocks of the Punta del Cobre Formation (Pincheira et al., 1990; IAVCEI, 2004). The dikes measure approximately 1500 m long, ~150 m wide, ~500 m deep, and are oriented along strike of the southern portion of the AFS. The West and East dikes contain ~63% and ~55% total Fe, respectively, and are bounded on the west by a fault and the east by an Fe-rich brecciated zone (Fe_{total} = ~25%) that extends into dioritic wallrock. Microscopic observations of samples collected from Los Colorados drill cores and mine pit indicate a lack of sodic and potassic alteration (Knipping et al., 2015), which makes Los Colorados an ideal natural laboratory to investigate the source of metals in IOA systems.

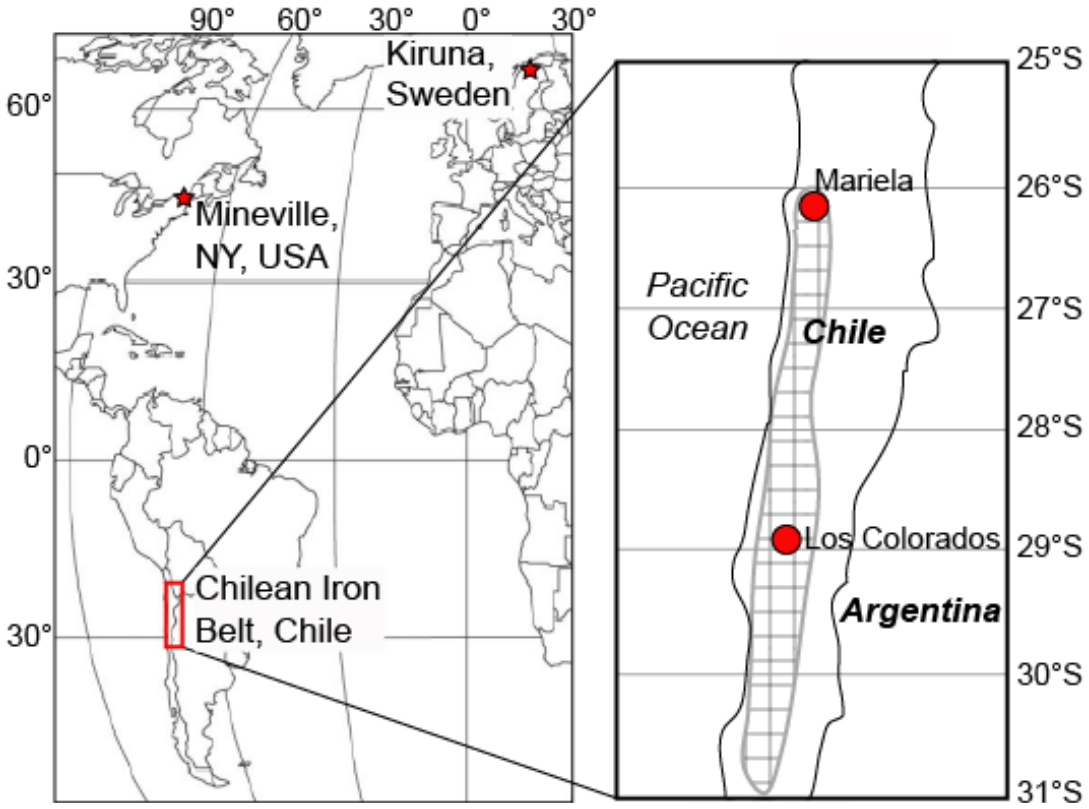

Figure 3.1: Map in left panel shows the locations of the three IOA districts focused on by this study. Right panel zooms into the Chilean iron belt (gray hatched area) and the iron oxide-apatite deposits analyzed here. The El Laco deposit is located northward of the belt.

3.3. SAMPLE PROCUREMENT AND PREPARATION

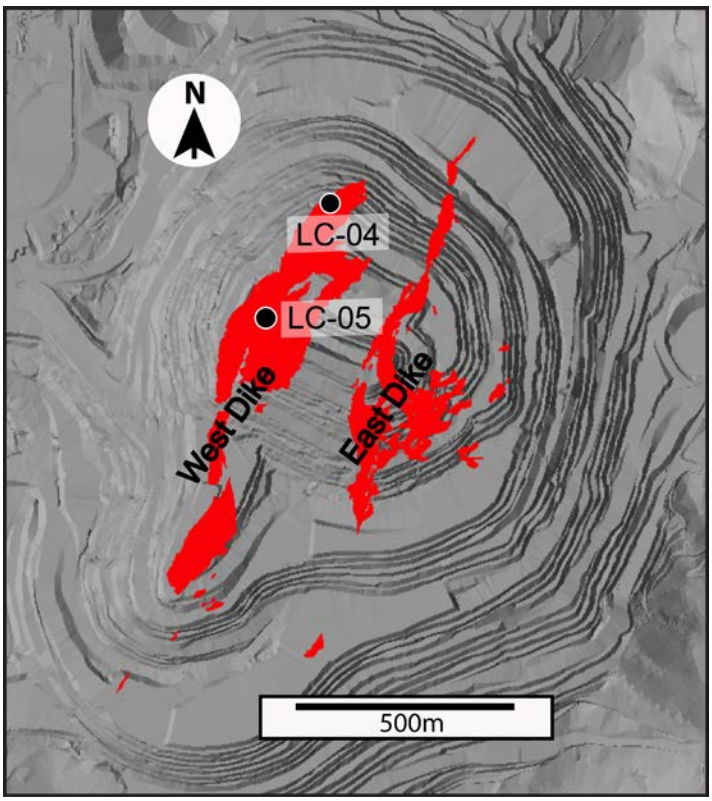

Figure 3.2: Map view of the West and East dikes (red areas) within the pit of the Los Colorados Iron Mine. Circles indicate surface locations of the two drill cores (LC-04 and LC-05) analyzed in this study.

Chilean Iron Belt Samples

Los Colorados drill core samples were acquired in cooperation with the Compañia Minera del Pacifico. We retrieved samples from two drill cores within the West Dike (Figure 3.2): 1) core LC-04, which penetrates the northern edge of the West Dike and extends into wall rock meta-andesite; 2) core LC-05, which was drilled through the middle portion of the West Dike and extends into a brecciated diorite at the base of the dike. Samples span the entire ~150 m length of each drill core. Additional samples were collected from the operating pit area, including one from the East Dike. We also collected samples from the smaller Mariela IOA deposit of the Atacama Region (Figure 3.1), and obtained samples from the Plio-Pleistocene El Laco “magnetite lavas”, which remains one of the most enigmatic Chilean IOA deposits and

whose genesis remains controversial (e.g., Henríquez and Nyström, 1998; Rhodes and Oreskes, 1999; Sillitoe and Burrows, 2002; Naranjo et al., 2010; Dare et al., 2014). The El Laco samples were collected from a drill core in the Pasos Blancos area, about 1 km south of Pico Laco (Naranjo et al., 2010).

Samples from Other Localities

We also analyzed magnetite samples from other well-studied IOA deposits (Table 3.1). These locations include the Kiruna IOA deposit in northern Sweden and the Mineville IOA deposit in New York, USA (Figure 3.1). Magnetite from the Granisle porphyry Cu deposit in British Columbia, CA (Quan et al., 1987), the Kuna Crest granodiorite of the Tuolumne Intrusive Series, USA (e.g., Paterson et al., 2008), and the Bushveld Igneous Complex (e.g., VanTongeren et al., 2010) were used as controls of magnetite of a known magmatic origin.

3.4. ANALYTICAL METHODS

Sample Selection and Preparation for Analysis

Whole rocks were hand-crushed by using an agate mortar and pestle that was rinsed in ethanol between samples to avoid contamination. Magnetite was separated from the crushed whole rock by using a hand magnet wrapped in a Kimwipe. Grains were then inspected under a microscope at ~40x magnification to ensure that no other mineral phases were present. Thin sections from corresponding samples were also inspected. For all isotopic measurements, only minerals without visible impurities were used. The magnetite was crushed after inspection to a powder with the agate pestle prior to laser fluorination for O isotope analysis and dissolution for Fe isotope analysis. Actinolite was handpicked under a binocular microscope before O isotope analysis to avoid grains with impurities.

Oxygen Isotopes

Oxygen isotope analyses were performed on mineral separates at the University of Oregon by using a laser fluorination line and Thermo-Finnigan MAT 253 gas isotope ratio mass spectrometer in dual inlet mode. About 2 mg of magnetite and 1.5 mg of actinolite were used for each analysis. Notably, although samples were carefully handpicked to avoid impurities, the Los Colorados magnetite contains sub-microscopic melt inclusions that cause them to behave unpredictably during interaction with the laser in the presence of BrF_5; crystals would move around and out of their places in the sample holder. Therefore, later analyses were performed on more finely powdered samples, exposing the entirety of the sample material to one power level before increasing the laser power in increments of one percent. A cold finger was used for any sample that yielded only 7.8 to 15 μmol total O (Table 3.1). Gore Mountain garnet was used as a standard and was analyzed before sample measurements began, in the middle of the sample queue, and once after all samples. Oxygen isotope values are reported in Table 3.1 relative to the international standard VSMOW, following equation 3.1:

$$\delta^{18}O_{sample}\ (‰) = [(^{18}O/^{16}O)_{measured} / (^{18}O/^{16}O)_{VSMOW} - 1] * 1000 \quad (3.1)$$

The average measured standard values ($\delta^{18}O_{GMGarnet}$ $\pm 1\sigma$) obtained during two days of instrument use were 6.90 ± 0.12‰ and 6.83 ± 0.10‰.

Iron Isotopes

Ion chromatography was performed on all samples to isolate Fe from whole rock or mineral samples for isotopic analysis. Magnetite samples were first dissolved and dried down in aqua regia, and then dissolved and dried down again in 8N HCl, before being loaded into columns with AG1-X8 resin in 8N HCl, following the procedure of Huang et al. (2011). Samples were analyzed by using a Nu Plasma HR multi-collector inductively coupled plasma mass

spectrometer (MC-ICP-MS) in dry plasma mode with a Desolvating Nebuliser System at the University of Illinois, Urbana-Champaign. All analyses were performed following the double-spike method of Millet et al. (2012), in which a standard solution of $^{57}Fe/^{58}Fe$ was added to each sample to correct for instrumental mass bias and increase precision. International standard IRMM-14 was measured between every sample to monitor and correct for instrumental drift throughout each session (Millet et al., 2012). Iron isotope data are reported in Table 3.1 relative to IRMM-14, following the relationship of equation 3.2:

$$\delta^{56}Fe_{sample}\ (‰) = [(^{56}Fe/^{54}Fe)_{measured} / (^{56}Fe/^{54}Fe)_{IRMM\text{-}14} - 1] * 1000 \quad (3.2)$$

Long-term reproducibility of BCR-2 was 0.07 ± 0.02‰ (1SE, n=14, 2 sessions over 3 months) and the average standard deviation of sample measurements (2σ) was 0.04‰.

Major Element Analyses of Actinolite Grains for Fe Number

Major element concentrations of actinolite were measured with Wavelength Dispersive Spectroscopy (WDS) by using a Cameca SX-100 electron probe microanalyzer (EPMA) at the University of Michigan, Ann Arbor, following the method of Lledo and Jenkins (2008). A 15nA beam was used with an accelerating voltage of 15 kV. We calibrated by using the following standards: ferrosillite (Fe), geikielite (Mg, Ti), tanzanite (Al), orthoclase (Si, K), wollastonite (Ca), rhodonite (Mn), and albite (Na). Sodium and Mg Kα were measured by using the LTAP crystal, TAP was used for Al and Si, PET was used for K and Ca, LPET for Ti, and the LLIF crystal was used to measure Mn and Fe.

3.5. RESULTS

Mineralogy of the Los Colorados Samples

The samples collected from Los Colorados are dominantly (up to 90 modal%) magnetite with an average of 5-10 modal% (combined) actinolite and apatite, and sparse (≤5 modal%)

quartz, clinopyroxene, orthopyroxene, titanite, and calcite. Crystals of quartz and calcite are interpreted to be secondary as they fill veins or cracks in the magnetite drill core samples. Actinolite occurs in some samples at up to 15 modal%, particularly in the pit sample collected from the East Dike. A representative backscatter electron image of actinolite within magnetite ore (sample 05-82.6) is shown in Figure 3.3. Stratigraphically, these modal abundances remain nearly constant for cores LC-04 and LC-05.

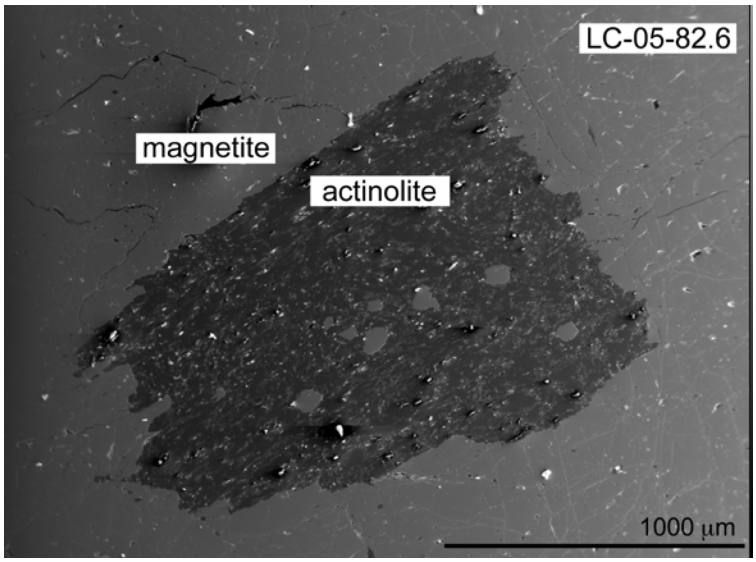

Figure 3.3: Backscatter electron image of a representative actinolite grain intergrown with magnetite from Los Colorados core LC-05, depth 82.6 m. The phase both surrounding and within the actinolite grain is magnetite.

Oxygen Isotope Compositions of Magnetite Separates

Stable O isotope values for magnetite separates are reported as $\delta^{18}O$ values in Table 3.1 and shown in Figure 3.4. The average value of $\delta^{18}O$ ($\pm 2\sigma$) of the Los Colorados magnetite sampled from cores LC-04 and LC-05 is 2.32 ± 0.12‰ (n=7) and 2.76 ± 0.12‰ (n=11), respectively (n refers to the number of unique samples from different depths of the core). The Kiruna sample has a $\delta^{18}O$ value of 1.76 ± 0.25‰ (n=2), and analyses of two El Laco magnetite samples yielded $\delta^{18}O$ values of 4.00 ± 0.10‰ (LCO-39) and 4.34 ± 0.10‰ (LCO vein) (Table 3.1). Magnetite from Mariela, yielded a $\delta^{18}O$ of 1.49 ±0.04‰, and magnetite from the Mineville

deposit yielded a $\delta^{18}O$ value of -0.79 ± 0.03‰. The $\delta^{18}O$ values presented here are consistent with the very limited published O isotope data for IOA and IOCG deposits (e.g., Rhodes and Oreskes, 1999; Nyström et al., 2008; Jonsson et al., 2013. Unequivocally magmatic-hydrothermal magnetite from the Granisle porphyry deposit and the igneous Kuna Crest granodiorite yielded $\delta^{18}O$ values of 2.70 ± 0.12‰ and 0.88 ± 0.12‰, respectively.

Iron Isotope Composition of Magnetite Separates

Stable Fe isotope data for magnetite separates are reported in Table 3.1 and Figure 3.4. Los Colorados core LC-04 magnetite $\delta^{56}Fe$ (± 2σ) values range from 0.18 ± 0.03‰ to 0.26 ± 0.04‰ ($\delta^{56}Fe_{average}$ = 0.20‰; n=8) and core LC-05 magnetite $\delta^{56}Fe$ values range from 0.08 ± 0.08‰ to 0.22 ± 0.05‰ ($\delta^{56}Fe_{average}$ = 0.15‰; n=9). Magnetite from pit samples of the East Dike yielded a $\delta^{56}Fe$ of 0.24 ± 0.02‰. The data for samples from both of the Los Colorados West Dike drill cores are stratigraphically homogeneous within the ore bodies within the drill core (Figure 3.4).

The $\delta^{56}Fe$ composition of magnetite from the Mariela IOA deposits is 0.13 ± 0.03‰ and 0.57 ± 0.04‰, respectively. Magnetite from El Laco ranges from $\delta^{56}Fe$ = 0.20 ± 0.03‰ to 0.53 ± 0.03‰ ($\delta^{56}Fe_{average}$ = 0.33‰; n=7). Mineville magnetite yielded a $\delta^{56}Fe$ value of -0.92 ± 0.03‰. Kiruna magnetite has a $\delta^{56}Fe$ of 0.16 ± 0.07‰. Magnetite Fe isotope compositions have also been measured in samples of the Upper and Upper Main Zone of the Bushveld Complex, South Africa, previously characterized by VanTongeren et al. (2010) and VanTongeren and Mathez (2012) (Bilenker et al., 2014). The $\delta^{56}Fe$ values obtained from these samples range from 0.28 ± 0.04‰ to 0.86 ± 0.07‰.

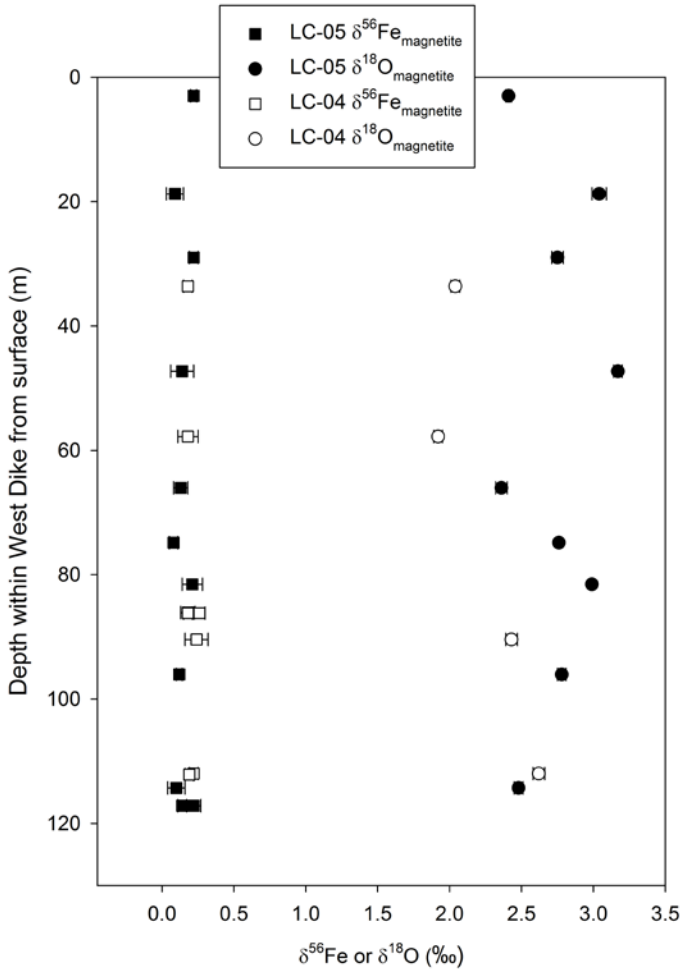

Figure 3.4: All Los Colorados stable Fe and O isotope data plotted for both core 05 and 04 within the West Dike. The drill cores were not vertical. True depth from Earth's surface was calculated for each sample according to the dip and length of each drill core (data provided by Compañia Minera del Pacifico). Error bars for all data are 2σ.

Oxygen Isotope Composition and Fe Number of Actinolite

Actinolite from Los Colorados sample 05-72.9 yielded a $\delta^{18}O$ value of 6.46 ± 0.56‰. The Fe number (Fe # = [molar Fe] / [molar Fe + molar Mg]) of actinolite was calculated for individual actinolite grains sampled from core LC-05 (depth = 82.6 m; sample name 05-82.6), one pit sample from the West Dike (pitW3), and one pit sample from the East Dike (pitE1). The average Fe # (± 1σ) for all grains measured in each of these samples is 0.44 ± 0.11, 0.35 ± 0.05, and 0.52 ± 0.02, respectively. All analytical data for actinolite are reported in Table 3.2.

3.6. DISCUSSION

Constraints on the source of Fe and O in IOA deposits

Traditionally, O and H stable isotope ratios have been used to establish "boxes", or ranges, of the isotopic composition of rocks and minerals formed from specific processes, such as precipitation from a meteoric fluid versus precipitation from a magmatic-hydrothermal fluid exsolved directly from a silicate melt (Hedenquist and Lowenstern, 1994). However, since Fe-rich ore deposits such as IOAs lack abundant H-bearing phases, or only contain H-bearing minerals that are paragenetically post-mineralization, developing source ranges for stable Fe—O isotope pairs offers the opportunity to fingerprint directly the source of Fe and O in IOAs.

The global range of O isotope values for igneous magnetite (i.e., magnetite crystallized directly from silicate melt) was constrained by Taylor (1967, 1968) as $\delta^{18}O$ = 1.0 to 4.4‰. Similarly, for stable Fe isotopes, Heimann et al. (2008) and Weis (2013) reported a global range for igneous magnetite of $\delta^{56}Fe$ = 0.06 to 0.49‰. In these studies, igneous magnetite was sampled from plutonic and volcanic rocks, and the values represent those of unaltered, primary igneous magnetite.

The method of using Fe and O isotope ratios for source fingerprinting was first employed successfully on IOA samples by Weis (2013) who focused on the >1.85 Ga Grängesberg Mining District (GMD), Sweden. Iron isotope data are useful because Fe is abundant in the deposit, exists within the mineral of economic interest, and the Fe isotope compositions of minerals appear to be less affected by secondary processes than other isotopic systems. Weis (2013) demonstrated this by quantifying the Fe and O isotope values of magnetite grains within and around the GMD ore deposit as well as samples from other Fe-rich deposits of known igneous origin (e.g., basalt, basaltic andesite, dacite, dolerite). The Fe isotope data showed less variation

and plotted within the known igneous range (cf. Heimann et al., 2008), while the O isotope compositions of some of the magnetite samples plot outside of the range interpreted to represent igneous O isotope values (c.f. Taylor, 1967; 1968) (Figure 3.5, gray triangles).

All published Fe—O isotope pairs (Weis, 2013; this study) are plotted in Figure 3.5 along with the accepted bounds of the magmatic Fe—O isotope box. The Los Colorados and other CIB samples (El Laco, Mariela) plot distinctively within the range of magmatic values along with Kiruna magnetite, suggesting a high-temperature origin for these IOA deposits. Since the few available Fe—O isotope pairs are not limited to Chilean and Swedish IOA deposits, we can begin to identify areas beyond the magmatic box where samples formed due to other processes. However, additional data are needed to refine these other potential boxes. For example, Mineville magnetite has particularly low δ^{56}Fe and δ^{18}O compositions. By combining field relations, geochronology, and geochemical compositions of host, mineralized, and later-emplaced rocks, Valley et al. (2011) concluded that secondary fluids remobilized magmatic magnetite to form new Fe oxide deposits at Mineville. Since it has been shown by theoretical calculations and experimental data that Cl-bearing fluids preferentially incorporate ^{54}Fe relative to magnetite (e.g., Heimann et al., 2008; Hill and Schauble, 2008; Bilenker et al., 2013), our Fe—O isotope data agree with the hypothesis of Valley et al. (2011). The other samples with lighter Fe—O isotope compositions are from the Dannemora Iron Skarn deposit, Sweden (Weis, 2013; Figure 3.5, white circles). This skarn was formed by contact metamorphism when a magma intruded carbonate wall rock. The Fe—O isotope data are close to but outside of the

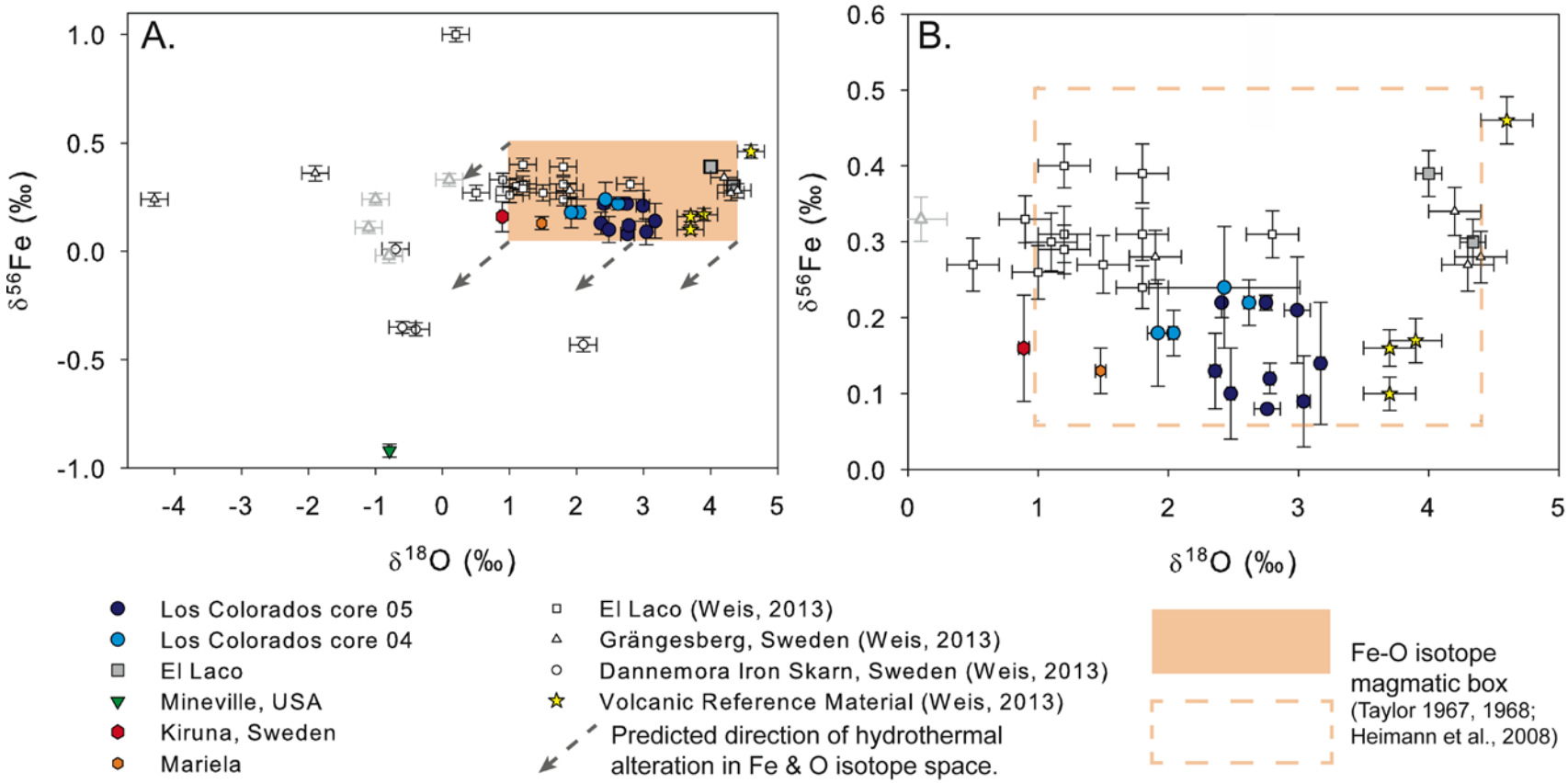

Figure 3.5. Isotopic data for magnetite samples in δ^{56}Fe vs. δ^{18}O space. Colored symbols represent samples measured in this study, and open symbols represent data reported by Weis (2013). The solid and dashed orange boxes denote magmatic isotope ranges as established by Taylor (1967, 1968) and Heimann et al. (2008). Yellow stars denote Fe and O isotope values for igneous magnetite reported by Weis (2013). The Grängesberg samples denoted by gray triangles represent the altered samples reported in Weis (2013). Panel A displays all data discussed while panel B show only datasets that include samples plotting within the magmatic Fe—O box. All Los Colorados samples have magmatic Fe—O isotope values. Error bars are 2σ.

magmatic ranges, consistent with the interaction of magmatic fluids and sedimentary rocks that formed from isotopically lighter, low-temperature fluids.

Our El Laco data are consistent with the previously published values of $\delta^{18}O$ reported by Rhodes and Oreskes (1999) and Nyström et al. (2008). However, while the magnetite data reported by Rhodes and Oreskes (1999) fit within the range for igneous magnetite, they were interpreted by the authors of that study to indicate precipitation of magnetite from isotopically heavy non-magmatic fluids, hypothesized to have been derived from interaction with an evaporitic source. These conclusions were based upon the fact that "hydrothermal" and "magmatic" magnetite at El Laco have similar O isotope values. Nyström et al. (2008) used their O isotope data to complement field observations and fluid inclusion data and concluded that the El Laco magnetite has a magmatic origin with minimal secondary alteration. Since we now also have constraints for magmatic Fe isotopes, our Fe—O isotope pairs are consistent with the latter hypothesis and seem to demand a magmatic or magmatic-hydrothermal formation for El Laco.Importantly, the Fe isotope data obtained from the Bushveld provide another source of unequivocally magmatic magnetite, and plot within and above the $\delta^{56}Fe$ range as determined by Heimann et al. (2008) and Weis (2013). Therefore, we can use these new data to extend the $\delta^{56}Fe$ range of the magmatic magnetite Fe—O box to 0.06 to 0.86‰ (Figure 3.6).

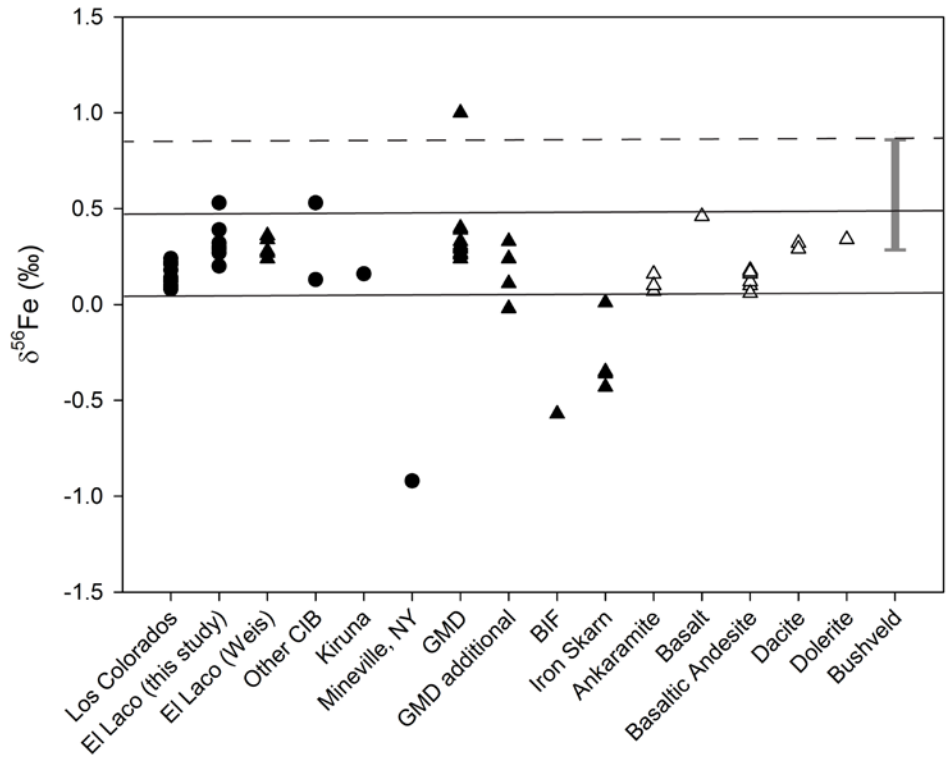

Figure 3.6: Iron isotope composition of magnetite samples measured in this study (circles) and data reported in Weis (2013) (triangles). The open triangles highlight data for unaltered igneous magnetite ("Volcanic Reference Material"). The vertical gray bar for the Bushveld represents the range of δ^{56}Fe values obtained from magnetite separates. Solid horizontal lines indicate the upper and lower δ^{56}Fe values reported by Heimann et al. (2008) for magnetite from unaltered volcanic and plutonic rocks. The horizontal dashed line is the upper δ^{56}Fe values when igneous magnetite from the Bushveld intrusion is included.

Constraints on the Minimum Formation Temperature of Los Colorados

Isotopic Constraints

We calculated minimum formation temperatures by using the difference in O isotope composition between magnetite and actinolite (cf. Bindeman and Valley, 2002):

$$\Delta^{18}O_{actinolite\text{-}magnetite} = \delta^{18}O_{actinolite} - \delta^{18}O_{magnetite} \sim 1000\ln\alpha \qquad (3.3)$$

The $\Delta^{18}O_{actinolite\text{-}magnetite}$ of the actinolite-magnetite pair analyzed from sample 05-72.9 is 4.10‰ ($\delta^{18}O_{actinolite}$ - $\delta^{18}O_{magnetite}$ = 6.46‰ - 2.36‰). By using the measured $\Delta^{18}O_{actinolite\text{-}magnetite}$, the minimum formation temperature can be calculated via equation 3.4:

$$1000\ln\alpha = 10^6 A/T^2 \qquad (3.4)$$

where A is the experimentally-determined A factor for the linear relationship between O isotope fractionation between magnetite and amphibole and $10^6/T^2$ through 0 (A = 3.36 here); T is temperature in Kelvin (Bindeman, 2008). The calculated minimum temperature of formation is ~630°C, consistent with the closure temperature of magmatic magnetite for O isotopes.

We also used published fractionation factors to calculate the isotopic composition of the parent magma and magmatic water that may have formed Los Colorados: $\Delta^{18}O_{magnetite\text{-}andesite}$ = -4.0‰, $\Delta^{18}O_{magnetite\text{-}water}$ = -4.5‰ (Zhao and Zheng, 2003). Using equation 3.3 and the average $\delta^{18}O$ of Los Colorados magnetite (2.60 ± 0.74‰), the isotopic compositions of the parent magma and co-existing magmatic water are calculated to be 6.60‰ and 7.10‰, respectively. This is consistent with the O isotope composition of subduction zone magmas, like the ones associated with the formation of IOA deposits (Taylor, 1968; Bindeman, 2008; Jonsson et al., 2013).

Geochemical constraints

The Fe # calculated for actinolite from the Los Colorados deposit are consistent with high-temperature growth of actinolite (Table 3.2). We compared these Fe # values to the experimental data of Lledo and Jenkins (2008) to obtain a reasonable estimation of the formation temperature. The average Fe # of 0.44 for all Los Colorados actinolite samples yields calculated formation temperatures that range from 620-790°C and 640-820°C at 100 and 200 MPa, respectively. Applying the highest (Fe # = 0.72) and lowest (Fe # = 0.25) Fe # to the temperature ranges corresponding with pressures of 100 and 200 MPa yields a minimum temperature of 610°C and a maximum temperature of 820°C. These temperatures are consistent with the closure temperatures calculated from actinolite-magnetite O isotope values.

Implications for the Formation of Iron Oxide-Apatite Deposits

The Fe and O stable isotope and actinolite Fe # data reported here demonstrate that both Fe and O in magnetite from the Chilean Fe oxide deposits (Los Colorados, El Laco, Mariela) and the Kiruna IOA deposit were sourced from a magmatic reservoir (Figure 3.5). We invoke high-temperature processes to form IOA deposits, but as of yet, these geochemical methods alone do not allow for us to rule out specific magmatic/magmatic-hydrothermal processes. However, further development of this method by using additional geochemical data to study a wide variety of global samples will allow it to become a robust, independent geochemical tool.

3.7. CONCLUSIONS

We report stable Fe and O isotope ratios for magnetite from several iron oxide – apatite (IOA) ore deposits, and combine these data with Fe and O isotope ratios from unequivocally magmatic and magmatic-hydrothermal magnetite to elucidate the source reservoir for these elements in IOA deposits. The $\delta^{18}O$ and $\delta^{56}Fe$ values for all samples cluster in the ranges 1.0 to 4.4‰ and 0.06 to 0.86‰, respectively. These Fe and O isotope data demonstrate that Fe and O in magnetite in IOA deposits are sourced from a magmatic reservoir. Pairing stable Fe and O isotope data from magnetite is a promising new method for fingerprinting the source of these elements in magnetite-bearing ore deposits. Further, we combine Fe and O isotope ratio data for magnetite and actinolite as well as the Fe # of actinolite grains from the world-class Los Colorados IOA deposit, Chile, to conclude that this deposit formed by high-temperature processes. At present, Fe and O isotope pairs do not allow us to discriminate whether magnetite crystallized from a melt or precipitated from a high-temperature magmatic-hydrothermal fluid, but future refinement of the Fe—O isotope source boxes may eventually allow this distinction.

3.8. REFERENCES

Barton M.D. and Johnson D.A. (1996) Evaporitic-source model for igneous-related Fe oxide-(REE-Cu-Au-U) mineralization. *Geology* **24**, 259-262.

Barton M.D. (2014) Iron Oxide(-Cu-Au-REE-P-Ag-U-Co) Systems. In: *Treatise on Geochemistry*, 2nd edition, vol. 11, p. 515-541.

Bilenker L.D., Simon A., Lundstrom C.C., Gajos N. and Zajacz Z. (2013) Experimental constraints on Fe isotope fractionation in fluid-melt-oxide-sulfide assemblages. *Goldschmidt Conference*.

Bilenker L.D., VanTongeren J.A., Lundstrom C. and Simon A. (2014) Fe isotope systematics of the Upper and Upper Main Zones of the Bushveld Complex, South Africa. *AGU Fall Meeting* [abs]: V51C-4797.

Bindeman I. (2008) Oxygen Isotopes in Mantle and Crustal Magmas as Revealed by Single Crystal Analysis. *RiMG* **69**, 445-478.

Chen H., Clark A.H., Kyser T.K., Ullrich T.D., Baxter R., Chen Y. and Moody T.C. (2010) Evolution of the Giant Marcona-Mina Justa Iron Oxide-Copper-Gold District, South-Central Peru. *Econ. Geol.* **105**, 155-185.

Chen H., Cooke D.R. and Baker M.J. (2013) Mesozoic Iron Oxide Copper-Gold Mineralization in the Central Andes and the Gondwana Supercontinent Breakup. *Econ. Geol.* **108**, 37-44.

Dare S.A.S., Barnes S.-J. and Beaudoin G. (2014) Did the massive magnetite "lava flows" of El Laco (Chile) form by magmatic or hydrothermal processes? New constraints from magnetite composition by LA-ICP-MS. *Mineral. Dep.* DOI:10.1007/s00126-014-0560-1.

Groves D.I., Bierlein F.P., Meinert L.D. and Hitzman M.W. (2010) Iron Oxide Copper-Gold (IOCG) Deposits through Earth History: Implications for Origin, Lithospheric Setting, and Distinction from Other Epigenetic Iron Oxide Deposits. *Econ. Geol.* **105**, 641-654.

Hill P.S. and Schauble E.A. (2008) Modeling the effects of bond environment on equilibrium iron isotope fractionation in ferric aquo-chloro complexes. *Geochim. Cosmochim. Acta* **72**, 1938-1958.

Hedenquist J.W. and Lowenstern J.B. (1994) The role of magmas in the formation of hydrothermal ore deposits. *Nature* **370**, 519-527.

Heimann A., Beard B.L. and Johnson C.M. (2008) The role of volatile exsolution and sub-solidus fluid/rock interactions in producing high $^{56}Fe/^{54}Fe$ ratios in siliceous igneous rocks. *Geochim. Cosmochim. Acta* **72**, 4379-4396.

Henríquez, F., and Nyström, J.O. (1998) Magnetite bombs at El Laco volcano, Chile. *GFF* **120**, 269-271.

Huang F., Zhang Z., Lundstrom C.C. and Zhi X. (2011) Iron and magnesium isotopic compositions of periodotite xenoliths from Eastern China. *Geochim. Cosmochim. Acta* **75**, 3318-3334.

Knipping J.L., Bilenker L.D., Simon A.C., Reich M., Barra F., Deditius A.P., Lundstrom C., Bindeman I. and Munizaga R. (2015) Giant Kiruna-type deposits form by efficient floation of magmatic magnetite suspensions. *Geology*, published online 19 May 2014, doi:10.1130/G36650.1.

Lledo H.L. and Jenkins D.M. (2008) Experimental Investigation of the Upper Thermal Stability of Mg-rich Actinolite Implications for Kiruna-Type Iron Deposits. *Journal of Petrol.* **49**, 225-238.

Mathur R., Marschik R., Ruiz J., Munizaga F., Leveille R.A. and Martin W. (2002) Age of Mineralization of the Candelaria Fe Oxide Cu-Au Deposit and the Origin of the Chilean Iron Blet, Based on Re-Os Isotopes. *Econ. Geol.* **97**, 59-71.

Millet M-A., Baker J.A. and Payne C.E. (2012) Ultra-precise stable Fe isotope measurements by high resolution multiple-collector inductively coupled plasma mass spectrometry with a ^{57}Fe-^{58}Fe double spike. *Chem. Geol.* **304-305**, 18-25.

Naranjo J.A., Henriquez F. and Nyström J.O. (2010) Subvolcanic contact metasomatism at El Laco Volcanic Complex, Central Andes. *Andean Geol.* **37**, 110-120.

Nyström J.O. and Henriquez F. (1994) Magmatic Features of Iron Ores of the Kiruna Type in Chile and Sweden: Ore Textures and Magnetite Geochemistry. *Econ. Geol.* **89**, 820-839.

Nyström J.O., Billström K., Henríquez F., Fallick A.E. and Naslund H.R. (2008) Oxygen isotope composition of magnetite in iron ores of the Kiruna type in Chile and Sweden. *GFF* **130**, 177-188.

Oyarzun R., Oyarún J., Meénard J.J. and Lillo J. (2003) The Cretaceous iron belt of northern Chile: role of oceanic plates, a superplume event, and a major shear zone. *Mineral. Dep.* **38**, 640-646.

Paterson S.R., Žák J. and Janoušek V. (2008) Growth of complex sheeted zones during recycling of older magmatic units into younger: Sawmill Canyon area, Tuolumne batholith, Sierra Nevada, California. *Jour. Volc. Geotherm. Res.* **177**, 457-484.

Pincheira M.J., Theile R. and Fontbote L. (1990) Tectonic transpression along the southern segment of the Atacama Fault-Zone, Chile. In: Colloques et Seminaires: Symposium International de Geodynamique Andine, Grenoble, 133-136.

Pollard P.J. (2006) An intrusion-related origin for Cu-Au mineralization in iron oxide-copper-gold (IOCG) provinces. *Min. Dep.* **41**, 179-187.

Quan R.A., Cloke P.L. and Kesler S.E. (1987) Chemical analyses of halite trend inclusions from the Granisle porphyry copper deposit, British Columbia. *Econ. Geol.* **82**, 1912-1930.

Rhodes, A.L. and Oreskes, N. (1999) Oxygen isotope composition of magnetite deposits at El Laco, Chile: Evidence of formation from isotopically heavy fluids. In: *Geology and ore deposits of the Central Andes,* B.J. Skinner, ed., SEG Special Publication **7**, 333-351.

Richards J.P. and Mumin A.H. (2013) Magmatic-hydrothermal processes within an evolving Earth: Iron oxide-copper-gold and porphyry Cu ± Mo ± Au deposits. *Geology*, published online as doi: 10.1130/G34275.1.

Sillitoe, R.H., and Burrows, D.R. (2002) New field evidence bearing on the origin of the El Laco magnetite deposit, Northern Chile. *Econ. Geol.* **97**, 1101-1109.

Sillitoe R.H. (2003) Iron oxide-copper-gold deposits: an Andean view. *Mineral. Dep.* **38**, 787-821.

Simon A., Pettke T., Candela P.A., Piccoli P.M. and Heinrich C.A. (2004) Magnetite solubility and iron transport in magmatic-hydrothermal environments. *Geochim. et Cosmochim. Acta* **68**, 4905-4914.

Taylor H.P. (1979). Oxygen and hydrogen isotope relationships in hydrothermal mineral deposits, pp. 236-277 in: H.L. Barnes, Ed., *Geochemistry of Hydrothermal Ore Deposits*, 2nd ed. New York: Wiley, 798 pp.

VanTongeren J.A., Mathez E.A. and Kelemen P.B. (2010) A Felsic End to Bushveld Differentiation. *J. Petrol.* **51**, 1891-1942.

VanTongeren J.A. and Mathez E.A. (2012) Large-scale liquid immiscibility at the top of the Bushveld Complex. *Geology* **40**, 491-494.

Weis F. (2013). Oxygen and Iron Isotope Systematics of the Grängesberg Mining District (GMD), Central Sweden. Diss. Uppsala universitet.

TABLES

Table 3.1: Fe and O isotope data for oxides and actinolite mineral separates. NA indicates that samples were not analyzed for that isotope pair. Sample refers to the drill core (e.g., LC-05 or LC-04) and depth within the core where the sample was taken; e.g., 05-3.30 indicates core 05 and 3.30 meters from the top of the drill hole. Note that depths in this table differ from those presented in Figure 3.2 where the depths correspond to true depth from Earth's surface.

Location	Sample	Phase	δ^{56}Fe (‰)	2σ	δ^{18}O (‰)	2σ
Chilean Iron Belt						
Los Colorados (LC)						
Core LC-05	05-3.30	Magnetite	0.22	0.03	2.41	0.02
	05-20.7	Magnetite	0.09	0.06	3.04	0.05
	05-32	Magnetite	0.22	0.03	2.75	0.04
	05-52.2	Magnetite	0.14	0.08	3.17	0.03
	05-72.9	Magnetite	0.13	0.05	2.36	0.04
		Actinolite 1	NA	NA	6.18	0.12
		Actinolite 2	NA	NA	6.74	0.12
	05-82.6	Magnetite	0.08	0.03	2.76*	0.10
	05-90	Magnetite	0.21	0.07	2.99	0.10
	05-106	Magnetite	0.12	0.03	2.78	0.03
	05-126.15	Magnetite	0.10	0.06	2.48	0.03
	05-129.3a	Magnetite	0.22	0.05	NA	NA
	05-129.3b	Magnetite	0.14	0.02	NA	NA
Core LC-04	04-38.8	Magnetite	0.18	0.03	2.04	0.03
	04-66.7	Magnetite	0.18	0.07	1.92*	0.08
	04-129.3	Magnetite	0.22	0.03	2.62*	0.04
	04-104.4	Magnetite	0.24	0.08	2.43*	0.58
LC East Dike	pitE1	Magnetite	0.18	0.03	NA	NA
El Laco	LCO-39	Magnetite	0.39	0.09	4.00	0.10
	LCO	Magnetite	0.29	0.03	NA	NA
	LCO vein	Magnetite	0.30	0.03	4.34	0.10
	LCO-76	Magnetite	0.32	0.09	NA	NA
	LCO-78	Magnetite	0.53	0.03	NA	NA
	LCO-104	Magnetite	0.27	0.03	NA	NA
	LCO-111	Magnetite	0.20	0.03	NA	NA
Mariela	M-8	Magnetite	0.13	0.03	1.49	0.04
Other IOAs						
Mineville, NY	Mineville	Magnetite	-0.92	0.03	-0.79	0.03
Kiruna, Sweden	KRA-9	Magnetite	0.16	0.07	1.76	0.25
Other Igneous						
Tuolumne Intrusive Series	TIS	Magnetite	NA	NA	0.88*	0.12
Granisle Porphyry	GR-1	Magnetite	NA	NA	2.70*	0.12

*Samples required a cold finger for O isotope analysis because they yielded between 7.8 and 15 μmol□

Table 3.2: Fe and Mg molar concentrations and calculated Fe # of actinolite grains within the Los Colorados magnetite dikes. Grain compositions were obtained by point or line traverse EPMA measurements; averages of the values of the latter were used for the grains denoted with an asterisk.

location	grain ID	Mg (molar)	Fe (molar)	Fe # (grain average)
pit west	1	3.36	1.98	0.37
pit west	2	3.34	2.02	0.38
pit west	3*	3.33	2.13	0.39
pit west	4	3.39	1.58	0.32
pit west	5	3.41	1.66	0.33
pit west	6	3.33	1.84	0.36
pit west	7	3.26	2.40	0.42
pit west	8*	3.32	2.18	0.40
pit west	9	3.44	1.66	0.32
pit west	10	3.12	2.42	0.44
pit west	11	3.25	1.65	0.34
pit west	12	3.39	1.61	0.32
pit west	13*	3.34	2.06	0.38
pit west	14*	3.32	2.15	0.39
pit west	15	3.63	1.10	0.23
pit west	16	3.61	1.17	0.25
	Average			0.35
pit east	1*	2.92	3.41	0.54
pit east	2*	2.94	3.33	0.53
pit east	3*	2.80	3.33	0.54
pit east	4	2.89	3.24	0.53
pit east	5	2.87	3.32	0.54
pit east	6	2.96	3.42	0.54
pit east	7	3.03	3.03	0.50
pit east	8	3.08	2.86	0.48
	Average			0.52
core 5 82.6	1	3.25	2.09	0.38
core 5 82.6	2	1.99	5.14	0.72
core 5 82.6	3	3.32	1.95	0.37
core 5 82.6	4	3.40	2.66	0.38
core 5 82.6	5*	3.34	1.60	0.40
core 5 82.6	6*	3.10	2.44	0.43
core 5 82.6	7	3.18	2.66	0.46
core 5 82.6	8	3.24	2.22	0.41
	Average			0.44
Los Colorados	Average			0.44
	2σ			0.28

CHAPTER IV

Fe ISOTOPIC EVOLUTION DURING FRACTIONAL CRYSTALLIZATION OF THE UPPERMOST BUSHVELD COMPLEX LAYERED MAFIC INTRUSION

ABSTRACT

We present the first data for the evolution of $\delta^{56}Fe$ ($^{56}Fe/^{54}Fe$ relative to standard IRMM-14) recorded in whole rock and magnetite mineral separates from the Upper and Upper Main Zones (UUMZ) of the Bushveld Complex layered series. The UUMZ evolved by fractional crystallization of a dry tholeiitic magma to produce gabbros and diorites with cumulus magnetite and fayalitic olivine. Despite previous work indicating a potential for magnetite crystallization to drastically change magma $\delta^{56}Fe$ during fractional crystallization, we observe no change in whole rock $\delta^{56}Fe$ above and below magnetite saturation. We also observe no change in whole rock $\delta^{56}Fe$ with increasing stratigraphic height, and only a small variation in $\delta^{56}Fe$ in magnetite mineral separates. Whole rock $\delta^{56}Fe$ ($\pm 2\sigma$) throughout the UUMZ ranges from -0.15 ±0.07‰ to 0.21 ±0.09‰ ($\delta^{56}Fe_{averageWR}$ = 0.09 ±0.08‰; n=22), and magnetites range from 0.28 ±0.04‰ to 0.86 ±0.07‰ ($\delta^{56}Fe_{averageMgt}$ = 0.50 ±0.15‰; n=20), similar to values previously reported from the Skaergaard Intrusion, Sonju Lake Intrusion, and Baima Intrusion. Our results are consistent with a model of $\delta^{56}Fe$ evolution during fractional crystallization of mafic cumulate rocks, which takes into account the modal abundances and fractionation factors for $\delta^{56}Fe$ of all phases present in the cumulate assemblage. This is the first study to evaluate the evolution of Fe isotopes in cumulate rocks formed from a nominally anhydrous tholeiitic basalt and indicates that the $\delta^{56}Fe$

signatures of the Bushveld are controlled by fractional crystallization and sub-solidus re-equilibration.

4.1. INTRODUCTION

Significant variations of stable Fe isotope ratios are predicted to occur under magmatic-hydrothermal conditions (i.e., high T, P). Proposed magmatic processes leading to isotopic fractionation include fractional crystallization (e.g., Schuessler et al., 2007; Shahar et al., 2008; Schuessler et al., 2009; Teng et al., 2008), fluid exsolution (Poitrasson and Freydier, 2005; Heimann et al., 2008; Telus et al., 2012), evolution of oxygen fugacity (fO_2) (Williams et al., 2005; Sossi et al., 2012, Foden et al., 2014), bonding environment (e.g., Schauble et al., 2004; Dauphas et al., 2014) and thermal gradients (Lundstrom et al., 2009; Huang et al., 2010; Zambardi et al., 2014). However, the mechanisms that control Fe isotope fractionation are still being actively investigated (e.g., Young et al., 2015). Despite these important studies, to-date there is no systematic study looking at the evolution of Fe isotopes in cumulate rocks formed by fractional crystallization from a single large magma body. The well-characterized Rustenberg Layered Suite (RLS) of the Bushveld Complex magmatic province is an ideal location in which to investigate the evolution of Fe isotopes in cumulate rocks during fractional crystallization.

The uppermost ~2.5 km of the 8-9 km thick RLS intrusion are represented by the Upper and Upper Main Zones (UUMZ). On the basis of major element, trace element, and isotopic geochemical trends, the rocks of the UUMZ are thought to reflect the crystallization products from the final pulse of magma into the chamber (e.g., Kruger et al., 1987; VanTongeren et al., 2010; VanTongeren and Mathez, 2013). Above a 3 m thick orthopyroxenite layer, the Pyroxenite Marker, the UUMZ is characterized by an evolving phase assemblage of pyroxene (px) + plagioclase (plag) → px + plag + magnetite (mgt) → px + plag + mgt + olivine (ol) → px + plag

+ mgt + ol + apatite (ap). VanTongeren et al. (2010) showed that the cumulus mineral compositions and phase assemblages in the UUMZ evolved by fractional crystallization from a single parent magma composition from the Pyroxenite Marker all the way to the roof of the intrusion.

We report the first Fe isotope ratio data on whole rocks and magnetite mineral separates throughout the stratigraphy of the UUMZ in the eastern Bushveld to investigate the effect of magmatic differentiation of a nominally anhydrous tholeiitic basalt on the isotopic evolution of the magma.

4.2. METHODS AND RESULTS

Samples were collected from exposed sections of the eastern limb of the RLS, and are the same as those analyzed in the studies of VanTongeren et al. (2010) and VanTongeren and Mathez (2012). Stratigraphic heights are reported relative to the Merensky Reef (MR) in the eastern Bushveld; the Pyroxenite Marker is located at 2200 m above the MR, and the roof of the intrusion is at 4625 m. Stable Fe isotope analyses were performed on whole rock and magnetite samples from the same stratigraphic position by using a Nu Plasma HR multi-collector inductively coupled mass spectrometer. We employed the ^{57}Fe-^{58}Fe double-spike method of Millet et al. (2012) for maximum precision and to correct for instrumental mass bias.

Results are reported in Table A.1 as $\delta^{56}Fe$ ($\pm 2\sigma$) relative to the international Fe isotope standard, IRMM-14, following equation 4.1: $\delta^{56}Fe$ (‰) = [($^{56}Fe/^{54}Fe_{sample}$ - $^{56}Fe/^{54}Fe_{IRMM\text{-}14}$) / $^{56}Fe/^{54}Fe_{IRMM\text{-}14}$] * 1000. Our dataset contains 22 whole rock ($\delta^{56}Fe_{WR}$) analyses plus 20 magnetite analyses ($\delta^{56}Fe_{mgt}$), including 20 whole rock-magnetite pairs for various stratigraphic heights throughout the UUMZ. Precision is estimated at 0.03‰ or is given based on the 2SD of repeat analysis. Values for BCR-2 processed identically are 0.62 ±0.03‰.

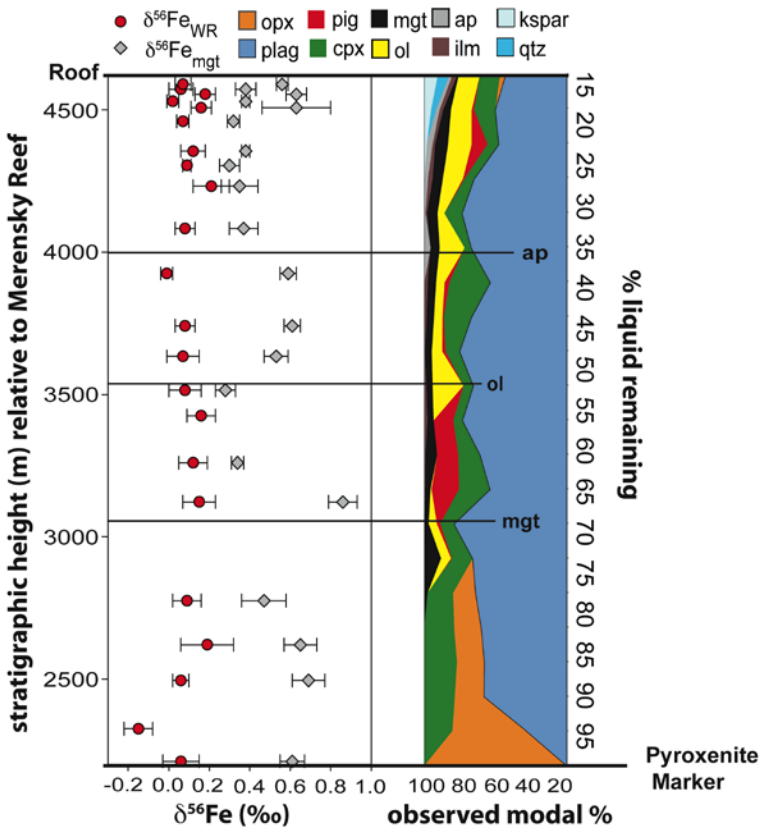

Figure 4.1: Measured Fe isotope compositions of whole rock (red circles) and magnetite (gray diamonds) plotted at the stratigraphic depth from which the samples were obtained, relative to the Merensky Reef. These data are compared to the observed modal abundances of phases from the base of the UUMZ (Pyroxenite Marker at 2200m) to the roof (4625m) (VanTongeren et al., 2010). Error bars are 2σ. Ap—apatite saturation; ol—olivine saturation; mgt—magnetite saturation.

We observe no systematic change in $\delta^{56}Fe_{WR}$ values with stratigraphic height within the UUMZ and there are few correlations between $\delta^{56}Fe_{WR}$ values and bulk rock or individual mineral geochemistry. $\delta^{56}Fe_{WR}$ ranges from -0.15 ±0.07‰ to 0.21 ±0.09‰ ($\delta^{56}Fe_{WR}$ average ~0.09 ±0.08‰) (Figure 4.1). Whole rock values reflect the weighting of the mineral mode and the isotope ratio of the phase; modes are not constant in layered rocks such as those measured here. The isotopically lightest whole rock ($\delta^{56}Fe_{WR}$ = -0.15 ±0.07‰) from this dataset is a sample containing the least magnetite and highest pyroxene modal abundance. Likewise, the isotopically heaviest whole rock value ($\delta^{56}Fe_{WR}$ = 0.21 ±0.09‰) reflects high magnetite content. This is the predicted observation considering that phases with more Fe^{3+} (i.e., magnetite) are

expected to be isotopically heavier with respect to Fe, and therefore, whole rock samples with a higher modal abundance of those phases will be comparatively isotopically heavier (e.g., Shahar et al., 2008; Bilenker et al., 2013).

Observed $\delta^{56}Fe_{mgt}$ are consistently isotopically heavier than their whole rock counterparts (Figure 4.1), an expected pattern based on experimental fractionation factors (Shahar et al., 2008; Bilenker et al., 2013) and measurements of natural samples (e.g., Heimann et al., 2008). The data for UUMZ magnetite ($\delta^{56}Fe_{mgt}$ range from 0.28 ±0.05‰ to 0.86 ±0.07‰; average = 0.48 ±0.16‰) show a slight decrease in $\delta^{56}Fe$ with crystallization, though this may be visually biased by a single high $\delta^{56}Fe$ value for the first sample above magnetite saturation, as well as the slightly higher $\delta^{56}Fe$ values for interstitial magnetite separates from samples stratigraphically below cumulus magnetite saturation (Figure 4.1).

Modeling Fe Isotope Evolution During Crystal Fractionation

The fractionation of Fe isotopes between two phases (i.e., mineral, melt) can be modeled by the mass balance equations:

$$\delta^{56}Fe_{liquidY} = X_{liquid(Y-1)} * \delta^{56}Fe_{liquid(Y-1)} - X_{WR(Y-1)} * \delta^{56}Fe_{WR(Y-1)} \qquad (4.2)$$

$$\delta^{56}Fe_{WR} = X_{phase1} * \delta^{56}Fe_{phase1} + X_{phase2} * \delta^{56}Fe_{phase2} + \ldots + X_{phaseX} * \delta^{56}Fe_{phaseX} \qquad (4.3)$$

where Y is the current step within the evolution of the magma and Y-1 represents the previous step. In equation 4.2, X is the proportion of liquid or whole rock comprising the whole system and in equation 4.3, X represents the normalized mass proportion of Fe present within an individual phase within the whole rock. Equations 4.2 and 4.3 require knowledge of (1) the crystallizing phase assemblage and mass proportion of phases at each step; (2) the $\delta^{56}Fe$ of each phase at each step; and (3) an estimate of the initial $\delta^{56}Fe$ of the parent melt, explained further below.

(1) To model the modal abundance of each mineral fractionating at each step, we calculated trends in observed modal data throughout the UUMZ (VanTongeren et al., 2010). In the UUMZ, the modal proportion of pyroxene decreases linearly with increasing stratigraphic height (from ~50 to 11 modal%), whereas the modal abundance of magnetite increases (from ~6 to 16 modal%) (Figure A.1). After olivine saturation, its observed modal abundance in the UUMZ is variable, but maintains a roughly constant proportion throughout the stratigraphy (~15 modal%). The $\delta^{56}Fe$ evolution of the system is dependent only on the crystallization of phases that contain significant amounts of Fe, and therefore the phase proportions of pyroxene, olivine, and magnetite (X_{phase}) were normalized to 1 prior to calculating $\delta^{56}Fe_{WR}$ using equation 4.3.

(2) To model the $\delta^{56}Fe$ of each fractionating phase, we used published fractionation factors for the Fe-bearing mineral phases [$\Delta_{magnetite\text{-}melt}$, Sossi et al., (2012); $\Delta_{magnetite\text{-}fayalite}$, Shahar et al., (2008); $\Delta_{pyroxene\text{-}melt}$, Sossi et al., (2012)]. We calculated crystallization temperatures assuming a linear decrease from 1200°C at the Pyroxenite Marker to 950°C at the top of the stratigraphy, using the newly developed T_{REE} thermometer of Sun et al. (2013) and Liang et al. (2013). Magnetite and olivine were not included in the model until the stratigraphic height at which they appear as a cumulus phase (Figures 4.1, 4.2), even though small amounts of intercumulus magnetite and olivine occur in the rocks of the UUMZ below these levels.

(3) The starting liquid composition in this model was set as $\delta^{56}Fe_{liquid} = 0‰$ for simplicity, but the overall trends are robust regardless of the parent magma initial $\delta^{56}Fe$.

Model results are presented in Figure 4.2 as a function of percent liquid remaining in order to simplify the mass fractionation equations. The fraction of liquid remaining is calculated for each stratigraphic height assuming 15% magma loss from the UUMZ to form some portion of the Rooiberg Group lavas and/or Rashoop Granophyres (e.g., VanTongeren et al. 2010;

Mathez et al., 2013) (Table A.1). Percent liquid remaining in our model varies from 100% at the Pyroxenite Marker (2200 m) to 15% at the roof of the magma chamber (4625 m). More details on the model are found in the Appendix.

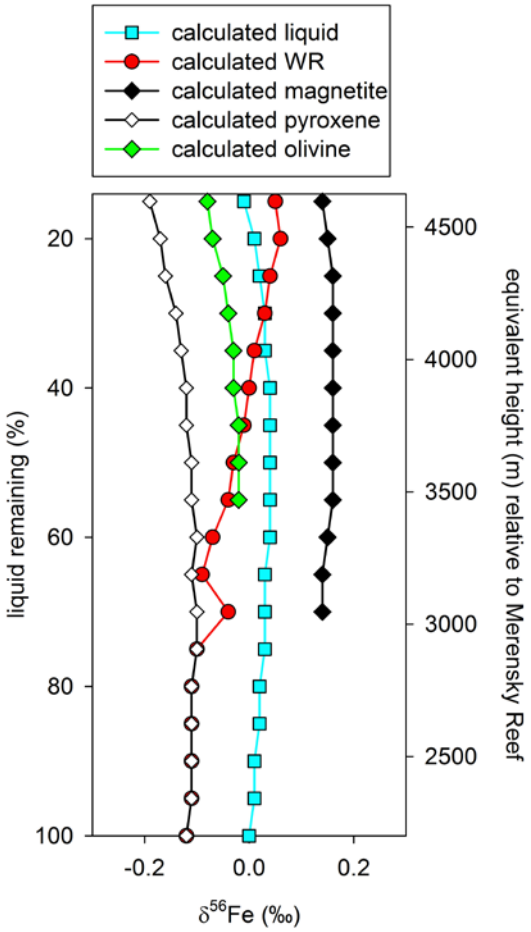

Figure 4.2: Modeled evolution of the Fe isotope composition of the liquid, whole rock, and Fe-bearing minerals during fractional crystallization. The model incorporates published fractionation factors, the normalized calculated modal abundances, and calculated crystallization temperature over the stratigraphy of the UUMZ. See Appendix for details on model parameters.

Model Results

Our model of Fe isotope evolution during fractional crystallization of the UUMZ reveals two important trends: (1) despite the positive mineral-melt fractionation factor for magnetite ($\Delta^{57}Fe_{mgt\text{-}melt} =\sim 0.2 * 10^6/T^2$), the low modal abundance of magnetite relative to pyroxene and olivine in the Bushveld samples buffers the effect of magnetite crystallization on the evolution of

$\delta^{56}Fe$ in the melt and consequently, no significant change in the $\delta^{56}Fe$ of the liquid or of individual phases is predicted in our model (Figure 4.2). For the modal abundances appropriate in the liquid line of descent (LLD) of the UUMZ, our model predicts $\delta^{56}Fe_{liquid}$ to increase by a maximum of 0.04‰. (2) In contrast, the model predicts significant systematic increases in the $\delta^{56}Fe_{WR}$ due to the increasing proportion of magnetite relative to pyroxene and olivine in the cumulus assemblage near the top of the stratigraphy (Figure 4.2). Thus, our model predicts a trend of decreasing $\Delta^{56}Fe_{WR\text{-}mgt}$ with stratigraphic height.

4.3. DISCUSSION

Comparison of Modeled and Measured Data from the UUMZ

The model described above for the crystallization of the UUMZ predicts little change in $\delta^{56}Fe_{mgt}$ with increasing stratigraphic height (Figure 4.2), which is similar to the observed data from the UUMZ (Figure 4.1). The model also predicts an overall increase in $\delta^{56}Fe_{WR}$ with increasing stratigraphic height, which is not observed in our measured data from the UUMZ (Figure 4.1). However, these samples are layered igneous rocks and therefore the modal abundance of each phase in a given sample can be 5 – 50% different than the average modal abundance predicted for that stratigraphic interval. In order to directly compare the model results to the measured values, we use the predicted $\delta^{56}Fe$ of the liquid and phase compositions from the modeled LLD in conjunction with *observed* modal abundances for each of the UUMZ rocks measured at each point in the stratigraphy (equation 4.3; Figure 4.3).

There is agreement in the overall trend between the modeled and measured $\Delta^{56}Fe_{WR\text{-}mgt}$ values from the UUMZ (Figure 4.3); however, in some samples the measured values are noticeably higher in $\Delta^{56}Fe_{WR\text{-}mgt}$ than predicted by the model. The difference between the modeled and measured $\Delta^{56}Fe_{WR\text{-}mgt}$ values is most likely explained by post-crystallization

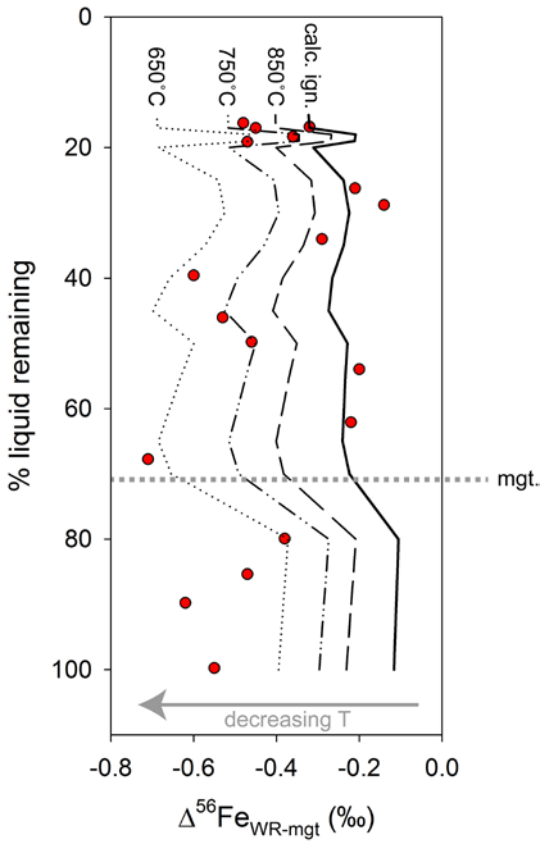

Figure 4.3: The modeled and measured $\Delta^{56}Fe_{WR\text{-}mgt}$ show matching trends over the evolution of the UUMZ parent liquid. Modeled values were calculated by subtracting the modeled $\delta^{56}Fe_{mgt}$ compositions (Figure 4.2; equation 4.3) from a $\delta^{56}Fe_{WR}$ calculated using the modal abundance of minerals observed in the rock with the modeled $\delta^{56}Fe$ of each mineral. Red circles are the measured data. Lines represent model outputs incorporating different temperatures, from the calculated crystallization temperature (c.f. Sun et al., 2013; Liang et al., 2013; "calc. ign.") down to 650°C. Mgt—magnetite saturation.

re-equilibration of $\delta^{56}Fe_{mgt}$ to lower temperature, whether due to the trapped liquid effect (e.g. Barnes et al., 1986) or sub-solidus re-equilibration (e.g., Fe^{2+} and Fe^{3+} interdiffusion in magnetite and other Fe-bearing phases, see Appendix A). Post-crystallization re-equilibration is not unexpected in slowly cooled cumulus rocks such as layered intrusions (Barnes et al., 1986) and has been inferred from exsolution lamellae in magnetites from the Bushveld Complex Upper Zone (Reynolds et al., 1986; Butcher and Merkle, 1987). Samples with the lowest modal abundance of magnetite and the highest abundance of pyroxene, show the greatest offset from

the modeled igneous values, as would be predicted during sub-solidus re-equilibration (Figure A.2). Our model is able to reproduce the measured values from the UUMZ when equilibration temperatures between 650°C and igneous values are used to calculate fractionation factors between the mineral compositions and the originally modeled LLD (Figure 4.3; see Appendix for details).

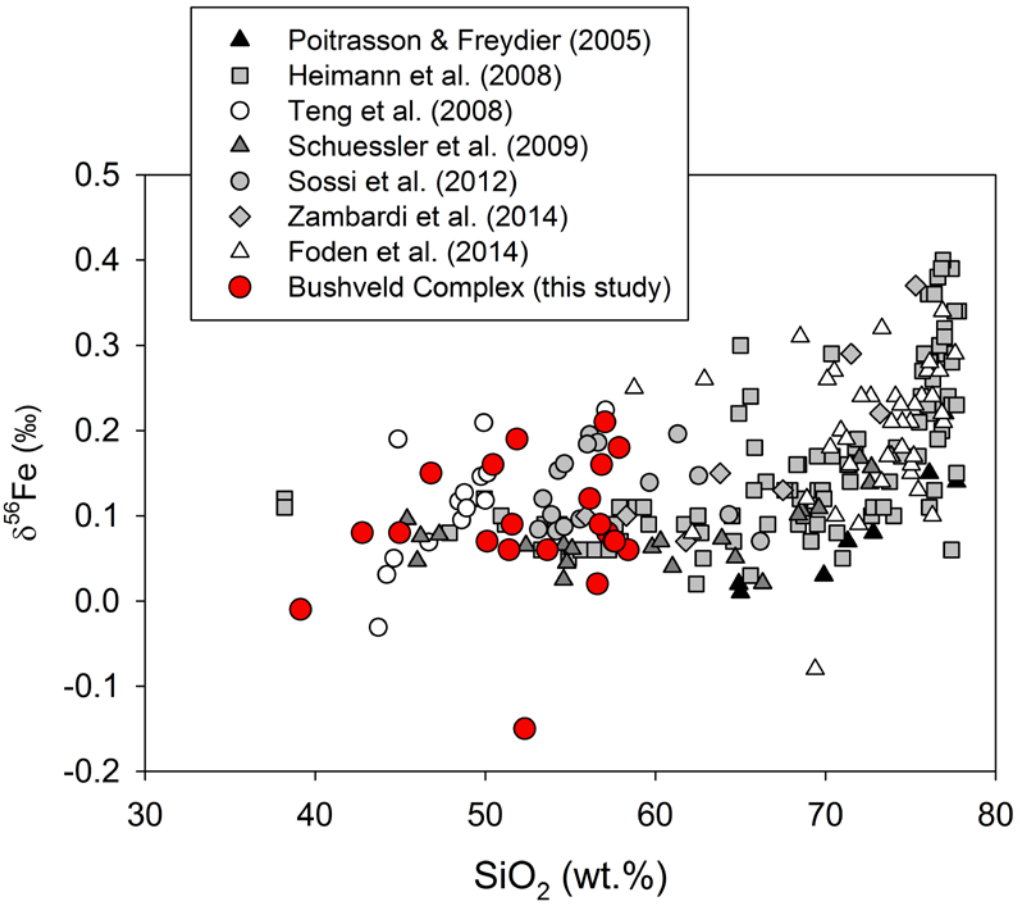

Figure 4.4: Whole rock Bushveld Complex $\delta^{56}Fe$ values (red circles) from this study plotted versus whole rock SiO_2 content along with seven other studies on igneous whole rocks. The Bushveld data are consistent with data from other igneous systems that evolved closed to O_2 gain/loss (circles), such as Kilauea Iki, Hawaii, USA (white circles; Teng et al., 2008) and the Red Hill Intrusion, Tasmania (gray circles; Sossi et al., 2012).

Comparison to other Intrusive Igneous Rocks

Sossi et al. (2012) measured the $\delta^{57}Fe$ composition of 16 whole rock and 6 magnetite-pyroxene pairs from the Red Hill sill, a ~420 m thick intrusion emplaced by a single injection of

magma (Figure 4.4). They reported increasing $\delta^{57}Fe_{WR}$ with decreasing whole rock MgO wt%, and attributed this to the effects of fractional crystallization of Fe-bearing phases on the $Fe^{3+}/\Sigma Fe$ of the melt. They compared their results to data from Hekla volcano (e.g., Schuessler et al. 2009), and suggested that systems open to oxygen, (i.e., buffered at a specific fO_2) would not record significant changes in $\delta^{57}Fe_{WR}$ until late in their crystallization history, whereas those closed to oxygen should display increasing $\delta^{57}Fe_{WR}$ throughout the stratigraphy. In the UUMZ, magnetite-ilmenite pairs record equilibrium fO_2 values near FMQ-1 throughout the stratigraphy (e.g., VanTongeren and Mathez, 2012). The lack of systematic changes in $\delta^{56}Fe_{WR}$ in the UUMZ is consistent with the hypothesis of Sossi et al. (2012).

In a comprehensive study of Fe isotope fractionation in the Baima Layered Intrusion, China, Chen et al. (2014) report $\delta^{56}Fe$ data for whole rocks, olivine, pyroxene, magnetite, and ilmenite separates throughout the stratigraphy. They reported little change in the $\delta^{56}Fe$ composition of the whole rock with increasing stratigraphic height ($\delta^{56}Fe \pm 2SE$ range: -0.02 ± 0.00‰ to 0.16 ± 0.04‰), but did observe slight cyclic trends corresponding to individual pulses of magma. They suggest that the extensive crystallization of magnetite and olivine had a measurable effect on the $\delta^{56}Fe_{WR}$, consistent with our data. Additionally, they found a distinctive trend of increasing $\delta^{56}Fe_{mgt}$ (0.18 ± 0.08‰ at the base to 0.36 ± 0.02‰ at the top). To a first order, this appears to be the opposite of trends observed in our study; however, two important points must be considered: (1) The Baima Intrusion is highly unique in that the Basal and Lower Zones are dominated by Fe-Ti oxides, constituting up to 55 modal% of the rocks. The abundance of Fe-Ti oxides, and the ratio of magnetite/ilmenite, *decrease* with increasing stratigraphic height, which is opposite to what is observed in the UUMZ; (2) the Baima Intrusion

formed from multiple pulses of magma injected throughout its crystallization history, and is not a record of closed system processes.

Relative to granitic rocks, there is a consistent observation of low $\delta^{56}Fe_{WR}$ values of mafic to intermediate igneous rocks (SiO_2 <~67 wt.%) (Poitrasson and Freydier, 2005; Heimann et al., 2008) (Figure 4.4). The $\delta^{56}Fe_{WR}$ of our Bushveld samples plot consistently within the range of $\delta^{56}Fe_{WR}$ data from rocks thought to have formed in other closed igneous systems (e.g., Kilauea Iki, Hawaii, USA, Teng et al., 2008; Red Hill Intrusion, Tasmania, Sossi et al., 2012) (Figure 4.4). Since the UUMZ lacks evidence for significant changes in fO_2 or extensive fluid exsolution, we conclude that the measured $\delta^{56}Fe_{WR}$ values presented here reflect the evolution of Fe isotopes during fractional crystallization.

4.4. CONCLUSIONS

We provide the first $\delta^{56}Fe$ data for whole rock and magnetite separates throughout the fractional crystallization sequence of the UUMZ of the Rustenberg Layered Suite. $\delta^{56}Fe_{WR}$ does not vary systematically with stratigraphic height, though there appears to be a very slight overall decrease in $\delta^{56}Fe_{mgt}$ with increasing stratigraphic height. Existing fractionation factors allow us to model the Fe isotope evolution within the uppermost Bushveld Complex purely as a fractional crystallization process. Our data demonstrate two important points:

(1) While crystallization of a single mineral phase will clearly have an effect on the Fe isotopic evolution of the liquid (e.g., Teng et al., 2008; Shahar et al., 2008), the overall effect of fractional crystallization of a multiply-saturated nominally anhydrous Fe-rich tholeiitic magma will be minimal.

(2) It is fundamentally important to consider the modal mineralogy, including interstitial Fe-bearing mineral phases, when interpreting whole rock Fe isotopic data of cumulate rocks.

4.5. REFERENCES

Barnes, Stephen J. (1986) The effect of trapped liquid crystallization on cumulus mineral compositions in layered intrusions. Contrib. Mineral. Petrol. 93, 524-531.

Bilenker L.D., Simon A., Lundstrom C.C., Gajos N. and Zajacz Z. (2013) Experimental constraints on Fe isotope fractionation in fluid-melt-oxide-sulfide assemblages. *Goldschmidt Conference*.

Butcher, Alan R., and Roland KW Merkle (1987) Postcumulus modification of magnetite grains in the upper zone of the Bushveld Complex, South Africa. Lithos 20, 247-260.

Cawthorn, R.G, Davies, G., Clubley-Armstrong, A., and McCarthy. T.S., 1981, Sills associated with the Bushveld Complex, South Africa: an estimate of the parental magma composition: LITHOS, v. 14, p.1-15.

Cawthorn, R.G., and Walraven, F., 1998, Emplacement and crystallizaiton time for the Bushveld Complex. Journal of Petrology, v. 39, 1669-1687.

Chen, L-M., Song, X-Y., Zhu, X-K., Zhang, X-Q., Yu S-Y., Yi, J-N., 2014, Iron isotope fractionation during crystallization and sub-solidus re-equilibration: constraints from the Baima mafic layered intrusion, SW China. Chemical Geology, v. 380, p. 97-109.

Dauphas, N., Roskosz, M., Alp, E.E., Neuville, D.R., Hu, M.Y, Sio, C.K., Tissot, F.L.H, Zhao, J., Tissandier, L., Médard, E. and Cordier, C., 2014, Magma redox and structural controls on iron isotope variations in Earth's mantle and crust. Earth and Planetary Science Letters, v. 308, 127-140.

Foden, J., Sossi, P.A., and Wawryk, C.M., 2015, Fe isotopes and the contrasting petrogenesis of A-, I- and S-type granite. Lithos, doi:10.1016/j.lithos.2014.10.015.

Harney, D.M.W., and vonGruenewaldt, G., 1995, Ore-forming processes in the upper part of the Bushveld Complex , South Africa. Jour. Afri. Earth Sciences, v. 20, 77-89.

Heimann A., Beard, B.L., and Johnson C.M., 2008, The role of volatile exsolution and sub-solidus fluid/rock interactions in producing high $^{56}Fe/^{54}Fe$ ratios in siliceous igneous rocks. Geochim. Cosmochim. Acta, v. 72, 4379-4396.

Huang, F., Chakraborty, P., Lundstrom, C.C., Holmden, C., Glessner, J.J.G., Kieffer, S.W., and Lesher C.E., 2010, Isotope fractionation in silicate melts by thermal diffusion. Nature, v. 464, 396-400.

Kruger, F.J., Cawthorn, R.G., Walsh, K.L., 1987, Strontium isotopic evidence against magma addition in the Upper Zone of the Bushveld Complex. Earth and Planetary Science Letters, v. 84, p. 51-58.

Liang, Y., Sun, C., Ashwal, L.D., Vantongeren, J.A., 2013, Spatial variations in temperature across the Bushveld layered intrusion revealed by REE-in-plagioclase-pyroxene thermometers with implications for magma chamber processes [abs.]: Transactions, American Geophysical Union, abstract #V54B-07.

Lundstrom, C.C., 2009, Hypothesis for the origin of convergent margin granitoids and Earth's continental crust by thermal migration zone refining. Geochim. Cosmochim. Acta 73, 5709-5729.

Mathez, E.A., 1995, Magmatic metasomatism and formation of the Merensky Reef, Bushveld Complex: Contributions to Mineralogy and Petrology, v. 119, p. 277-286.

Mathez, E. A., J. A. VanTongeren, and J. Schweitzer, 2013, On the relationships between the Bushveld Complex and its felsic roof rocks, part 1: petrogenesis of Rooiberg and related felsites. Contrib. Mineral. Petrol. 166, 435-449.

Millet, M., Baker, J., and Payne, C., 2012, Ultra-precise stable Fe isotope measurements by high resolution multi-collector inductively coupled plasma mass spectrometry with a ^{57}Fe-^{58}Fe double spike. Chem. Geol. 304-305, 18-25.

Molyneux, T. G., 1974, A geological investigation of the Bushveld Complex in Sekhukhuneland and part of the Steelpoort Valley: Transactions of the Geological Society of South Africa, v. 77, 329-338.

Poitrasson, F., and Freydier, R., 2005, Heavy iron isotope composition of granites determined by high resolution MC-ICP-MS. Chem. Geol. 222, 132-147.

Reynolds, Ivan M. (1985) The nature and origin of titaniferous magnetite-rich layers in the upper zone of the Bushveld Complex; a review and synthesis. Econ. Geol. 80, 1089-1108.

Schuessler, J.A., Schoenberg, R., Behrens, H., and von Blanckenburg, F., 2007, The experimental calibration of the iron isotope fractionation factor between pyrrhotite and peralkaline rhyoltic melt. Geochim. Cosmochim. Acta 71, 417-433.

Schuessler, J.A., Schoenberg, R., and Sigmarsson, O., 2009, Iron and lithium isotope systematics of the Hekla volcano, Iceland—Evidence for Fe isotope fractionation during magma differentiation. Chem. Geol. 258, 78-91.

Shahar, A., Young, E.D., and Manning, C.E., 2008, Equilibrium high-temperature Fe isotope fractionation between fayalite and magnetite: An experimental calibration. Earth Planet. Sc. Lett. 268, 330-338.

Sossi, P.A., Foden, J.D. and Halverson, G.P. (2012) Redox-controlled iron isotope fractionation during magmatic differentiation: an example from the Red Hill intrusion, S. Tasmania. Contrib. Mineral. Petrol. 164, 757-779.

Sun, C., Liang, Y., Ashwal, L., VanTongeren, J., 2013, Temperature variations along stratigraphic height across the Bushveld Complex with implications for magma chamber processes in layered intrusions [abs]: GSA Abstracts with Programs 45, 390.

Telus, M., Dauphas, N., Moynier, F., Tissot, F. L.H., Teng, F-Z., Nabelek, P.I., Craddock, P.R. and Groat, L.A., 2012, Iron, zinc, magnesium and uranium isotopic fractionation during continental crust differentiation: The tale from migmatites, granitoids, and pegmatites. Geochim. Cosmochim. Acta 97, 247-265.

Teng, F., Dauphas, N. and Helz, R.T., 2008, Iron isotope fractionation during magmatic differentiation in Kilauea Iki Lava Lake. Science 320, 1620-1622.

VanTongeren et al., 2010, A Felsic End to Bushveld Differentiation: Journal of Petrology, 51, 1891-1942.

VanTongeren, J.A., and Mathez, E.A., 2012, Large-scale liquid immiscibility at the top of the Bushveld Complex. Geology 40, 491-494.

VanTongeren, J.A., and Mathez, E.A., 2013, Incoming Magma Composition and Style of Recharge below the Pyroxenite Marker, Eastern Bushveld Complex, South Africa. Journal of Petrology 54, 1585-1605.

Weyer, S., 2008, What Drives Iron Isotope Fractionation in Magma? Science Perspectives 320, 1600-1601.

Williams, H.M., Peslier, A.H., McCammon, C., Halliday, A.N., Levasseur, S., Teutsch, N., and Burg, J.-P., 2005, Systematic iron isotope variations in mantle rocks and minerals: The effects of partial melting and oxygen fugacity. Earth Planet. Sc. Lett. v. 235, p. 435-452.

Young, E.D., Manning, C.E., Schauble, E.A., Shahar, A., Macris, C.A., Lazar, C. and Jordan, M., 2015, High-temperature equilibrium isotope fractionation of non-traditional stable isotopes: Experiments, theory, and applications. Chem. Geol., v. 395, p. 176-195.

Zambardi, T., Lundstrom, C.C., Li, X., McCurry, M., 2014, Fe and Si isotope variations at Cedar Butte volcano; insight into magmatic differentiation. Earth and Planetary Science Letters, v. 405, p. 169-179.

CHAPTER V

CONCLUSIONS

High-temperature Fe isotope geochemistry is a new and useful tool for studying igneous systems and ore deposits, and we are now able to quantify Fe isotope fractionation within these systems by experimental and field-based methods. This dissertation demonstrates the importance of high-temperature experimental Fe isotope studies as they provide a controlled framework within with we can interpret natural samples, while natural samples provide a realistic context.

Additional experimental calibration and investigation are necessary to further develop our understanding of the mechanisms that fractionate stable Fe isotopes under conditions relevant to igneous and ore-forming processes. ***Chapter II*** emphasized the importance of this, presenting data from high-temperature experiments that produced results opposite to those that we would expect based upon theoretical calculations. Our experimental study was not the first to highlight the discrepancy between theoretical predictions and experimental data (e.g., Shahar et al., 2008), but it was the first to include an aqueous fluid phase in experimental phase assemblages. This is significant due to the number of studies that assume any Cl-bearing aqueous fluid in equilibrium with a high-SiO_2 melt/magma will be isotopically lighter than the melt/magma. More high-temperature experiments investigating the effect of fluid and melt compositions would be particularly useful for providing additional insight into the pattern of increasing $\delta^{56}Fe$ with increasing SiO_2 content in many igneous rocks.

Chapters III and ***IV*** applied Fe isotopes to natural samples, focusing on the world-class Los Colorados iron oxide—apatite (IOA) deposit (Chile) and the world's largest exposed mafic magma chamber and layered intrusion, the Bushveld Igneous Complex (South Africa). These deposits served as case studies for Fe—O and Fe stable isotope systematics, respectively. The Los Colorados IOA contains ~350 Mt Fe in two massive magnetite dikes (up to >90 modal%) that are minimally altered. Iron and O isotope pairs measured in magnetite separates from drill core and pit samples were used to determine a high-temperature origin for the Los Colorados and other Chilean IOA deposits, as well as the namesake IOA deposit, Kiruna in Sweden. Oxygen isotope values and Fe numbers measured in co-existing actinolite grains allowed for us to calculate minimum formation temperatures that corroborate our hypothesis of a high-temperature origin for Los Colorados. This work also contributed to a study (Knipping et al., 2015) that proposes a new model for the formation of IOAs by flotation of magnetite within a magmatic system. The Fe—O isotope pairs were used in conjunction with detailed geochemical analyses of Los Colorados magnetite grains, since we are not yet able to pinpoint specific high-temperature processes by using the isotope data alone. However, we will eventually be able to do so by collecting more Fe and O isotope data from natural samples of known origin. The agreement of the additional geochemical data in both Los Colorados studies demonstrates that the Fe—O isotope method is robust.

The work presented in ***Chapter IV*** on the uppermost portion of the Bushveld Complex is an example of the benefit of using a relatively under-developed geochemical tool on a well-characterized deposit. There are many studies that have been published on the Bushveld since it is well exposed, is a layered mafic intrusion, and much of the world's platinum group elements are mined from one layer within the Complex (the Merensky Reef, stratigraphically below our

study area). The Upper and Upper Main Zones (UUMZ) that comprise the ~2.5 km of the Rustenberg Layered Suite of the Bushveld are thought to have been formed by one magmatic event and evolved under relatively closed conditions. Systematic fractional crystallization during magmatic differentiation is observed stratigraphically upward from the base of the UUMZ (the Pyroxenite Marker). However, at first glance, our stable Fe isotope data do not reveal systematic patterns reflecting fractional crystallization, despite the fact that we know this process plays a significant role in the formation of these rocks. Since the Bushveld is a layered intrusion, with concentrated horizons of individual minerals appearing at irregular intervals throughout the stratigraphy, we needed to take this into account when interpreting the whole rock and magnetite δ^{56}Fe. We were able to show that, by using published fractionation factors, we could mimic the whole rock and magnetite δ^{56}Fe, but not the magnitude of $\Delta^{56}Fe_{WR\text{-}magnetite}$ until closure temperatures were incorporated into the model. Thanks to the availability of an abundance of data for Bushveld rocks, we were able to quantify and determine that the measured Fe isotope systematics of the UUMZ, and likely other layered mafic intrusions, are controlled by fractional crystallization and the thermal history of the system.

This body of work shows that using the methods of pairing Fe—O isotope values in magnetite and analyzing the Fe isotope systematics of whole rock and mineral samples are useful tools with which we can improve our understanding of igneous rocks and ore deposits. It seems that the more samples we analyze, the more we reveal about the complexity of stable Fe isotope fractionation in natural igneous and ore systems. With additional experimental and field-based research, high-temperature stable Fe isotope geochemistry may eventually become useful as an exploration tool used to identify new resources of Fe, copper, gold, and rare earth elements. This would be quite valuable given that knowing how an ore deposit forms is imperative for

successful exploration, which itself is necessary to sustain our current demand of these metals that are used to produce items we use on a daily basis.

References

Knipping J.L., Bilenker L.D., Simon A.C., Reich M., Barra F., Deditius A.P., Lundstrom C., Bindeman I. and Munizaga R. (2015) Giant Kiruna-type deposits form by efficient floation of magmatic magnetite suspensions. *Geology*, published online 19 May 2014, doi:10.1130/G36650.1.

Shahar A., Young E.D. and Manning C.E. (2008) Equilibrium high-temperature Fe isotope fractionation between fayalite and magnetite: An experimental calibration. *Earth Planet. Sc. Lett.* **268**, 330-338.

APPENDIX

MODEL DETAILS AND ADDITIONAL FIGURES FOR CHAPTER IV

Our model of the Fe isotope evolution within the Upper and Upper Main Zones (UUMZ) of the Bushveld Complex incorporates several individual parameters whose chosen values are explained below. In addition, we make certain important assumptions: First, we assume perfect crystallization; i.e., a controlled amount of liquid crystallizes at each step (5% of the initial liquid present, not 5% of the liquid present at the current model step). The model stops at 15% liquid remaining, at which point the residual magma is erupted to the surface to form portions of the Rooiberg Group lavas and/or Rashoop Granophyres, as was proposed by VanTongeren et al. (2010). Further, the $\delta^{56}Fe$ of the starting liquid was fixed at 0‰, for simplicity. This assumption has no bearing on the trends produced by the model as they hold regardless of the pre-determined initial $\delta^{56}Fe_{liquid}$.

Liquid remaining and modal mineralogy

Values incorporated into the model for 1.) percent liquid remaining and 2.) mineral modes were based upon the geochemistry of the natural samples.

1.) The percent liquid remaining is correlated to the stratigraphic height in the UUMZ according to the following relationship:

$$\text{Liquid remaining (\%)} = 15 + 100*(4625 - d)/2850$$

where d represents the stratigraphic depth in meters above the Merensky Reef in the eastern Bushveld. The Pyroxenite Marker is located at 2200 m (100% liquid remaining) and the roof of the UUMZ is at 4625 m (15% liquid remaining).

2.) Modal abundances are based upon values reported by VanTongeren et al. (2010) (Figure 4.1; Figure A.1). For our model, the abundance of an individual mineral ($X_{mineral}$) was considered to be 0 until the stratigraphic height at which it appears as a cumulus phase (pyroxene: 2200 m; magnetite: 3070 m; olivine: ~3400 m). Modal abundances of the Fe-bearing minerals were normalized to 1 since only Fe-bearing phases can contribute to δ^{56}Fe values (Table A.1). Pyroxene, magnetite, and olivine are the only cumulus Fe-bearing phases present within the UUMZ (Figure A2).

Temperature

The modeled $\Delta^{56}Fe_{WR\text{-}mgt}$ are produced for a range in temperature (Figure 4.3). The igneous crystallization temperature of the UUMZ magma decreases during fractional crystallization from approximately 1250°C at the Pyroxenite Marker to approximately 950°C at the roof. These temperatures are calculated from rare earth element (REE) contents of plagioclase and pyroxene using the newly developed method of Sun et al. (2013) and Liang et al. (2013), who observe a linear evolution in temperature from ~1250°C at 2200 m to ~1050°C at 3500 m in the UUMZ. After ~3500 m in the stratigraphy, the REE thermometer is no longer calibrated for the compositional range. Thus, temperatures for the stratigraphy from 3500 m to 4625 m are calculated assuming the same slope in temperature vs. stratigraphic height. Over the course of the entire UUMZ stratigraphy, the crystallization temperature in our model decreases by ~15°C per 5% decrease in percent liquid remaining (i.e., at each model step).

Given that fractionation factors are T-dependent, and that modeled $\Delta^{56}Fe_{WR\text{-}mgt}$ values match the trends observed in the samples but do not necessarily predict each point, we compared the results with various lower T models (Figure 4.3; Figure A.2) . While the “calculated igneous” T model incorporates a realistic T gradient over the ~2.5 km of the UUMZ, the lower T models

were produced by using a single T over the entire stratigraphy. For example, the 850°C model used 850°C to calculate the fractionation factors for pyroxene, magnetite, and olivine at every percentage of liquid remaining.

Fe isotope fractionation factors

All fractionation factors ($\Delta^{57}Fe_{phaseA\text{-}phaseB}$) used in the model are from previously published field- or lab-based studies and are calculated by incorporating T and converting to $\Delta^{56}Fe_{phaseA\text{-}phaseB}$ by the relationship: $\Delta^{57}Fe_{phaseA\text{-}phaseB} / 1.5 = \Delta^{56}Fe_{phaseA\text{-}phaseB}$. The temperature-dependent equations for each cumulus Fe-bearing mineral are:

$$\Delta^{57}Fe_{pyroxene\text{-}melt} = -0.25 * (10^6/T^2) \text{ (Sossi et al., 2012)}$$

$$\Delta^{57}Fe_{magnetite\text{-}melt} = 0.2 * (10^6/T^2) \text{ (Sossi et al., 2008)}$$

$$\Delta^{57}Fe_{magnetite\text{-}fayalite} = 0.3 * (10^6/T^2) \text{ (Shahar et al., 2008)}$$

The $\Delta^{57}Fe_{pyroxene\text{-}melt}$ and $\Delta^{57}Fe_{magnetite\text{-}melt}$ equations are derived from measurements of samples from the Red Hill Intrusion, Tasmania, a sill containing dolerite and granophyre that was injected in a single event and evolved as a closed system (Sossi et al., 2012). $\Delta^{57}Fe_{magnetite\text{-}fayalite}$ is based on an experimental calibration performed between magnetite and fayalite between 600°C and 800°C by Shahar et al. (2008). These fractionation factors are the only ones available in the literature, to our knowledge, that are applicable for the T range and composition of the UUMZ.

Difference between modeled and measured $\Delta^{56}Fe_{WR\text{-}mgt}$ values

Each presented model ("calculated igneous", 850°C, 750°C, 650°C) is consistent with different measured data (Figure 4.3). Although the overall pattern of the Fe isotopic shifts over the stratigraphy is mirrored by all models, no single model predicts each measured datum. We can use the difference between the modeled and measured $\Delta^{56}Fe_{WR\text{-}mgt}$ values (measured $\Delta^{56}Fe_{WR\text{-}mgt}$ minus modeled $\Delta^{56}Fe_{WR\text{-}mgt}$) to evaluate the cause of this discrepancy. The difference

between the $\Delta^{56}Fe_{WR\text{-}mgt}$ values modeled using the calculated igneous T and the measured $\Delta^{56}Fe_{WR\text{-}mgt}$ values is best correlated with the whole rock FeO content (Figure A.2A), as well as modal abundance of pyroxene (Figure A.2). The modeled $\Delta^{56}Fe_{WR\text{-}mgt}$ values are closest to the measured $\Delta^{56}Fe_{WR\text{-}mgt}$ values when there is less co-existing pyroxene and more available Fe within the whole rock. This likely indicates sub-solidus re-equilibration of magnetite with respect to Fe isotopes. As a magma cools, post-crystallization interdiffusion of Fe^{3+} and Fe^{2+} will allow for the $\delta^{56}Fe$ composition of magnetite to be influenced by the abundance of co-existing Fe-bearing phases.

Although there appears to be a correlation between olivine abundance and the difference between the modeled $\Delta^{56}Fe_{WR\text{-}mgt}$ values, magnetite is not likely re-equilibrating at sub-solidus conditions with olivine since the models more closely match the measured $\Delta^{56}Fe_{WR\text{-}mgt}$ in its presence. Further, pyroxene abundance concurrently decreases. The modeled $\Delta^{56}Fe_{WR\text{-}mgt}$ also become closer to measured values higher in the UUMZ stratigraphy. We know from Figure A.1 that pyroxene modal abundance also decreases higher in the UUMZ while whole rock FeO increases, indicating that pyroxene mode is more strongly tied to offsetting the models from measured values than the presence of olivine. Overall, magnetite $\delta^{56}Fe$ values from rocks containing a lower abundance of other Fe-bearing phases more closely reflect the $\delta^{56}Fe$ composition of the magnetite during its crystallization.

References

Liang, Y., Sun, C., Ashwal, L.D., VanTongeren, J.A., 2013, Spatial variations in temperature across the Bushveld layered intrusion revealed by REE-in-plagioclase-pyroxene thermometers with implications for magma chamber processes [abs.]: Transactions, American Geophysical Union, abstract #V54B-07.

Shahar, A., Young, E.D., and Manning, C.E., 2008, Equilibrium high-temperature Fe isotope fractionation between fayalite and magnetite: An experimental calibration. Earth Planet. Sc. Lett. 268, 330-338.

Sossi, P.A., Foden, J.D. and Halverson, G.P., 2012, Redox-controlled iron isotope fractionation during magmatic differentiation: an example from the Red Hill intrusion, S. Tasmania. Contrib. Mineral. Petrol. 164, 757-779.

VanTongeren et al., 2010, A Felsic End to Bushveld Differentiation: Journal of Petrology, 51, 1891-1942.

Table A.1: All $\delta^{56}Fe$ values from whole rock-magnetite pairs with associated 2σ, sample lithology, and modal abundaces of Fe-bearing minerals. NA indicates that not enough pure magnetite could be separated from the sample for Fe isotope analysis. Blank indicates that observed modal abundance is unvailable for that sample.

Stratigraphic position (m) relative to the MR	Equivalent % liquid remaining	$\delta^{56}Fe_{WR}$ (‰)	2σ	$\delta^{56}Fe_{magnetite}$ (‰)	2σ	Lithology	Normalized observed modal abundance of Fe-bearing minerals		
							Pyroxene	Magnetite	Olivine
2210	99.74	0.06	0.09	0.61	0.06	gabbro	1	0	0
2325	95.70	-0.15	0.07	*NA*	*NA*	gabbro			
2495	89.74	0.06	0.04	0.69	0.08	gabbro	1	0	0
2620	85.35	0.19	0.13	0.65	0.08	gabbro	1	0	0
2775	79.91	0.09	0.07	0.47	0.11	gabbro	1	0	0
3122	67.74	0.15	0.08	0.86	0.07	gabbro	0.75	0.25	0
3260	62.89	0.12	0.07	0.34	0.03	gabbro	0.79	0.21	0
3425	57.11	0.16	0.07	*NA*	*NA*	anorthosite			
3515	53.95	0.08	0.08	0.28	0.05	troctolite	0.07	0.13	0.80
3634	49.77	0.07	0.08	0.53	0.06	gabbro	0.47	0.26	0.27
3741	46.02	0.08	0.05	0.61	0.04	gabbro	0.54	0.14	0.32
3925	39.56	-0.01	0.03	0.59	0.04	gabbro	0.57	0.20	0.23
4083	34.02	0.08	0.05	0.37	0.07	troctolite	0.22	0.24	0.53
4232	28.79	0.21	0.09	0.35	0.09	diorite	0.12	0.29	0.59
4305	26.23	0.09	0.02	0.3	0.05	diorite	0.16	0.28	0.56
4355	24.47	0.12	0.06	0.38	0.02	diorite			
4460	20.79	0.07	0.03	0.32	0.03	diorite			
4508	19.11	0.16	0.05	0.63	0.17	diorite	0.37	0.12	0.51
4530	18.33	0.02	0.06	0.38	0.02	diorite	0.45	0.45	0.10
4555	17.46	0.18	0.04	0.63	0.05	diorite			
4573	16.82	0.06	0.06	0.38	0.05	diorite	0.39	0.12	0.50
4590	16.23	0.07	0.03	0.56	0.03	diorite	0.44	0.13	0.43

Figure A.1: Observed modal abundances of pyroxene (blue circles), olivine (green squares), and magnetite (gray diamonds) throughout the stratigraphy of the UUMZ, after VanTongeren et al. (2010). Mgt—magnetite saturation; ol—olivine saturation.

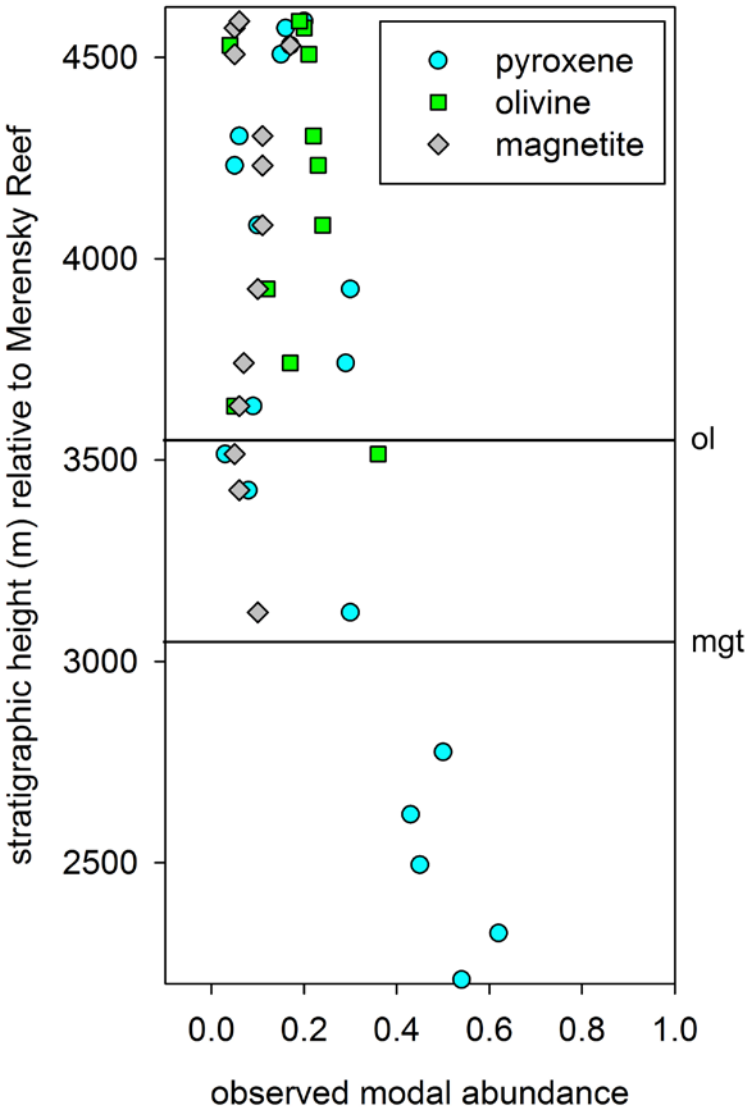

Figure A.2: The difference between measured and modeled $\Delta^{56}Fe_{WR\text{-}mgt}$ values versus whole rock FeO content (A), and abundances of pyroxene (B), magnetite (C), and olivine (D). The difference between measured and modeled $\Delta^{56}Fe_{WR\text{-}mgt}$ decreases most strongly with increasing whole rock FeO and pyroxene mode, while it decreases with increasing olivine abundance. Data in brackets represent samples below magnetite saturation.